*Astronomy Letters, Vol. 30, No. 9, 2004, pp. 583–592. Translated from Pis'ma v Astronomicheskiĭ Zhurnal, Vol. 30, No. 9, 2004, pp. 643–652.*


# NGC 7468: A Galaxy with an Inner Polar Disk

**L. V. Shalyapina[1*], A. V. Moiseev[2], V. A. Yakovleva[1], V. A. Hagen-Thorn[1], and O. Yu. Barsunova[1]**

[1]*Sobolev Astronomical Institute, St. Petersburg State University, Universitetskii pr. 28, Petrodvorets, 198504 Russia*

[2]*Special Astrophysical Observatory, Russian Academy of Sciences, Nizhnii Arkhyz, Karachai-Cherkessian Republic, 357147 Russia*

Received January 22, 2004

**Abstract**—We present our spectroscopic observations of the galaxy NGC 7468 performed at the 6-m Special Astrophysical Observatory telescope using the UAGS long-slit spectrograph, the MPFS multipupil fiber spectrograph, and the IFP scanning Fabry–Perot interferometer. We found no significant deviations from the circular rotation of the galactic disk in the velocity field in the regions of brightness excess along the major axis of the galaxy (the putative polar ring). Thus, these features are either tidal structures or weakly developed spiral arms. However, we detected a gaseous disk at the center of the galaxy whose rotation plane is almost perpendicular to the plane of the galactic disk. The central collision of NGC 7468 with a gas-rich dwarf galaxy and their subsequent merging seem to be responsible for the formation of this disk. © *2004 MAIK "Nauka/Interperiodica"*.

Key words: *galaxies, groups and clusters of galaxies, intergalactic gas, polar-ring galaxies, kinematics.*

## INTRODUCTION

Whitmore *et al.* (1990) included NGC 7468 (Mrk 314) in their catalog of polar-ring galaxies (PRGs), candidate PRGs, and similar objects as a probable candidate (C-69). The direct images (Fig. 1) of this galaxy show an extended low-surface-brightness base and a bright nuclear region resolvable into several individual condensations. Protrusions are observed along the major axis on the galaxy's southern and northern sides, which may suggest the existence of a ring; this was the reason why NGC 7468 was included in the above catalog. The southern protrusion transforms into a faint structure that ends with a brightening whose distance from the galaxy's center in the plane of the sky is $\sim 45''$, or $\sim 7$ kpc. (For the line-of-sight velocity we found, $V_{\rm gal} = 2220$ km s$^{-1}$; with $H_0 = 65$ km s$^{-1}$ Mpc$^{-1}$, the distance to the galaxy is 34 Mpc, which yields a scale of 0.16 kpc in $1''$.)

NGC 7468 was initially classified as a peculiar elliptical galaxy (RC3, LEDA). However, according to a detailed photometric study by Evstigneeva (2000), it should be considered to be a late-type spiral or an irregular galaxy. Indeed, the galaxy is rich in gas, as follows from neutral and molecular hydrogen data (Taylor *et al.* 1993, 1994; Richter *et al.* 1994; Wiklind *et al.* 1995). The ratios $M_{\rm HI}/L_B = 0.621$ and $M_{\rm H_2}/L_B = 0.06$ ($M_{\rm H_2}/M_{\rm HI} = 0.11$) derived for NGC 7468 are characteristic of galaxies of late morphological types (Young *et al.* 1989). The galaxy is an infrared source ($L_{\rm IR}/L_B \sim 0.6$), suggesting the presence of dust whose mass is estimated to be $0.4 \times 10^6 M_\odot$ (Huchtmeier *et al.* 1995).

In the central part of the galaxy, Petrosyan *et al.* (1979) were able to distinguish three condensations whose emission spectra were studied by Petrosyan (1981) and subsequently by Nordgren *et al.* (1995). Since the spectra for the galaxy's central region are similar to those for H II regions, beginning with the works by Thuan *et al.* (1981), this object has been attributed to H II galaxies or blue compact dwarf galaxies (BCDGs) with active star formation in their central regions. The estimates of the star formation rate (Evstigneeva 2000; Cairos *et al.* 2001b) correspond to the star formation rate in BCDGs.

The velocity field inferred from neutral hydrogen (Taylor *et al.* 1993, 1994) exhibits no features in any of the two protrusions and in the brightening region. These authors pointed out that the central isovels are distorted (oval distortion), which may be indicative of the presence of a bar. However, the spatial resolution of these observations is not high.

The photometry performed by Evstigneeva (2000) and Cairos *et al.* (2001b) show that the color of the

*E-mail: lshal@astro.spbu.ru

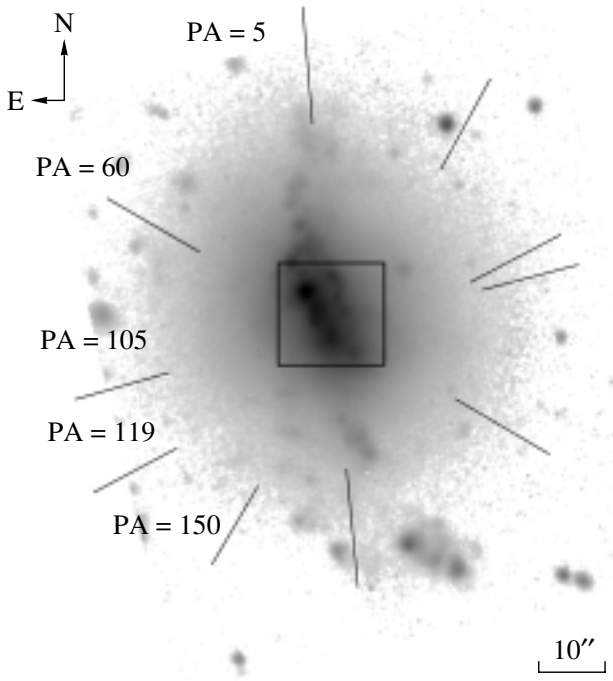


**Fig. 1.** Image of the galaxy NGC 7468 obtained with the 6 m telescope through a filter centered at λ6622 Å; the UAGS slit locations and the MPFS field during observations are shown.

northern and southern protrusions and the brightening is bluer than that in the remaining regions of the galaxy (except for the nuclear region), which was considered by Evstigneeva (2000) as evidence for the presence of an outer polar ring around NGC 7468.

The initial assumption that the brightening to the south of the galaxy is a superassociation (Petrosyan 1981) was replaced by Evstigneeva (2000) with the suggestion that this is a companion galaxy, probably because galaxy interaction is believed to be the most probable cause of the polar-ring formation and because she failed to find another suitable candidate that would confirm the interaction. Meanwhile, Taylor *et al.* (1993) pointed out that there is a faint galaxy 4.′6 (45.5 kpc) north of NGC 7468 that the authors believe to be a possible companion of NGC 7468.

The currently available information is clearly insufficient to determine whether NGC 7468 belongs among PRGs. The velocity field of the galaxy must be studied with a high spatial resolution. This paper presents the results of such a study based on optical spectroscopy.

## OBSERVATIONS AND DATA REDUCTION

We performed our spectroscopic observations of the galaxy NGC 7468 at the prime focus of the 6-m Special Astrophysical Observatory (SAO) telescope with the long-slit spectrograph (UAGS), the multipupil fiber spectrograph (MPFS) (Afanasiev *et al.* 2001), and the scanning Fabry–Perot interferometer (IFP) (see Moiseev (2002) and the SAO site[1]). The table gives a log of observations.

The reduction technique that we used was described previously (Shalyapina *et al.* 2004).

The long-slit spectra were taken near the Hα line (see the table). The Hα and [S II] λλ6716, 6730 Å emission lines proved to be brightest in the spectra; in addition, the [N II] λλ6548, 6583 Å, He I λ6678 Å lines were observed. The line-of-sight velocity curves were constructed from all of the lines. The accuracy of these measurements was ±10 km s$^{-1}$.

The central region of the galaxy was observed with the MPFS in the green spectral range. This range includes metal absorption lines (Mg I λ5175 Å, Fe I λ5229 Å, Fe I+Ca I λ5270 Å, etc.) and the Hβ and [O III] λλ4959, 5007 Å emission lines. Spectra from 240 spatial elements that form a 16 × 15 array in the plane of the sky were taken simultaneously.

Based on emission lines, we constructed two-dimensional maps of the intensity and line-of-sight velocity distributions (velocity fields). The line-of-sight velocities were determined with an accuracy of 10–15 km s$^{-1}$. We used the spectra of the twilight

[1] http://www.sao.ru/hq/lsfvo/devicese.html

Log of observations of NGC 7468

| Instrument, date | Exposure time, s | Field, arcmin | Scale, arcsec | Spectral resolution, Å | Seeing, arcsec | Spectral region, Å | PA field |
|---|---|---|---|---|---|---|---|
| UAGS | 1800 | 2 × 140 | 0.4 | 3.6 | 1.3 | 6200–7000 | 5° |
| | 1200 | 2 × 140 | 0.4 | 3.6 | 1.5 | 6200–7000 | 60° |
| Oct. 2–4, 1999 | 1200 | 2 × 140 | 0.4 | 3.6 | 1.5 | 6200–7000 | 105° |
| | 1800 | 2 × 140 | 0.4 | 3.6 | 1.3 | 6200–7000 | 150° |
| | 300 | 2 × 140 | 0.4 | 3.6 | 1.3 | 6200–7000 | 119° |
| MPFS | 1800 | 16 × 15 | 1 | 4.5 | 2.0 | 4600–6000 | Center |
| Dec. 8, 2001 | | | | | | | |
| IFP | 32 × 240 | 5 × 5 | 0.56 | 2.5 | 1.3 | Hα | |
| Aug. 31, 2002 | | | | | | | |

sky and the galactic nucleus as templates for cross-correlation when constructing the velocity field for the stellar component. The errors in the line-of-sight velocities determined from the absorption lines were found to be ∼15–20 km s$^{-1}$.

Our IFP observations were performed near the Hα line. Preliminary monochromatization was performed using a filter with a central wavelength of 6578 Å and FWHM = 19 Å. The readout was made in 2 × 2-pixel binning mode, with 512 × 512-pixel images being obtained in each spectral channel. These data were used to construct the velocity field and the Hα and continuum brightness maps. The measurement errors of the line-of-sight velocities did not exceed 10 km s$^{-1}$.

## RESULTS OF THE UAGS OBSERVATIONS AND THEIR ANALYSIS

The line-of-sight velocity curves constructed from different emission lines are similar. Figure 2 shows the data obtained from the Hα line at five locations of the UAGS slit. The point of maximum brightness that coincides with the southernmost of the three condensations was taken as zero. As we see from the figures, all of the line-of-sight velocity curves are peculiar. Let us consider these peculiarities in more detail.

The line-of-sight velocity curve obtained at a slit location close to the galaxy's major axis (PA = 5°) is shown in Fig. 2a. In general, its shape agrees with that expected for the rotation of the galaxy's gaseous disk around its minor axis. In the region $-18'' \le R \le 20''$, the line-of-sight velocities change from 2140 to 2030 km s$^{-1}$, flattening out at $R \ge 20''$. However, the change in the velocity is not monotonic. The waves that probably are associated with individual H II regions are seen in the curve at $R \approx -3''$–$5''$ and $R \approx 12''$, and a step where the velocity is almost constant is noticeable at $0 \le R \le 7''$. Obviously, the gas responsible for the emission here is not involved in the rotation of the galaxy's main disk.

The presence of a kinematically decoupled gaseous subsystem at the center is confirmed by the line-of-sight velocity curves for position angles close to the minor axis (PA = 105°, PA = 119°). In both cases, a rectilinear segment with gradient $dV/dR \approx$ 200 km s$^{-1}$ kpc$^{-1}$ is clearly seen in the region $0 \le R \le 3''$, suggesting the rigid-body rotation of the gas around the galaxy's major axis. To the east of the center, the line-of-sight velocities are almost constant and, on average, equal to 2115 km s$^{-1}$. The emission here is attributable to the gas of the galaxy's disk that rotates around its minor axis. At $R \ge 3''$, the behavior of the line-of-sight velocities is different on these two cuts. At the position angle PA = 105°, the slit apparently goes outside the region where the emission of the gas belonging to the central subsystem dominates, and the line-of-sight velocity begins to increase, approaching ≈ 2100 km s$^{-1}$, the value that the subsystem of the galaxy's gaseous disk must have here. At PA = 119°, the further decrease in the line-of-sight velocity with a smaller gradient (30 km s$^{-1}$kpc$^{-1}$) probably stems from the fact that

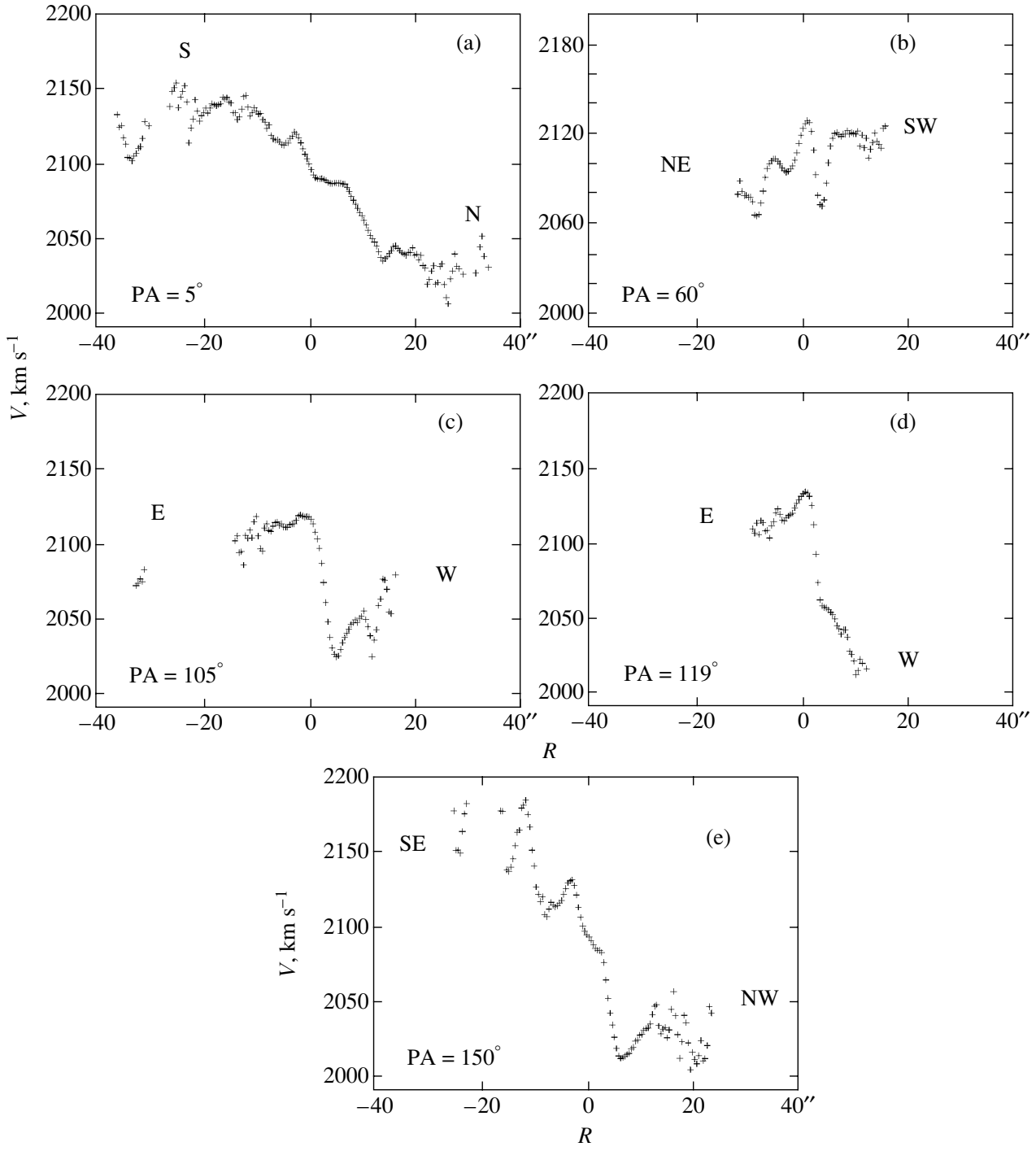


**Fig. 2.** NGC 7468: the UAGS line-of-sight velocity curves.

the cut does not pass through the dynamic center of the decoupled subsystem.

The line-of-sight velocity curves at PA = 60° and PA = 150° are consistent with the assumption that a gaseous subsystem rotating around the major axis is present in the central part of the galaxy. At $R \leq 3''$, the curve also has a rectilinear segment with a gradient $dV/dR \approx 78$ km s$^{-1}$kpc$^{-1}$ northeast of the center at PA = 60° and with a gradient $dV/dR \approx 80$ km s$^{-1}$kpc$^{-1}$ at PA = 150°. The outer segments of the line-of-sight velocity curves are determined by the galaxy's gaseous disk.

Thus, the behavior of all of the line-of-sight velocity curves indicates that there is a kinematically

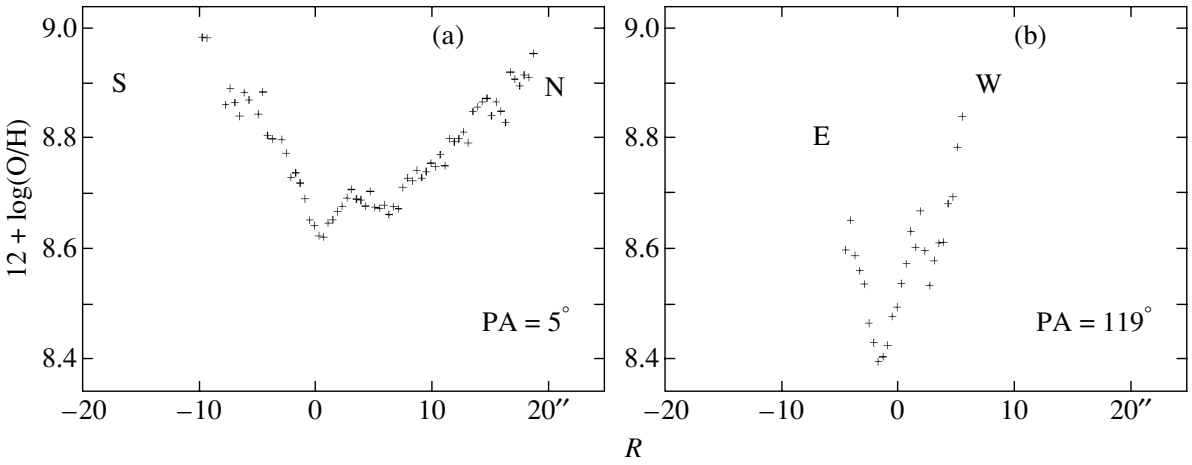


**Fig. 3.** Radial metallicity distributions.

decoupled gaseous subsystem rotating around the major axis in the nuclear region of the galaxy. The change in the line-of-sight velocity gradient yields a preliminary estimate for the location of the dynamic axis of this gaseous subsystem (PA $\approx 110°$). Its size is about $6''$ (1 kpc). At $R \geq 10''$, the line-of-sight velocity curves demonstrate the rotation of the galaxy's gaseous disk around its minor axis; the locations of the photometric axis on the periphery and the kinematic axis coincide and are close to PA $= 5°$. An improvement of the kinematic features for the two gaseous subsystems based on 2D spectroscopy will be described below.

Our comparative analysis of the line intensities shows that the line intensity ratio $I_{[\mathrm{N\,II}]\lambda 6583}/I_{\mathrm{H}\alpha}$ does not exceed 0.4 everywhere, whence it follows that the emission is produced by photoionization. In this case, we can use the empirical method described by Denicolo *et al.* (2001) to determine the metallicity:

$$12 + \log(\mathrm{O/H}) = 9.12(\pm 0.05) + 0.73(\pm 0.10) \quad (1)$$
$$\times \log(([\mathrm{S\,II}]\lambda 6716 + [\mathrm{S\,II}]\lambda 6731)/\mathrm{H}\alpha).$$

As an example, Fig. 3 shows the radial distributions of $12 + \log(\mathrm{O/H})$ for two cuts. An inner region ($r \leq 5''$) where this parameter is equal to ~8.6 and ~8.4 is distinguished in all of the distributions; farther out, it increases and reaches ~8.9 in outer regions. These values correspond to metallicities of $0.5Z_\odot$, $0.3Z_\odot$, and $0.9Z_\odot$, respectively. The spectrum along the galaxy's major axis (PA $= 5°$) passes through the brightest condensations designated by Petrosyan (1981) as "b" and "c." In these regions, $12 + \log(\mathrm{O/H}) \approx 8.6 \pm 0.1$ ($\sim 0.5Z_\odot$). The distribution constructed for PA $= 119°$ (Fig. 3b) exhibits the lowest values, $12 + \log(\mathrm{O/H}) = 8.4$ ($\sim 0.3Z_\odot$), at distances $R \lesssim 4''$ from the center. These regions are located in the area of the kinematically decoupled gaseous subsystem, and the data for them apparently suggest that the metallicity of the central subsystem is slightly lower.

## THE MORPHOLOGY OF NGC 7468

The IFP and MPFS intensity maps in the emission lines and in the continuum are shown in Fig. 4. The overall pattern of the brightness distributions in the red continuum and in the H$\alpha$ line (Figs. 4a and 4b) shows similarities, but numerous condensations of different sizes, which are probably H II regions, are distinguished more clearly in the H$\alpha$ image. Chains of H II regions are observed on the southern side of the galaxy, and the southern protrusion turns toward the brightening, where three bright condensations are distinguished. A protrusion in the H$\alpha$ brightness distribution and individual H II regions are also observed on the opposite side of the galaxy. Note that the H II regions in the central part of NGC 7468 form a ring of roughly oval shape. This structure also shows up in the continuum brightness distribution, creating the illusion of a barlike structure (Taylor *et al.* 1994).

The galaxy's outer amorphous base has roughly elliptical isophotes with close axial ratios in the continuum ($b/a \approx 0.7$) and in the H$\alpha$ line ($b/a \approx 0.65$); the geometrical center of the ellipses is $3''$ west of condensation "a." The protrusions directed northward and southward are clearly seen in the continuum brightness distribution.

The three brightenings that correspond to condensations "a," "b," and "c" noted by Petrosyan *et al.* (1978) are clearly seen in the central part of the image in the green continuum (Fig. 4c). Condensation "c" is the brightest. In the emission lines (Fig. 4), condensation "c" is poorly seen, while condensation "a" is the most prominent. This characteristic feature was noted by Petrosyan (1981).

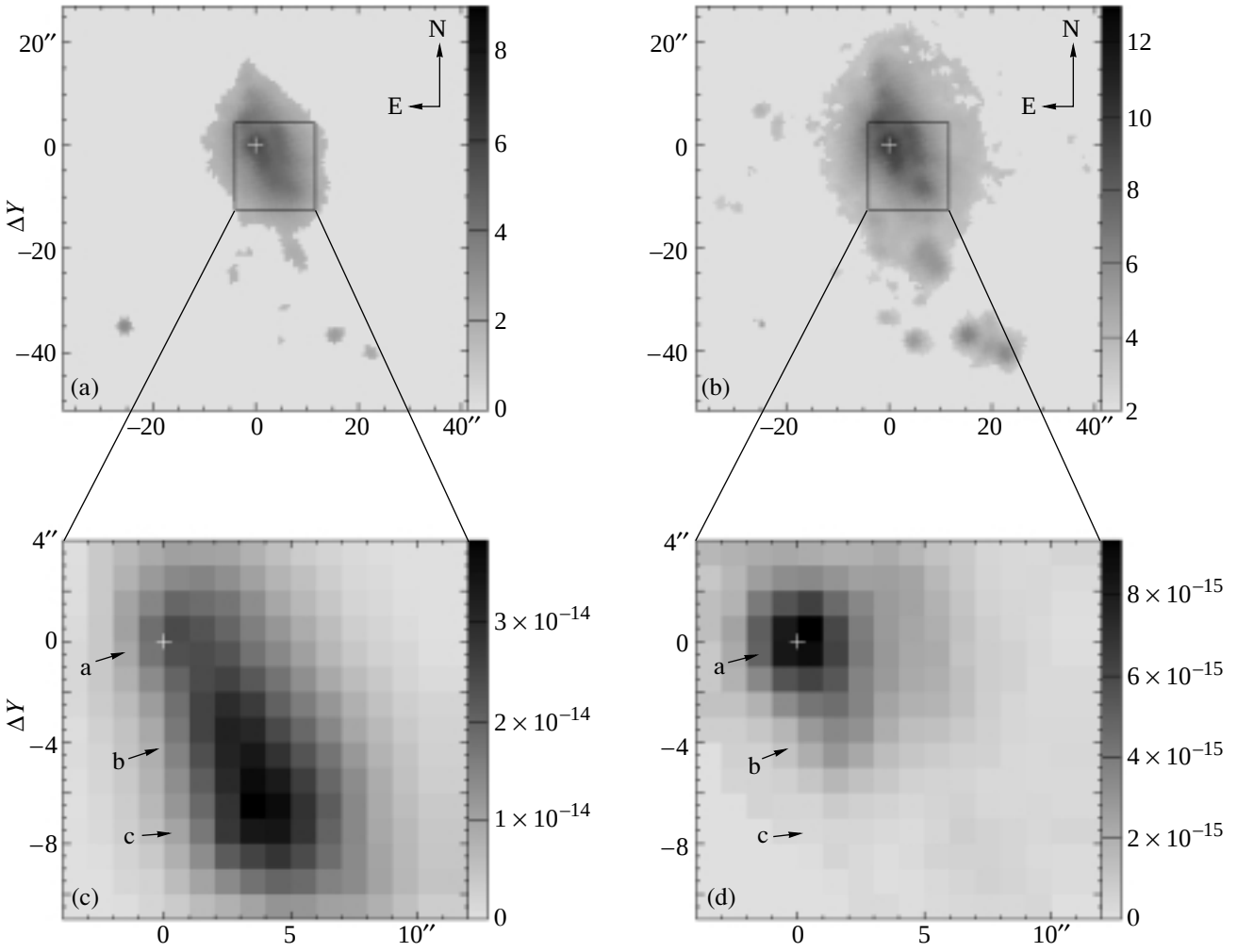


**Fig. 4.** IFP data: (a) images in the continuum near Hα; (b) an image in Hα. MPFS data: the brightness distribution (c) in the continuum (λ5400–5500) Å and (d) in the [O III]λ5007 line. The gray scale corresponds to intensities in arbitrary units for panels (a) and (b) and to intensities in erg $s^{-1}$ $cm^{-2}$ $arcsec^{-2}$ $Å^{-1}$ for panels (c) and (d). The pluses mark the position of the brightness maximum in the red continuum.

## VELOCITY FIELDS OF IONIZED GAS AND STARS

Figure 5a shows the large-scale velocity field for the emitting gas, as constructed from the IFP data, suggesting the rotation of the galaxy's gaseous disk around its minor axis. However, a feature indicating the rotation of the gas around the galaxy's major axis is clearly seen in the central part of the velocity field. Thus, the IFP data confirm the presence of two kinematic subsystems of gas in this galaxy.

If the gas is assumed to rotate in circular orbits, then the method of "tilted annuli" can be used (Begeman 1989; Moiseev and Mustsevoi 2000) to analyze the velocity field. The method allows us to determine the positions of the kinematic center and the kinematic axis (the direction of the maximum velocity gradient), to estimate the galaxy's inclination, and to construct the rotation curve. As we see from Fig. 6b, the location of the kinematic axis changes with increasing radius: $PA_{dyn} \sim 120°$ in the nuclear region ($R \lesssim 6''$) and $PA_{dyn} \backsimeq 180°$ on the periphery. This confirms the existence of two kinematic subsystems of gas. The locations of the dynamic axes of the subsystems are close to those estimated from long-slit spectra. The subsystem associated with the central region is apparently the inner disk (ring) rotating around the galaxy's major axis. The dynamic centers of the subsystems coincide, but are displaced by approximately 3″ to the W of condensation "a." The heliocentric line-of-sight velocity of the galaxy is $V_{sys} = 2070$ km $s^{-1}$ or, after being corrected for the rotation of our Galaxy, $V_{gal} = 2220$ km $s^{-1}$. The observed velocity field is best described by the model of

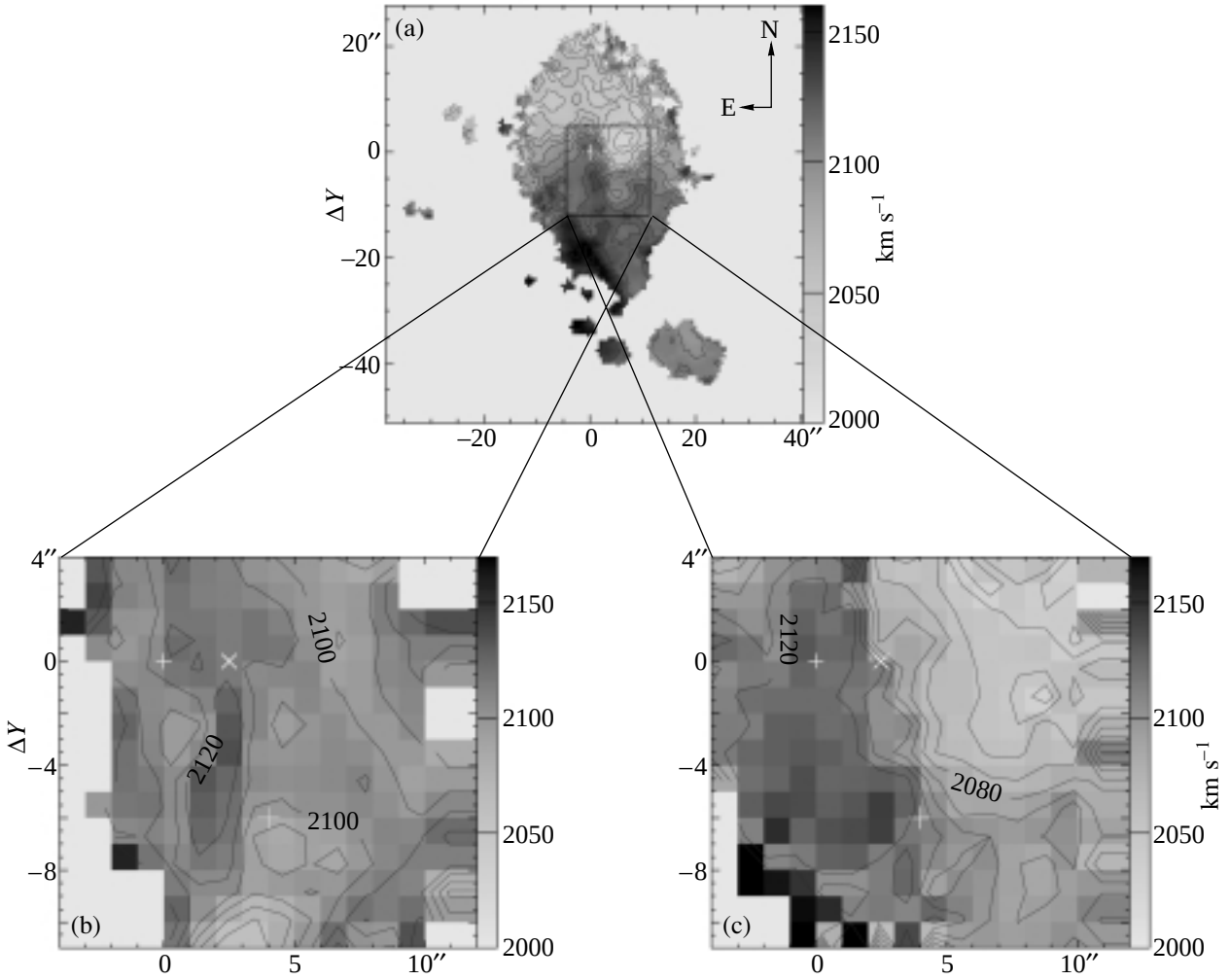


**Fig. 5.** (a) Large-scale velocity field, as inferred from IFP; (b) and (c) the velocity field of the stellar and gaseous components for the central region obtained from MPFS: the pluses indicate the positions of condensations "a" and "c" and the cross indicates the position of the dynamic center.

circular rotation at an inclination of the galactic disk $i_{\rm disk} \backsimeq 45°$ (which is equal to the estimate obtained from the galaxy's axial ratio) and that of the inner disk/ring, $i_{\rm ring} \backsimeq 60°$. Here, two values of the angle between the galactic disk and the plane of the inner disk are possible: $\Delta i \approx 50°$ and $\approx 86°$. In the first case, the orbits of the gas are unstable, and, therefore, noncircular motions must be observed in the velocity field. However, such motions have not been found, so the second value (86°) of the angle between the galactic disk and the plane of the inner disk should be taken.

The observed rotation curve of the galaxy constructed from our data (crosses) and from the H I data of Taylor *et al.* (1994) (triangles) is shown in Fig. 6a. At $R \leq 3$ kpc, the triangle lies well below the crosses. This is most likely because the 21-cm observations have a low spatial resolution ($\sim 3$ kpc). At $R \geq 3$ kpc, the discrepancy between the optical and H I data decreases and does not exceed 10 km s$^{-1}$.

The rotation curve reflects the motions in the inner disk/ring in the region $0 \leq R \leq 0.8$ kpc and the rotation of the galactic disk farther out. There is no significant jump in velocity when passing from one kinematic system to the other, which most likely suggests that the galaxy's potential is spherically symmetric on these scales.

We analyzed the observed rotation curve using the models described by Monnet and Simien (1977). At distances of 0–3 kpc, it is well represented by an exponential disk model (the dashed line in Fig. 6a) with the scale factor $h = 0.9$ kpc. This value is close to the estimates given by Evstigneeva (2000) and Cairos *et al.* (2001a), if these are recalculated to our assumed distance to the galaxy. Note that the photometric profile in the work by Evstigneeva (2000)

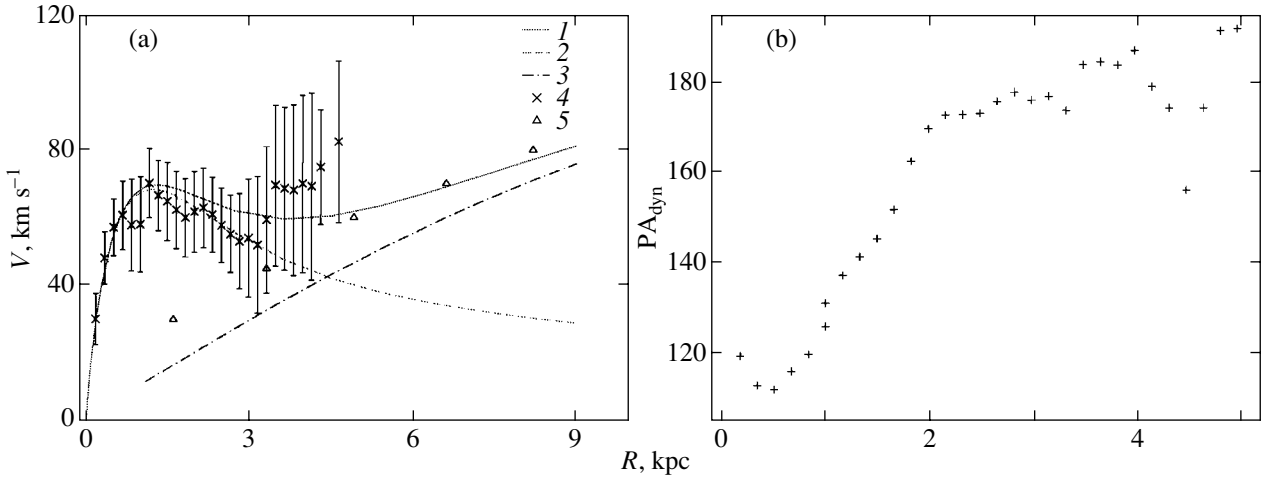


**Fig. 6.** (a) Rotation curves: (*1*) the resulting curve; (*2*) for the disk component; (*3*) for the halo; (*4*) our data; (*5*) the data from Richter *et al.* (1990). (b) The change in the location of the dynamic axis with radius.

was represented by two components: bulge + disk. However, our rotation curve does not confirm the presence of a bulge. If the galaxy actually had a bulge, then the velocity gradient in the central region would be much larger than that in our rotation curve. Therefore, we assume that the increase in brightness compared to the exponential law observed in the central part of the profiles could be due to the existence of regions of active star formation. The HI data show that the rotation curve flattens out somewhere at 8–10 kpc. Although there may be a small systematic shift between the optical and radio data, in general, the run of the rotation curve at large distances from the center ($R \geq 3$ kpc) can be explained by assuming the presence of an extended spherical isothermal halo. Its parameters were found to be the following: $r_c = 10$ kpc, $\rho_0 = 0.002 \times M_\odot$ kpc$^{-3}$. The combined theoretical rotation curve is indicated in Fig. 6a by the solid line. The overall shape of the rotation curve is characteristic of late-type galaxies (Amram and Garrido 2002). The total mass of the galaxy, including the halo, is $2 \times 10^{10} M_\odot$, and the mass of the disk/ring, assuming its radius to be 0.75 kpc, is $\sim 4 \times 10^8 M_\odot$, or 2% of the galaxy's mass.

The velocity fields for the stellar and gaseous components in the central part of the galaxy NGC 7468 are different (Figs. 5b and 5c). As we see from the figure, the ionized gas in this region rotates around the major axis, while the stellar velocity field is highly irregular. The velocity range does not exceed 40 km s$^{-1}$. The observed velocity variations can be explained by the presence of noncircular motions. It should also be noted that the contrast of the absorption features from the old stellar population is low for galaxies of late morphological types; therefore, the accuracy of the line-of-sight velocity measurements is lower than that of the usual MPFS observations of earlier-type galaxies, being 15–20 km s$^{-1}$. We attempted to describe the stellar velocity field using the method of tilted annuli with the fixed parameters PA and $i$ corresponding to those of the galaxy's outer disk. The model describes the observations satisfactorily, except for the region near condensation "a," where large residual velocities ($\sim 50$ km s$^{-1}$) are observed. We found no rotation around the major axis in the stellar velocity field. Therefore, we conclude that the stars and the gas in the galaxy's central region belong to different kinematic systems.

## DISCUSSION

As was noted in the Introduction, the putative polar ring manifests itself in the galaxy's images as protrusions on its northern and southern sides. However, analysis of the velocity field that we constructed from the IFP data and the velocity field derived from neutral hydrogen (Taylor *et al.* 1994) shows no peculiar features near these protrusions. The gas in these regions is involved in the rotation of the galactic disk around the minor axis. Here, there is no kinematically decoupled subsystem characteristic of polar rings, which forces us to reject the assumption that NGC 7468 is a galaxy with an outer polar ring.

The nature of the protrusions and the brightening in the south is not quite clear. If we assume, following Taylor *et al.* (1993), that the galaxy to the north of NGC 7468 is spatially close to it (according to this paper, the difference between their line-of-sight velocities is 73 km s$^{-1}$), then these may be considered as tidal structures, as may be evidenced by the deviations of the observed velocities from the circular ones in the region of the brightening (by 40 km s$^{-1}$) and

in the region of the southern protrusion (by approximately 20 km $s^{-1}$). On the other hand, these may be weakly developed spiral arms. Their appearance and color, bluer than that for the remaining parts of the galaxy (Cairos *et al.* 2001b), can serve as evidence for this interpretation.

At the same time, we found a kinematically decoupled gaseous subsystem, a rotating inner disk, in the central part of NGC 7468 ($\sim$1.5 kpc in diameter). The angle between the galactic disk and the plane of the inner disk is 86°. Thus, we can assert that the galaxy has an inner polar disk (possibly a ring) rather than the bar whose presence was used to explain some of the features in the velocity field constructed from the HI data (Taylor *et al.* 1994).

According to current views (Bournaud and Combes 2003), a polar structure in a galaxy can be formed either through the accretion of gas from a neighboring gas-rich galaxy during their close interaction or through the direct collision of galaxies, which can lead to the complete absorption of the less massive participant of the collision by the more massive galaxy. At the observed orientation of the inner disk, the position of the northern galaxy does not permit us to consider it a donor galaxy. Thus, we conclude that NGC 7468 collided with a low-mass gas-rich galaxy that was absorbed. As a result, a metal-poor polar gaseous disk was formed, and the observed induced star formation began in the central region of the galaxy (in a ring with a radius of $\sim$1.2 kpc). The individual condensations in this ring are spaced $\sim$500 pc–1 kpc apart. Such distances are observed between neighboring gas–dust clouds. The sizes of the condensations do not exceed 500 pc, in agreement with the sizes of stellar associations and stellar complexes. The intensity ratio of the emission lines suggests the photoionization mechanism of the emission in these regions.

Note also that the difference between the relative brightnesses of the condensations in the continuum and in the emission lines may be due to the age difference between these star-forming regions. Condensation "c," being relatively brighter in the continuum, may be an older stellar complex at a stage when the surrounding gas had already been partially swept away to large distances by strong radiative pressure and/or supernova explosions.

## CONCLUSIONS

Below, we summarize our results.

(1) Based on the long-slit spectra near H$\alpha$, we found a kinematically decoupled gaseous subsystem in the central region rotating around the galaxy's major axis.

(2) Our analysis of the line-of-sight velocity fields obtained using two-dimensional spectroscopy confirmed the existence of two kinematic subsystems of ionized gas: one of these is the gaseous disk of the galaxy, and the other is an inner disk 1.5 kpc in size. The angle between the planes of the disks is 86°; i.e., the inner disk is polar. In the central region of the galaxy, the stars and the ionized gas belong to different subsystems.

(3) The arc-shaped protrusions on the northern and southern sides of the galaxy are not kinematically distinct enough to confirm the presence of the polar ring as suggested by Whitmore *et al.* (1990). They are probably either tidal structures or weakly developed spiral arms.

(4) The intensity ratio of the forbidden and permitted lines confirms that the emission in H II regions results from photoionization. The derived metallicity is lower than the solar value ($\sim 0.3 Z_{\odot}$).

(5) The detected inner disk allows the galaxy NGC 7468 to be classified as belonging among PRGs. The central collision with a dwarf galaxy and its capture could be responsible for the formation of the inner polar disk.

## ACKNOWLEDGMENTS

We are grateful to the Commission on the Subject of Large Telescopes (CSLT) for allocating observational time on the 6-m telescope. This study was supported by the Russian Foundation for Basic Research (project nos. 02-02-16033 and 03-02-06766) and the Russian Ministry of Education (project no. E02-11.0-5).

## REFERENCES

1. V. L. Afanasiev, S. N. Dodonov, and V. L. Moiseev, *Stellar Dynamics: From Classic to Modern,* Ed. by L. P. Ossipkov and I. I. Nikiforov (Sobolev Astron. Inst., St. Petersburg, 2001), p. 103.
2. P. Amram and O. Garrido, astro-ph/0202475 (2002).
3. K. G. Begeman, Astron. Astrophys. **223**, 47 (1989).
4. F. Bournaud and F. Combes, Astron. Astrophys. **401**, 817 (2003).
5. L. M. Cairos, N. Caon, J. M. Vilchez, *et al.*, Astrophys. J., Suppl. Ser. **136**, 393 (2001b).
6. L. M. Cairos, J. M. Vilchez, G. Perez, *et al.*, Astrophys. J., Suppl. Ser. **133**, 321 (2001a).
7. G. Denicolo, R. Terlevich, and E. Terlevich, Mon. Not. R. Astron. Soc. **330**, 69 (2001).
8. E. A. Evstigneeva, Astrofizika **43**, 519 (2000).
9. W. K. Huchtmeier, L. G. Sage, and C. Henkel, Astron. Astrophys. **300**, 675 (1995).
10. A. V. Moiseev, Bull. SAO **54**, 74 (2002); astro-ph/0211104.
11. A. V. Moiseev and V. V. Mustsevoĭ, Pis'ma Astron. Zh. **26**, 657 (2000) [Astron. Lett. **26**, 565 (2000)].

12. G. Monnet and F. Simien, Astron. Astrophys. **56**, 173 (1977).
13. T. E. Nordgren, G. Helou, J. N. Chengalur, *et al.*, Astrophys. J., Suppl. Ser. **99**, 461 (1995).
14. A. R. Petrosyan, Astrofizika **17**, 421 (1981).
15. A. R. Petrosyan, K. A. Saakyan, and É. E. Khachikyan, Astrofizika **15**, 209 (1979).
16. O. R. Richter, P. D. Sackett, and L. S. Sparke, Astron. J. **107**, 99 (1994).
17. L. V. Shalyapina, A. V. Moiseev, V. A. Yakovleva, *et al.,* Pis'ma Astron. Zh. **30**, 3 (2004) [Astron. Lett. **30**, 1 (2004)].
18. C. Taylor, E. Brinks, and E. D. Skillman, Astron. J. **105**, 128 (1993).
19. C. L. Taylor, E. Brinks, R. W. Pogge, and D. E. Skillman, Astron. J. **107**, 971 (1994).
20. T. X. Thuan and G. E. Martin, Astrophys. J. **247**, 823 (1981).
21. T. Wiklind, F. Combes, and C. Henkel, Astron. Astrophys. **297**, 643 (1995).
22. B. C. Whitmore, R. A. Lucas, D. B. McElroy, *et al.*, Astron. J. **100**, 1489 (1990).
23. J. S. Young, S. Xie, J. D. P. Kenney, and W. L. Rice, Astrophys. J., Suppl. Ser. **70**, 699 (1989).

*Translated by N. Samus'*

*Astronomy Letters, Vol. 30, No. 9, 2004, pp. 593–602. Translated from Pis'ma v Astronomicheskiĭ Zhurnal, Vol. 30, No. 9, 2004, pp. 653–662.*


# Stellar Velocity Dispersion and Mass Estimation for Galactic Disks

**A. V. Zasov[1*], A. V. Khoperskov[2], and N. V. Tyurina[1]**

[1] *Sternberg Astronomical Institute, Universitetskiĭ pr. 13, Moscow, 119992 Russia*

[2] *Volgograd State University, Volgograd, 400068 Russia*

Received February 18, 2004

**Abstract**—Available velocity dispersion estimates for the old stellar population of galactic disks at galactocentric distances $r \simeq 2L$ (where $L$ is the photometric radial scale length of the disk) are used to determine the threshold local surface density of disks that are stable against gravitational perturbations. The mass of the disk $M_\mathrm{d}$ calculated under the assumption of its marginal stability is compared with the total mass $M_\mathrm{t}$ and luminosity $L_B$ of the galaxy within $r = 4L$. We corroborate the conclusion that a substantial fraction of the mass in galaxies is probably located in their dark halos. The ratio of the radial velocity dispersion to the circular velocity increases along the sequence of galactic color indices and decreases from the early to late morphological types. For most of the galaxies with large color indices $(B-V)_0 > 0.75$, which mainly belong to the S0 type, the velocity dispersion exceeds significantly the threshold value required for the disk to be stable. The reverse situation is true for spiral galaxies: the ratios $M_\mathrm{d}/L_B$ for these agree well with those expected for evolving stellar systems with the observed color indices. This suggests that the disks of spiral galaxies underwent no significant dynamical heating after they reached a quasi-equilibrium stable state. © *2004 MAIK "Nauka/Interperiodica".*

Key words: *galactic disk masses, dark halo masses, stellar velocity dispersion in galactic disks.*

## INTRODUCTION

The stellar disks of galaxies consist mostly of old stars with velocity $(c_r, c_\varphi, c_z)$ dispersions of several tens of km s$^{-1}$ in each of the three coordinates. The velocity dispersion, which characterizes the degree of dynamical heating of the system, reflects the pattern of evolution of its disk, including the conditions for its formation and the possible gravitational effects from satellites or neighboring galaxies. Nonetheless, it is not yet clear which basic physical processes are responsible for the dynamical heating of the stellar population.

The increase in the entropy of collisionless stellar systems, which manifests itself in an increase in the velocity dispersion, is a unidirectionally developing process that accumulates the effects of gravitational perturbations of the disk over its history. The existence of efficient collisionless heating mechanisms for the stellar population is evidenced by the observations of stars in the solar neighborhood that exhibit a relatively rapid increase in the stellar velocity dispersion with age: it increases by several factors in several Gyr. Whether the velocity dispersion increases continuously or this process reaches saturation at a certain level of dynamical heating is still an open question. Since any perturbations of the gravitational potential produce the strongest response in cold subsystems, the dynamical heating must be least efficient for old disk stars. There is evidence that the stellar velocity dispersion is approximately constant in the range of ages $(3–9) \times 10^9$ yr (Freeman 1991; Dehnen and Binney 1998; Quillen and Garnett 2001). However, an alternative possibility has also been discussed (Binney 2000).

The following three basic heating mechanisms for a disk in a quasi-steady state are commonly considered:

(1) The scattering of stellar orbits by massive gaseous (molecular) clouds first suggested by Spitzer and Schwartzschield (1951, 1953) and subsequently developed by a number of authors.

(2) The scattering of disk stars by the fluctuations of the gravitational potential associated with spiral density waves (Barbanis and Woltjer 1967; Sellwood and Carlberg 1984; Carlberg and Sellwood 1985; Sellwood and Lin 1989; Masset and Tagger 1997; Khoperskov *et al.* 2003).

(3) Disk heating through the tidal influence of satellites (see Huang and Carlberg (1997), Ardi *et al.* (2003) and references therein) or massive disk-crossing halo objects (Lacey and Ostriker 1985) whose existence is predicted by certain galaxy formation scenarios in CDM cosmology. In the case of

*E-mail: zasov@sai.msu.ru

the tidal mechanism, the stellar velocity dispersion increases in all three coordinates both by the direct interaction of a massive body with stars and through the excitation of bending waves in the disk (Sellwood *et al.* 1998).

The first mechanism can be efficacious only for stars that move in a layer with a thickness comparable to the thickness of the layer of molecular gas. Therefore, it is most efficient for young stars, affecting weakly the velocity dispersion of old disk stars.

The second mechanism causes the velocity dispersion to increase mainly in the plane of the disk and appears to be dominant in our Galaxy. The role of transient spiral density waves in heating the disk clearly shows up in numerical simulations where the wave amplitude decreases and the velocity dispersion ceases to increase after several disk rotations (see, e.g., Khoperskov *et al.* 2003). In our Galaxy, this mechanism could be responsible for the observed substructures in the stellar velocity field in the solar neighborhood that contain stars of various ages (De Simone *et al.* 2003).

The combined effect of the first two mechanisms allows the observed correlation of the stellar velocity dispersion (both $c_z$ and $c_r$) with the age of young stars (Jenkins and Binney 1990; Jenkins 1992) to be explained.

As regards the third mechanism mentioned above (the heating of the disk by satellites or massive halo bodies), the increase in the velocity dispersion can be quite significant and continuous (although serious difficulties in explaining the thickness of the Galactic disk arise in this case; see Ardi *et al.* 2003). However, the efficiency of this process in specific galaxies is difficult to estimate, because we know neither the number of massive objects in the halo or around the galaxy nor their mass. On the other hand, the absorption of small satellites seems quite realistic, because this process is observed both in our Galaxy and in many other galaxies. If such heating took place in the distant past, then it could be responsible for the formation of the thick Galactic disk that contains the oldest stars (Freeman 1991; Quillen and Garnett 2001). An external impact on the disk could also be responsible for the existence of thicker disks in interacting galaxies (Reshetnikov and Combes 1997; Schwartzkopf and Dettmar 2000), but it remains unknown what fraction of the galaxies have passed through the stage of close interaction.

The mechanisms under consideration can be invoked to account for the increase in the velocity dispersion of young stars with age. However, these do not answer the question of what determines the present velocity dispersion of old disk stars with ages of several billion years, or why the stellar disks of galaxies have a particular thickness that often changes only slightly with galactocentric distance, despite the fact that the efficiency of the above mechanisms must be different at different galactocentric distances.

There is a different approach to explaining the velocity dispersion of the stars that constitute the bulk of the disk mass. It is based on an analysis of the minimum possible dispersions that determine the disk stability against gravitational and bending perturbations.

Even in the absence of massive clouds and satellites or massive halo objects penetrating into the galaxy, the stellar velocity dispersion in the plane of the disk still cannot be very low. It is determined by the conditions for the stability of the disk against gravitational perturbations in its plane; i.e., it depends on the disk density and thickness, the rotation velocity and its radial derivatives. In addition, bending perturbations determine the vertical stellar velocity dispersion and the disk thickness (Polyachenko and Shukhman 1977; Mikhailova *et al.* 2001; Bizyaev *et al.* 2003; Sotnikova and Rodionov 2003).

Estimating the limiting mass of the disk at which it can be in a quasi-equilibrium steady state is the subject of this paper.

## MASS ESTIMATION FOR MARGINALLY STABLE DISKS

The radial velocity dispersion of marginally stable disks is usually written as

$$c_r = \frac{3.36G\sigma}{\varkappa}Q, \qquad (1)$$

where $\sigma$ is the surface density of the disk; $\varkappa$ is the epicyclic frequency, and $Q$ is the Toomre parameter, which is equal to unity for radial linear perturbations in a thin disk. In general, $Q$ depends on a number of factors that are difficult to take into account and can be determined either from analytical relations derived under strong simplifications or from numerical disk models. Most of the existing estimates yield $1 \lesssim Q \lesssim 3$ (see Khoperskov *et al.* (2003) for a discussion of this issue).

The vertical velocity dispersion $c_z$ increases with $c_r$ and is determined by the condition for stability against bending perturbations. In this case, the ratio $c_z/c_r$ is either determined by the initial value of $c_z$ (no bending instability develops if $c_z$ is sufficiently high) or is set during the evolution and, in this case, depends on the disk-to-halo mass ratio (Zasov *et al.* 2002). The development of bending instability and the related increase in the disk thickness were analyzed in numerical simulations of three-dimensional collisionless disks (see, e.g., Sotnikova and Rodionov (2003), Khoperskov *et al.* (2003), Bizyaev *et al.*

(2003) and references therein). Comparison of the observed thickness of the stellar disks in edge-on spiral galaxies with the expected (from numerical models of galaxies) thickness of marginally stable disks shows good agreement (Zasov *et al.* 2002). This demonstrates that the disks of these galaxies are not strongly overheated along the $z$-coordinate: $c_z$ is close to the minimum velocity dispersion required for stability.

Khoperskov (2002) attempted to use the same approach (i.e., to compare the observed stellar velocity dispersion with the values obtained for numerical steady-state models) to analyze the radial velocity dispersion rather than the vertical one. He assumed that the observed central stellar velocity dispersion pertains to the disk or is at least no lower than the central velocity dispersion of the disk component. In many cases, the limiting disk mass was shown to be several times smaller than the total mass of the galaxy. However, the results of this approach depend strongly on the adopted model of the galaxy, and the predominance of a bright bulge in the central parts of many galaxies significantly complicates the formulated problem.

In this paper, we use a slightly different method. We estimate the mass $M_\mathrm{d}$ of a disk with an exponential density profile by assuming it to be marginally stable for galaxies with available estimates of the stellar velocity dispersion at sufficiently large galactocentric distances in the region $(1.5–2) \times L$ ($L$ is the photometric disk scale length). In general, the derived $M_\mathrm{d}$ may be considered as an upper limit for the mass of an equilibrium quasi-steady disk.

The numerical $N$-body models applied to marginally stable three-dimensional disks show that the stability parameter $Q$ (which generally varies along the disk radius by several factors) has a minimum dispersion at $r \simeq 1.5L–2L$ and is equal to $Q \simeq 1.5$ for various mass distributions in the bulge, the disk, and the halo. It is important to note that the scatter of values $\Delta Q \simeq 0.2$ is at a minimum at this galactocentric distance. Therefore, having estimated $c_r$ from the observed velocity dispersion at $r \simeq 2L$ and taking $Q_\mathrm{T} = 1.5$, we can easily obtain an upper limit on the local density of the disk at this galactocentric distance and restore the upper limit on the disk mass from the known radial scale length.

The velocity dispersion of old disk stars in galaxies is difficult to measure spectroscopically at large galactocentric distances, at which the influence of the bulge is no longer significant. This is primarily because the surface brightness of the disk is low (it is generally $21^m – 23^m/\square''$ in the red ($R$) band at $r \simeq 2L$). Furthermore, observations yield only estimates of the line-of-sight velocity dispersion that can differ from $c_r$ by a factor of 1.5–2. The velocity dispersions were reliably measured along both the major and minor axes of the disk only for a few galaxies for which it is possible to separate the vertical and radial dispersions and to estimate $c_r$ through simple geometrical transformations (Shapiro *et al.* 2003).

Below, we list the main sources of errors in estimating the mass of a marginally stable disk:

(1) The measurement errors of the velocity dispersion at $r \simeq 2L$, which are particularly significant in the cases of a low dispersion;

(2) The errors of the allowance for geometric factors in recalculating the observed velocity dispersion $c_\mathrm{obs}$ to $c_r$, which are particularly significant for galaxies with small inclinations $i$ of the rotation axis to the line of sight;

(3) The errors in the estimated circular velocity at $r = 2L$ and, for the rotation curves of the stellar component, the errors of the allowance for the velocity dispersion in estimating the circular velocity in the asymptotic drift approximation (van den Kruit and Freeman 1986; Bottema 1992);

(4) The errors in the radial scale $L$ of the disk density estimated by assuming that the density is proportional to the brightness of the stellar disk.

As a result of the above factors, the individual estimates of the limiting disk masses inferred from the velocity dispersion have a low accuracy. Since the critical disk density is proportional to $c_r$, the probable error of $c_r$ gives an idea of the accuracy of the disk mass estimate (see Table 1). The error can exceed a factor of 1.5—2 for galaxies with the lowest values of $c_\mathrm{obs}$ or those seen nearly face-on. However, even this accuracy does not hinder a comparison of various galaxies provided that the sample is sufficiently large.

Following (1), we write the expression for the surface density of the disk at $r = 2L$ as

$$\sigma(2L) = \frac{kc_rV_\mathrm{c}}{7.72LGQ}, \tag{2}$$

or

$$\sigma(2L)[M_\odot/\mathrm{pc}^2] = 6.9 \times 10^{-2}\frac{kc_r[\mathrm{km\ s}^{-1}]V_\mathrm{c}[\mathrm{km\ s}^{-1}]}{2QL[\mathrm{kpc}]}, \tag{3}$$

where $k = \varkappa/\Omega$ (the values of this parameter lie within the range from 2 for rigid rotation to $\sqrt{2}$ for the plateau on the rotation curve), and $V_\mathrm{c}$ and $Q$ pertain to the radial coordinate $r = 2L$. Below, we assume that $Q(2L) = 1.5$ (see above) and that the parameter $k$ is equal to $\sqrt{2}$ for galaxies with an approximately constant velocity $V_\mathrm{c}$ at $r \simeq 2L$ (which is true in almost all cases) and 1.8 for galaxies with a rising rotation curves in this region (the latter applies to NGC 2613, NGC 6340, and NGC 6503).

**Table 1.** Sample of galaxies

| Galaxy | Type | $D$, Mpc | $i$ | $c_{\rm obs}$, km s$^{-1}$ | | $V_{\rm c}(2L)$, km s$^{-1}$ | $L$ | |
|---|---|---|---|---|---|---|---|---|
| NGC 1068 | 3 | 15.2 | 30° | $50 \pm 10$ | (1) | 251 | 55″.6 | (9) |
| NGC 2460 | 1 | 19.2 | 46 | $60 \pm 10$ | (1) | 200 | 15 | (1) |
| NGC 2775 | 2 | 18 | 40 | $60 \pm 15$ | (1) | 283 | 35 | (1) |
| NGC 4030 | 2 | 19.5 | 40 | $55 \pm 10$ | (1) | 249 | 18 | (1) |
| NGC 3982 | 3 | 15.8 | 30.4 | $45 \pm 10$ | (2) | 200 | 10.2 | (9) |
| NGC 1566 | 4 | 17.5 | 28 | $20 \pm 10$ | (3) | 181 | 35.7 | (3) |
| NGC 2613 | 3 | 19.2 | 90 | $36 \pm 25$ | (3) | 300 | 57.3 | (3, 9) |
| NGC 3198 | 5 | 12.2 | 70 | $20 \pm 15$ | (3) | 180 | 58 | (3) |
| NGC 5247 | 4 | 15.3 | 43 | $20 \pm 10$ | (3) | 83 | 40 | (3) |
| NGC 6340 | 0 | 19.1 | 26 | $35 \pm 15$ | (3) | 163 | 28 | (3) |
| NGC 6503 | 6 | 5.9 | 71 | $18 \pm 10$ | (3) | 112 | 40 | (3) |
| IC 750 | 2 | 12.9 | 71 | $70 \pm 30$ | (4) | 170 | 14.2 | (9) |
| NGC 470 | 3 | 33.9 | 60 | $40 \pm 20$ | (5) | 185 | 13.6 | (10) |
| NGC 4419 | 1 | 14 | 71 | $60 \pm 20$ | (5) | 148 | 12.8 | (9) |
| NGC 7782 | 3 | 74.6 | 58 | $45 \pm 15$ | (5) | 295 | 18.3 | (9) |
| NGC 2962 | −1 | 24.1 | 59 | $60 \pm 20$ | (6) | 209 | 22.3 | (9) |
| NGC 3630 | −1 | 17.4 | 90 | $80 \pm 20$ | (6) | 186 | 8.3 | (9) |
| NGC 4143 | −2 | 12.7 | 60 | $60 \pm 15$ | (7) | 235 | 15.4 | (9) |
| NGC 4203 | −3 | 14.3 | 55 | $50 \pm 20$ | (7) | 92 | 17.2 | (9) |
| NGC 4578 | −2 | 14 | 50 | $60 \pm 15$ | (7) | 136 | 10.3 | (9) |
| NGC 5273 | −2 | 15.1 | 44 | $50 \pm 15$ | (7) | 105 | 9.2 | (9) |
| Galaxy | 4 | − | 90 | − | | 200 | (3 kpc) | See text |
| NGC 584 | −4 | 25.5 | 90 | $80 \pm 40$ | (8) | 215 | 8.5 | (8) |
| NGC 2549 | −2 | 15.8 | 90 | $50 \pm 20$ | (8) | 153 | 20.2 | (8) |
| NGC 2768 | −4 | 20.4 | 90 | $73 \pm 20$ | (8) | 138 | 44.8 | (8) |
| NGC 3489 | −1 | 10.8 | 60 | $78 \pm 22$ | (8) | 137 | 19.4 | (8) |
| NGC 4251 | −2 | 13.5 | 68 | $86 \pm 20$ | (8) | 135 | 22.6 | (8) |
| NGC 4649 | −4 | 14 | 49 | $186 \pm 59$ | (8) | 227 | 29.6 | (8) |
| NGC 4753 | −2 | 16.3 | 71 | $50 \pm 25$ | (8) | 185 | 34.8 | (8) |
| NGC 5866 | −1 | 11.9 | 75 | $100 \pm 20$ | (8) | 217 | 21 | (8) |

Note: (1) Shapiro *et al.* (2003), (2) Bershady *et al.* (2002), (3) Bottema (1993), (4) Heraudeau *et al.* (1999), (5) Beltran *et al.* (2001), (6) Simien and Prugniel (2000), (7) Simien and Prugniel (2002), (8) Neistein *et al.* (1999), (9) Baggett *et al.* (1998), (10) Grosbol (1985).

The surface density estimate (3) allows the mass of a disk with an exponential density profile to be easily determined:

$$M_{\rm d} = 2\pi L^2 \sigma(2L) e^2. \quad (4)$$

The mass of the disk within a fixed galactocentric distance of $R = 4L$ that roughly corresponds to the optical disk boundary is equal to $0.95M_{\rm d}$.

Table 1 lists the galaxies used here and their assumed parameters. This table gives the following:

(1) The galaxy name;

(2) The morphological type (from the LEDA database) in the notation of de Vaucouleurs. $T = -1, 1, 3, 5$, and 7 correspond to S0, Sa, Sb, Sc, and Sd galaxies, respectively;

(3) The assumed distances $D$ to the galaxies. For galaxies with radial velocities $V_r > 800$ km s$^{-1}$, the distances correspond to the Hubble constant $H_0 = 75$ km s$^{-1}$ Mpc$^{-1}$ (except for the galaxies of the Virgo cluster, for which we assumed that $D = 14$ Mpc). For nearby galaxies with lower radial velocities (NGC 3198, NGC 6503, and IC 750), we used the distance moduli from the LEDA database.

(4) The disk inclination $i$. We took its values from LEDA, except NGC 1566, for which Bottema (1992) gave a greatly differing estimate of $i$ (28° instead of 44°) and the galaxies with directly estimated radial velocity dispersions (Shapiro *et al.* 2003) (for these, we use the $i$ values from the cited paper);

(5) The observed velocity dispersions at $r \simeq 2L$ (along the major axis) and the corresponding reference. The errors, if these were not given in the original paper, were determined visually from the scatter of data points on the plot and are only a rough estimate of the accuracy. The velocity dispersion for our Galaxy is referenced to the $c_r = 38$ km s$^{-1}$ that was determined for the solar neighborhood (Dehnen and Binney 1998) at an assumed Galactocentric distance of $R = 8$ kpc $\simeq 2.7L$;

(6) The assumed circular rotation velocities $V_{\rm c}$ at $r \simeq 2L$ (the data for the rotation curves of the stellar component were corrected for the stellar velocity dispersion). We failed to find any rotation curve for NGC 5247 and assumed $V_{\rm c}(2L)$ to be equal to the maximum rotation velocity $V_{\rm m}$ based on the HI radio line width (from LEDA);

(7) The photometric disk scale length (in arcsec) and the corresponding reference.

For most of the galaxies, $c_{\rm obs}$ was estimated at points on the major axis. In this case, the following equation holds:

$$c_{\rm obs}^2 = c_\varphi^2 \sin^2 i + {c_z}^2 \cos^2 i, \quad (5)$$

**Table 2.** Mass estimates for the marginally stable disks of galaxies

| Galaxy | $M_{\rm d}/M_\odot$ | $M_{\rm d}/M_{\rm t}$ | $M_{\rm d}/L_B$ | $(B-V)_0$ |
|---|---|---|---|---|
| NGC 1068 | $7.1 \times 10^{10}$ | 0.29 | 2.2 | 0.7 |
| NGC 2460 | $3.5 \times 10^{10}$ | 0.67 | 5.2 | 0.81 |
| NGC 2775 | $5.5 \times 10^{10}$ | 0.24 | 2.2 | 0.84 |
| NGC 4030 | $5.2 \times 10^{10}$ | 0.53 | 3.1 | – |
| NGC 3982 | $2.1 \times 10^{10}$ | 0.72 | 3.1 | – |
| NGC 1566 | $3.0 \times 10^{10}$ | 0.32 | 0.6 | 0.58 |
| NGC 2613 | $1.2 \times 10^{11}$ | 0.27 | 2.0 | 0.7 |
| NGC 3198 | $2.7 \times 10^{10}$ | 0.26 | 1.4 | 0.43 |
| NGC 5247 | $1.2 \times 10^{10}$ | 0.65 | 0.6 | 0.42 |
| NGC 6340 | $4.7 \times 10^{10}$ | 0.74 | 3.9 | 0.79 |
| NGC 6503 | $5.1 \times 10^{9}$ | 0.38 | 0.9 | 0.57 |
| IC 750 | $2.3 \times 10^{10}$ | 0.97 | 8.2 | 0.91 |
| NGC 470 | $3.8 \times 10^{10}$ | 0.53 | 1.3 | 0.65 |
| NGC 4419 | $1.7 \times 10^{10}$ | 0.95 | 2.2 | 0.81 |
| NGC 7782 | $2.0 \times 10^{11}$ | 0.38 | 2.3 | 0.72 |
| NGC 2962 | $7.5 \times 10^{10}$ | 0.71 | 10.1 | 0.93 |
| NGC 3630 | $2.2 \times 10^{10}$ | 0.99 | 9.3 | – |
| NGC 4143 | $3.0 \times 10^{10}$ | 0.63 | 5.8 | – |
| NGC 4203 | $1.3 \times 10^{10}$ | 1.36 | 2.1 | 0.91 |
| NGC 4578 | $1.4 \times 10^{10}$ | 1.14 | 3.8 | 0.81 |
| NGC 5273 | $8.8 \times 10^{9}$ | 1.26 | 2.4 | 0.82 |
| Galaxy | $4.8 \times 10^{10}$ | 0.43 | – | (0.57) |
| NGC 584 | $3.9 \times 10^{10}$ | 0.85 | 1.3 | 0.9 |
| NGC 2549 | $2.5 \times 10^{10}$ | 0.75 | 3.4 | 0.85 |
| NGC 2768 | $9.5 \times 10^{10}$ | 1.22 | 2.9 | 0.91 |
| NGC 3489 | $2.5 \times 10^{10}$ | 1.39 | 3.3 | 0.78 |
| NGC 4251 | $3.8 \times 10^{10}$ | 1.52 | 6.3 | 0.8 |
| NGC 4649 | $2.0 \times 10^{11}$ | 2.12 | 5.0 | 0.93 |
| NGC 4753 | $5.6 \times 10^{10}$ | 0.64 | 3.2 | 0.82 |
| NGC 5866 | $5.7 \times 10^{10}$ | 1.08 | 4.8 | 0.79 |

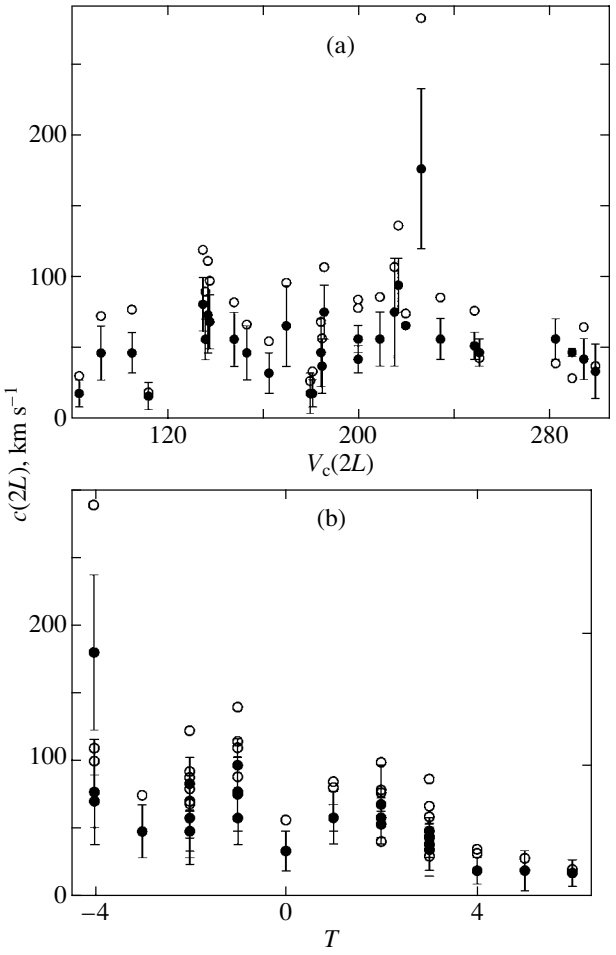


**Fig. 1.** Comparison of the velocity dispersion at $r = 2L$ with the circular velocity $V_c$ at the same galactocentric distance (a) and with the morphological type $T$ of the galaxy (b): the filled and open symbols represent the observed dispersions ($c_{obs}$) and the corresponding radial velocities ($c_r$) estimated from $c_{obs}$, respectively.

whence

$$c_r = c_{obs}\left[(c_\varphi/c_r)^2\sin^2 i + (c_z/c_r)^2\cos^2 i\right]^{-1/2}. \quad (6)$$

When going from $c_{obs}$ to $c_r$ in (6), we assumed that $c_\varphi/c_r = \varkappa/2\Omega$ (the epicyclic approximation) and $c_z/c_r \simeq 1/2$. Unfortunately, observational estimates of $c_z/c_r$ are available only for a few galaxies. These ratios lie within the range 0.5–0.8 and tend to increase from Sc–Sd toward Sa (Shapiro *et al.* 2003), but the available data are clearly insufficient to confidently relate $c_z/c_r$ to a morphological type. In any case, the possible error in $c_z/c_r$ has little effect on the resulting estimate of $c_r$ obtained from formula (6). For the galaxies whose stellar velocity dispersion was determined along both the major and minor axes (Shapiro *et al.* 2003), we used the model estimates of $c_r$ from the cited paper.

We estimated the rotation velocity of the disk at $r \simeq 2L$ from the rotation curve of the gas, if available (with an allowance made for the adopted inclination $i$). If the original paper gave only the velocity of the stellar component, then we applied a correction for the radial velocity dispersion in the asymptotic drift approximation for $r = 2L$ by assuming that $r\partial\ln(c_r^2)/\partial r = -1$. For the galaxies for which the corrected velocities at $r \simeq 2L$ were given in the original paper (Neistein *et al.* 1999), we used these to estimate the local disk density (this applies to NGC 2549, NGC 2768, NGC 3489, NGC 4251, NGC 4649, and NGC 4573).

Table 2 gives the resulting estimates of the total mass $M_d$ of the disk that is marginally stable at $r = 2L$. This table also gives the derived ratios of the disk mass to the total mass of the galaxy (in solar units) within $R = 4L$. The latter was roughly estimated using the relation $M_t = 4V_c^2 L/G$.

The fourth column in Table 2 gives the ratios of the disk mass to the total luminosity of the galaxy. For spiral galaxies, this ratio is close to the $M_d/L_B$ ratio for the stellar population of the disk, because the bulge contributes only slightly to the total luminosity. However, the presence of a bulge can be important for lenticular galaxies; therefore, the $M_d/L_B$ ratio may be considered only as a lower limit of the corresponding ratio for the disk. The last column gives the corrected (for the disk inclination and Galactic extinction) color indices of the galaxies (from LEDA). For our Galaxy, we adopted the mean color index for type $T = 4$ (Buta *et al.* 1994).

## DISCUSSION AND CONCLUSIONS

It follows from Fig. 1a that there is virtually no correlation between the circular velocity $V_c$ and the velocity dispersion $c_r$ or $c_{obs}$ at a chosen galactocentric distance $r \simeq 2L$. Therefore, we cannot estimate $c_r$ empirically from the rotation velocity, which is known for a very large number of galaxies. However, there is a weak correlation between $c_r$ and the morphological type (Fig. 1b). Early-type galaxies have, on average, higher velocity dispersions at $r = 2L$. The elliptical (or lenticular) galaxy NGC 4649 with a rotating stellar subsystem stands out on the diagrams. Since its velocity dispersion exceeds significantly the rotation velocity, rotation does not play a major role in the equilibrium of the disk. Therefore, we excluded this galaxy from our analysis when estimating the disk masses.

It is convenient to characterize the role of rotation in the equilibrium of the disk by the ratio of the radial

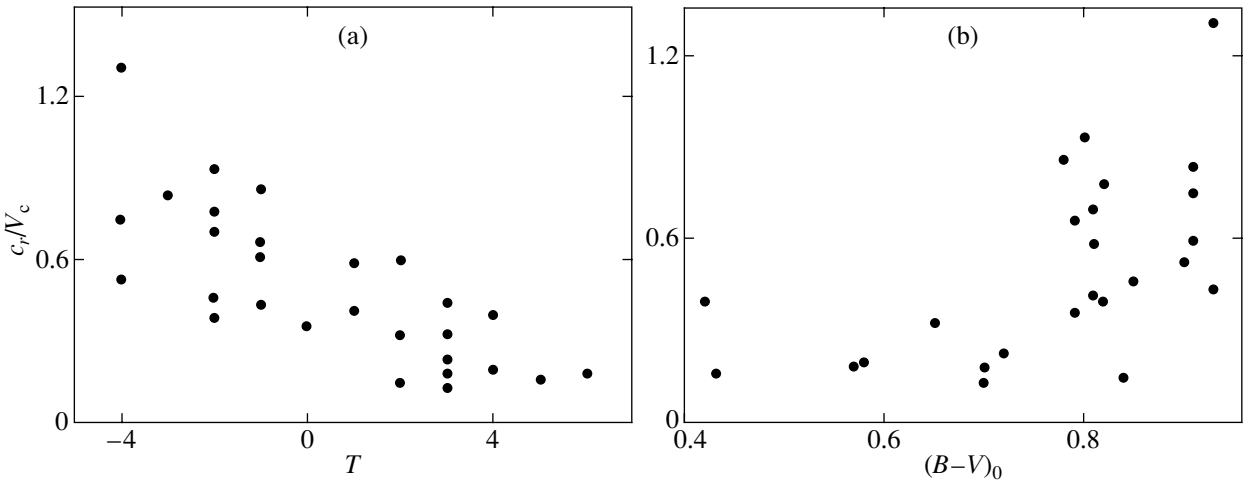


**Fig. 2.** Comparison of the $c_r/V_c$ ratio with the morphological type (a) and the total color index of the galaxy (b).

velocity dispersion to the circular rotation velocity. In Figs. 2a and 2b, the ratio $c_r/V_c$ is compared with the morphological type and the color index $(B-V)_0$. Here, we clearly see a correlation between the quantities being compared. The dependence $c_r/V_c(T)$ (Fig. 2a) indicates that rotation in late-type galaxies plays a more important role in maintaining the equilibrium of the old stellar disk than it does in Sa–S0 galaxies.

The diagram in Fig. 2b shows that the dynamically cold disks are distinguished by more intense star formation, as evidenced by their bluer colors. On the other hand, the red galaxies (Sa–S0 dominate among them) exhibit a large dispersion of their kinematic properties, and there are many strongly overheated systems with high ratios $c_r/V_c$. The boundary between the cold and hot disks corresponds to $(B-V)_0 \simeq 0.75$.

Figure 3 shows the local disk densities at the chosen galactocentric distance calculated using formula (2) compared with the total color indices of the galaxies. A group of red galaxies (almost all of them are of the S0 type) with anomalously high critical disk densities exceeding $400 M_\odot/\mathrm{pc}^2$ clearly stands out, while $\sigma(2L)$ for most of the remaining galaxies lies within the range 50–200 $M_\odot/\mathrm{pc}^2$. For comparison: the density of the disk of our Galaxy does not exceed $60 M_\odot/\mathrm{pc}^2$ in the solar neighborhood (Khoperskov and Tyurina 2003). This suggests that the observed stellar velocity dispersion in some of the galaxies significantly exceeds the minimum value required for the disk to be stable.

A similar picture is observed when the relative mass of the disk calculated by assuming it to be marginally stable is compared with the morphological type and the color index of the galaxies (Figs. 4a and 4b). Recall that, in general, $M_d$ is an upper limit for the mass of the disk, because the stellar velocity dispersion in the galactic disk can exceed the minimum value required for it to be stable. The horizontal line separates the objects with $M_d/M_t > 1$. The latter inequality has no physical meaning and suggests only that the assumption of marginal disk stability for these galaxies is inconsistent with the adopted value of $c_r$. Either these galaxies have strongly heated (with a large stability margin) disks or their $c_r$ estimates were affected by stars of the bulge, which is hotter than the disk. Both variants are possible, and the

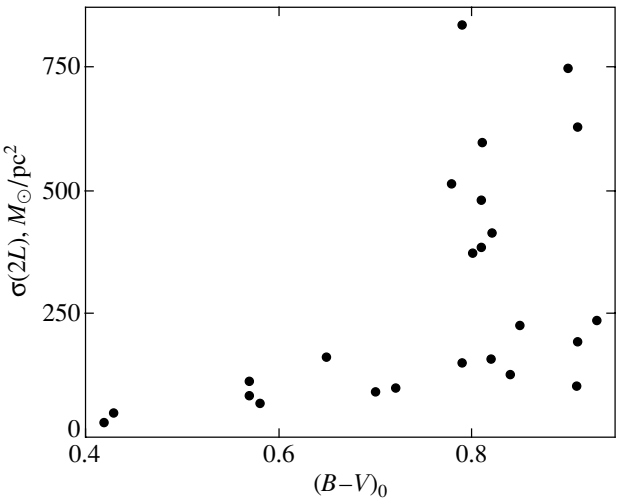


**Fig. 3.** Comparison of the local disk densities at $r \simeq 2L$ calculated by assuming the disk to be marginally stable with the total color indices of the galaxies. A group of "red" galaxies for which $\sigma(2L)$ appears to have been highly overestimated stands out.

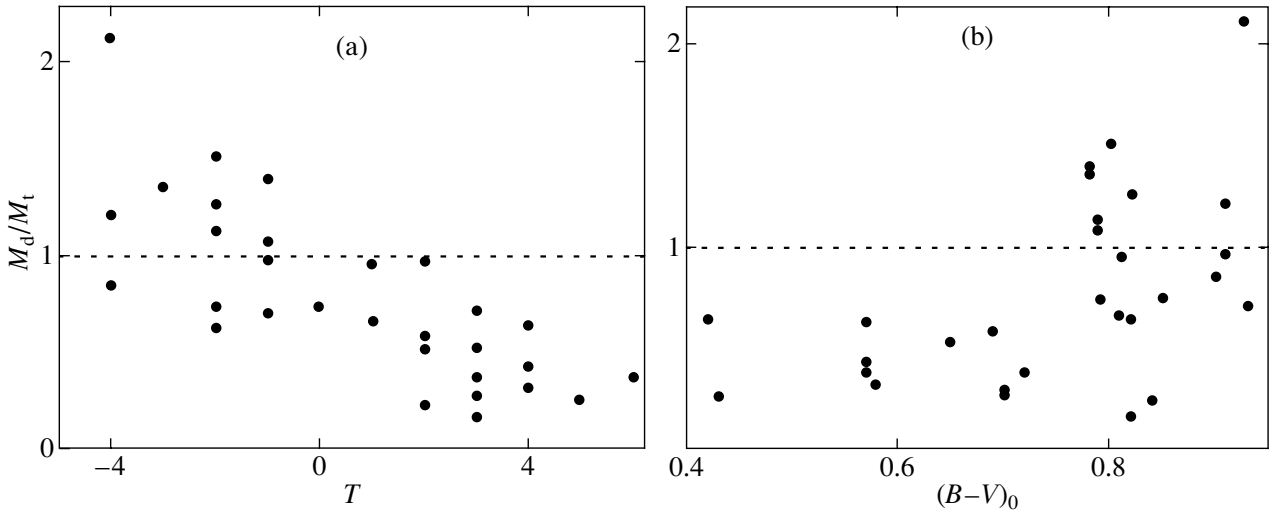


**Fig. 4.** Comparison of the ratio of the mass of a marginally stable disk to the total mass of the galaxy $M_d/M_t$ within $r = 4L$ with (a) the morphological type and (b) the total color index of the galaxy

question should be solved individually for each galaxy. Note, however, that in the radial profile $c_{obs}(r)$, the inner, bulge-dominated parts of the galaxy generally differ markedly from the adjacent disk regions, where the velocity dispersion is lower and slowly decreases with $r$ (see, e.g., Simne and Prugniel 2002, 2003). In the galaxies with $M_d/M_t > 1$ considered here (except NGC 3489), the region $r \simeq 2L$ falls within the "disk" portion of $c_{obs}(r)$ or the transition region, which provides circumstantial evidence that the observed velocity dispersion is not strongly affected by the bulge, at least in some of the galaxies.

For certain galaxies, we can check whether the estimate $M_d/M_t > 1$ is the result of overestimating $c_{obs}(2L)$ using available measurements. For three lenticular galaxies with $M_d/M_t > 1$ (NGC 4251, NGC 4578, and NGC 5273), the velocity dispersions were estimated up to $r/L = 3.6, 3.3$, and 3.1, respectively, i.e., up to the galactocentric distances where the bulge effect must be much weaker than at $2L$. Although the uncertainty in the parameter $Q$ increases at large $r$, we can assume that the condition $Q < 3$ is still satisfied for these limiting distances and, thus, can estimate the lower limit for $M_d$. We found that even in this case, the ratio $M_d/M_t$ exceeds unity for the listed galaxies (1.3, 2.0, and 1.2, respectively); i.e., the conclusion that their disks are overheated remains valid.

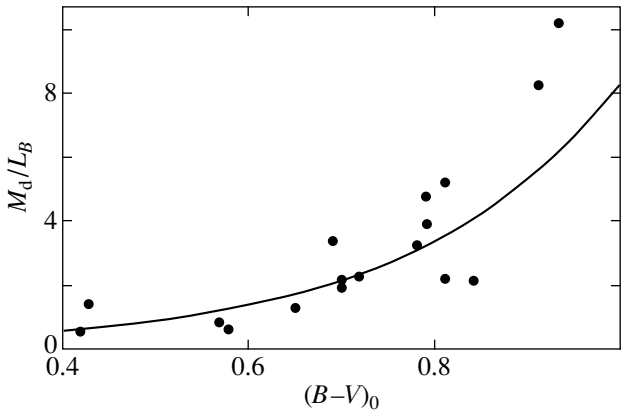


**Fig. 5.** Correlation of the ratio of the mass of a marginally stable disk to the total luminosity of the galaxy with the total color index of the galaxy. The curve indicates an analytical fit to the dependence obtained by the method of evolutionary modeling of stellar systems (according to Bell and de Jong (2001)).

The situation with spiral galaxies is different. The condition $M_d/M_t < 1$ is satisfied for most of them, but it does not follow from its satisfaction that the velocity dispersion in their disks is close to the minimum value required for them to be gravitationally stable. Here, independent estimates for the disk masses are required.

To compare $M_d$ with the values expected for a given luminosity of the galaxy, Fig. 5 shows the "$M_d/L_B$—color index" diagram for the spiral galaxies of the sample under consideration. Clearly, the ratio $M_d/L_B$ for the stellar population (which is generally equal to several solar units) increases with a decreasing contribution of young stars to the total luminosity, i.e., with an increasing color index. In this case, the relation between $M_d/L_B$ and the color depends weakly on the history of star formation in the galaxy (Bell and de Jong 2001). The curve in Fig. 5 indicates the dependence computed for a modified

Salpeter initial mass function and given in analytical form in the cited paper[1]. The reddest galaxies are IC 750 (Sab) and NGC 2962 (S0a). Despite the significant scatter of data points in Fig. 5 about the model curve, we may conclude that the disk mass estimates satisfying the marginal stability condition are in quantitative agreement with those expected for the given color and luminosity. This is a strong argument that the stellar velocity dispersion in the disks of spiral galaxies is close to the minimum value required for the disks to be stable in most cases. It thus follows that the mechanisms of slow dynamical heating of the stationary disks in the spiral galaxies considered are not efficient enough to cause a significant increase in the velocity dispersion over their lifetimes.

As we pointed out above, the stellar disks in early-type galaxies appear to be often strongly overheated. This primarily follows from the unacceptably high local densities and total disk masses estimated by assuming the disks to be marginally stable. In this case, there is a clear correlation between the high velocity dispersion and the low star formation rate. Indeed, the relative velocity dispersion $c_r/V$ systematically increases with the galaxy color index (Fig. 2b), with all galaxies with $M_\mathrm{d}/M_\mathrm{t} > 1$ having the color of the old stellar population ($(B-V)_0 > 0.75$). The weak star formation at the current epoch appears to be attributable to such events in the history of these galaxies that have simultaneously resulted both in the dynamical heating of the stellar disk and in an enhanced rate of gas depletion and, hence, in the high color indices. This may be assumed to be associated with tidal effects or the accretion of small stellar systems.

## ACKNOWLEDGMENTS

This work was supported by the Russian Foundation for Basic Research (project no. 04-02-16518 and, in part, project no. 04-02-96500).

## REFERENCES

1. E. Ardi, T. Tsuchiya, and T. Burket, Astrophys. J. **596**, 204 (2003).
2. W. E. Baggett, S. M. Baggett, and K. S. J. Anderson, Astron. J. **116**, 1626 (1998).
3. B. Barbanis and L. Woltjer, Astrophys. J. **150**, 461 (1967).
4. E. Bell and R. S. de Jong, Astrophys. J. **550**, 212 (2001).
5. J. C. V. Beltran, A. Pizzella, E. M. Corsini, *et al.*, Astron. Astrophys. **374**, 391 (2001).
6. M. Bershady, M. Verheijen, and D. A. Anders, ASP Conf. Proc. **275**, 43 (2002).
7. J. Binney, ASP Conf. Ser. **230**, 63 (2000).
8. D. V. Bizyaev, A. V. Khoperskov, and N. V. Tiurina, Am. Astron. Soc. Meet. **202**, 40.13 (2003); astro-ph/0306193.
9. R. Bottema, Astron. Astrophys. **257**, 69 (1992).
10. R. Bottema, Astron. Astrophys. **275**, 16 (1993).
11. R. Buta, S. Mitra, G. de Vaucouleurs, and H. G. Corwin, Astron. J. **107**, 118 (1994).
12. R. G. Carlberg and J. A. Sellwood, Astrophys. J. **292**, 79 (1985).
13. W. Dehnen and J. J. Binney, Mon. Not. R. Astron. Soc. **298**, 387 (1998).
14. K. C. Freeman, *Dynamics of Disc Galaxies,* Ed. by B. Sundelius (Goteborg, Sweden, 1991), p. 15.
15. P. J. Grosbol, Astron. Astrophys., Suppl. Ser. **60**, 261 (1985).
16. Ph. Heraudeau, F. Simien, G. Maubon, and Ph. Prugniel, Astron. Astrophys., Suppl. Ser. **136**, 509 (1999).
17. S. Huang and R. G. Carlberg, Astrophys. J. **480**, 503 (1997).
18. A. Jenkins, Mon. Not. R. Astron. Soc. **257**, 620 (1992).
19. A. Jenkins and J. Binney, Mon. Not. R. Astron. Soc. **245**, 305 (1990).
20. A. V. Khoperskov, Pis'ma Astron. Zh. **28**, 723 (2002) [Astron. Lett. **28**, 651 (2002)].
21. A. V. Khoperskov and N. V. Tyurina, Astron. Zh. **80**, 483 (2003) [Astron. Rep. **47**, 443 (2003)].
22. A. V. Khoperskov, A. V. Zasov, and N. V. Tyurina, Astron. Zh. **80**, 387 (2003) [Astron. Rep. **47**, 357 (2003)].
23. P. C. van der Kruit and K. C. Freeman, Astrophys. J. **303**, 556 (1986).
24. C. Lacey and J. P. Ostriker, Astrophys. J. **299**, 633 (1985).
25. F. Masset and M. Tagger, Astron. Astrophys. **322**, 442 (1997).
26. E. A. Mikhailova, A. V. Khoperskov, and S. S. Sharpak, *Stellar Dynamics: from Classic to Modern,* Ed. by L. P. Ossipkov and I. I. Nikiforov (St. Petersburg, 2001), p. 147.
27. E. Neistein, D. Maoz, H.-W. Rix, and J. L. Tonry, Astron. J. **117**, 2666 (1999).
28. V. L. Polyachenko and I. G. Shukhman, Pis'ma Astron. Zh. **3**, 254 (1977) [Sov. Astron. Lett. **3**, 134 (1977)].
29. A. C. Quillen and D. R. Garnett, ASP Conf. Ser. **230**, 87 (2001).
30. V. Reshetnikov and F. Combes, Astron. Astrophys. **324**, 80 (1997).
31. U. Schwarzkopf and R.-J. Dettmar, Astron. Astrophys., Suppl. Ser. **144**, 85 (2000).
32. J. A. Sellwood and R. G. Carlberg, Astrophys. J. **282**, 61 (1984).
33. J. A. Sellwood and D. N. C. Lin, Mon. Not. R. Astron. Soc. **240**, 991 (1989).

[1]The curve in Fig. 5 corresponds to the dependence $\log M_\mathrm{d}/L_B = 1.937(B-V)_0 - 1.019$ (see Table A3 for the closed-box model in the paper by Bell and de Jong (2001)).

34. J. A. Sellwood, R. W. Nelson, and S. Tremaine, Astrophys. J. **506**, 590 (1998).
35. F. Simien and Ph. Prugniel, Astron. Astrophys., Suppl. Ser. **145**, 263 (2000).
36. F. Simien and Ph. Prugniel, Astron. Astrophys. **384**, 371 (2002).
37. R. S. de Simone, Wu Xiaonan, and S. Tremaine, Mon. Not. R. Astron. Soc. (in press); astro-ph/0310906 (2003).
38. N. Ya. Sotnikova and S. A. Rodionov, Pis'ma Astron. Zh. **29**, 367 (2003) [Astron. Lett. **29**, 321 (2003)].
39. L. Spitzer and M. Schwarzschild, Astrophys. J. **114**, 385 (1951).
40. L. Spitzer and M. Schwarzschild, Astrophys. J. **118**, 106 (1953).
41. K. L. Shapiro, J. Gerssen, and R. P. van der Marel, Astron. J. **126**, 2707 (2003).
42. A. V. Zasov, D. V. Bizyaev, D. I. Makarov, and N. V. Tyurina, Pis'ma Astron. Zh. **28**, 599 (2002) [Astron. Lett. **28**, 527 (2002)].

*Translated by A. Dambis*

*Astronomy Letters, Vol. 30, No. 9, 2004, pp. 603–614. Translated from Pis'ma v Astronomicheskiĭ Zhurnal, Vol. 30, No. 9, 2004, pp. 663–675.*


# Natural Spectral Bandwidth of Electron Cyclotron Maser Emission

**G. D. Fleishman***

*Purple Mountain Observatory, Nanjing, 210008 China*
*Ioffe Physicotechnical Institute, Russian Academy of Sciences,*
*ul. Politekhnicheskaya 26, St. Petersburg, 194021 Russia*

Received July 23, 2003

**Abstract**—We studied the spectral properties of the electron cyclotron maser emission generated by anisotropic distributions of fast electrons with power-law magnitude distributions in solar flares. The natural bandwidth of the generated spectral line depends significantly on the angle between the direction of the wave emission and the direction of the magnetic field in the source. In addition, the line bandwidth depends on the parameters of the momentum and pitch-angle distribution functions for fast electrons. The typical spectral bandwidths are shown to lie within the range 0.1–0.4%, in agreement with the minimum observable bandwidths of millisecond solar radio spikes. © *2004 MAIK "Nauka/Interperiodica"*.

Key words: *Sun*.

## INTRODUCTION

In recent years, new pieces of evidence that the solar radio spikes observed during solar flares are generated by the electron cyclotron maser mechanism have been obtained (Fleishman and Mel'nikov 1998; Fleishman *et al.* 2003). It has long been known (Benz 1986; Stähli and Magun 1986; Csillaghy and Benz 1993) that the spectral bandwidth of an individual spike can be very small, $\Delta\omega/\omega \lesssim 1\%$. Recently, Messmer and Benz (2000) showed that the smallest natural FWHM bandwidth of spikes in the two analyzed events was 0.17 and 0.41%, respectively. This imposes fairly stringent constraints on the microscopic mechanism responsible for the generation of radio spikes: it must be capable of producing narrow spectral lines whose theoretical bandwidth does not exceed the observed values.

Clearly, the observed spectral bandwidth of the radio emission line is a superposition of the effects from several factors: the natural bandwidth of the spectral line and its broadening due to the nonlinearity of the emission process, the inhomogeneity of the emission source, and the scattering of the emission on the way between the source and the observer.

Note that the theory for the generation of the electron cyclotron maser emission (ECME) line (and, accordingly, solar radio spikes) is currently very fragmentary and is still far from being compete. Hewitt *et al.* (1982) (see also Messmer and Benz 2000) provided a kinematic estimate of the ECME bandwidth that, however, is virtually independent of the properties of the distribution function for the fast electrons that generate this emission. Platonov and Fleishman (2001) and Fleishman (2004a) studied the modification of the spectral shape of the ECME line under the effect of magnetic-field inhomogeneities in the emission source.

Aschwanden (1990) showed that the ECME line broadens during its quasi-linear saturation. This is because the emission at the frequency at which its growth was initially fastest is the earliest to saturate (i.e., its growth initially slows down and subsequently ceases and gives way to its decay). Therefore, when the growth of the emission slows down (ceases) at the line center and continues in its wings, the spectral line bandwidth increases. Therein lies the mechanism of line broadening due to the nonlinearity. It is easy to understand that the shape of the spectral line can itself be significantly modified by such nonlinear effects.

However, when analyzing their observational data, Csillaghy and Benz (1993) rejected all spikes with complex spectral profiles by assuming that the multicomponent structure of the profile resulted from a *superposition* of various spikes with simple spectral profiles. This selection criterion leads to a selection effect that favors spikes at a linear stage. Consequently, the data accumulated to date on the spectral properties of radio spikes should be interpreted in terms of a linear theory.

Nevertheless, the dependence of the natural ECME bandwidth itself on the distribution parameters of fast particles and on the plasma parameters in the sources of solar radio spikes remains unexplored,

*E-mail:gregory@sun.ioffe.rssi.ru

although the problem of the spectral ECME bandwidth has been considered in detail to explain the fine spectral structure of the auroral kilometric radiation (AKR) (Gurnett and Anderson 1981; Baumback and Calvert 1987; Yoon and Weatherwax 1998; Pritchett *et al.* 1999). Interestingly, the spectral bandwidth of individual AKR peaks is very small, $\Delta\omega/\omega \sim 10^{-3}$ (Gurnett and Anderson 1981), with the lowest values being $\sim 10^{-5}$ (Baumback and Calvert 1987). Yoon and Weatherwax (1998) recently showed that the ECME generated by fast electrons with realistic (based on observations) distribution functions easily provides spectral bandwidths of $\sim 10^{-3}$.

Unfortunately, the numerous results obtained for the AKR conditions cannot be directly extended to the conditions in the solar corona (since the magnetic fields, the plasma densities and temperatures, and the distribution functions of fast electrons differ significantly in these two cases). Therefore, studying the ECME in the solar corona is, to a large extent, a problem in its own right that requires a proper analysis.

In this paper, we consider the dependence of the natural spectral line bandwidth on the above parameters for a power-law magnitude distribution of fast electrons. The pitch-angle distribution of fast electrons was modeled in accordance with our observations (Fleishman *et al.* 2003; Fleishman 2004b) by a loss-cone function; the dependence of the number of particles on the cosine of the pitch angle within the loss cone was assumed to be Gaussian.

## FORMULATION OF THE PROBLEM

### *The ECME Amplification Coefficient*

The electron cyclotron maser emission arises when the gyrosynchrotron absorption coefficient in the region of one or more gyrofrequency harmonics changes its sign, resulting in an amplification of the electromagnetic waves due to the cyclotron instability. The amplification (absorption) coefficient of the cyclotron instability is given by the standard expression (Eidman 1958)

$$\kappa_\sigma(\omega,\vartheta) = -\frac{\pi^2\omega_{pe}^4}{\omega|\eta|v_\sigma N(1+K_\sigma^2+\Gamma_\sigma^2)\left(n_\sigma^2\frac{\partial(\omega n_\sigma)}{\partial\omega}\right)} \times \sum_{n=1}^{\infty}\int\frac{p^2}{\gamma_e\beta}dp(1-\mu^2) \times\left[\frac{-\Gamma_\sigma\sqrt{1-\eta^2}+K_\sigma(\eta-\beta\mu n_\sigma)}{n_\sigma\beta\sqrt{(1-\mu^2)(1-\eta^2)}}J_n(z)+J_n'(z)\right]^2 \times\left[p\frac{\partial}{\partial p}-(\mu-n_\sigma\beta\eta)\frac{\partial}{\partial\mu}\right]f(\mathbf{p})|_{\mu=\mu_*}. \quad (1)$$

Here, $\mu=\cos\theta$ is the cosine of the electron pitch angle,

$$\mu_* = \frac{\gamma_e\omega - n\omega_{Be}}{\gamma_e\beta n_\sigma\eta\omega}, \qquad |\mu_*|\le 1; \quad (2)$$

$\eta=\cos\vartheta$ is the cosine of the emission angle; $v_\sigma$ and $n_\sigma$ are the group velocity and refractive index of the $\sigma$ wave, respectively; $\omega_{pe}$ is the electron plasma frequency; $K_\sigma$ and $\Gamma_\sigma$ are the polarization vector components of the $\sigma$ wave; $\beta=v/c$ is the dimensionless particle velocity; $\gamma_e=(1-\beta^2)^{-1/2}$ is the particle Lorentz factor; $J_n(z)$ and $J_n'(z)$ are the Bessel function and its first derivative with respect to the argument $z$, $z=(\omega/\omega_{Be})\gamma_e n_\sigma\beta\sqrt{(1-\mu^2)(1-\eta^2)}$; and $N$ is the number density of the thermal electrons in the plasma.

The expressions for the refractive indices and the polarization vectors are well known; these are given, for example, in the Appendix to our previous paper (Fleishman 2004b).

### *Definition of the Natural Spectral ECME Bandwidth*

In contrast to atomic spectral lines, ECME lines have no fundamental bandwidth; on the contrary, this bandwidth can strongly depend on the parameters of the problem. In this study, we define the natural ECME bandwidth as the width of the spectral profile for the spatial amplification coefficient (in a given direction) at 0.9 of its maximum. This definition corresponds to the natural ECME bandwidth at $1/e$ of its maximum if the peak of the emission line is observed at the amplification optical depth $\tau=\kappa_{\max}L=10$ in a nonlinear (unsaturated) regime. At the typical parameters for solar flares, the geometric size of an amplification region with $\tau\sim 10$ (in the region of the lowest gyrofrequency harmonics) ranges from several to several hundred kilometers.

Note that the natural spectral ECME bandwidth is defined here in the linear approximation. An allowance for the nonlinearity (the quasi-linear saturation of the instability) can result in a broadening of the spectral ECME line, as can an allowance for the source inhomogeneity and for the emission propagation effects.

### *The Model Distribution Function*

The distribution function for fast electrons was modeled by the product of the angular function and a function that depends only on the momentum magnitude,

$$f(\mathbf{p}) = \frac{N_e}{2\pi}f_1(p)f_2(\mu), \quad (3)$$

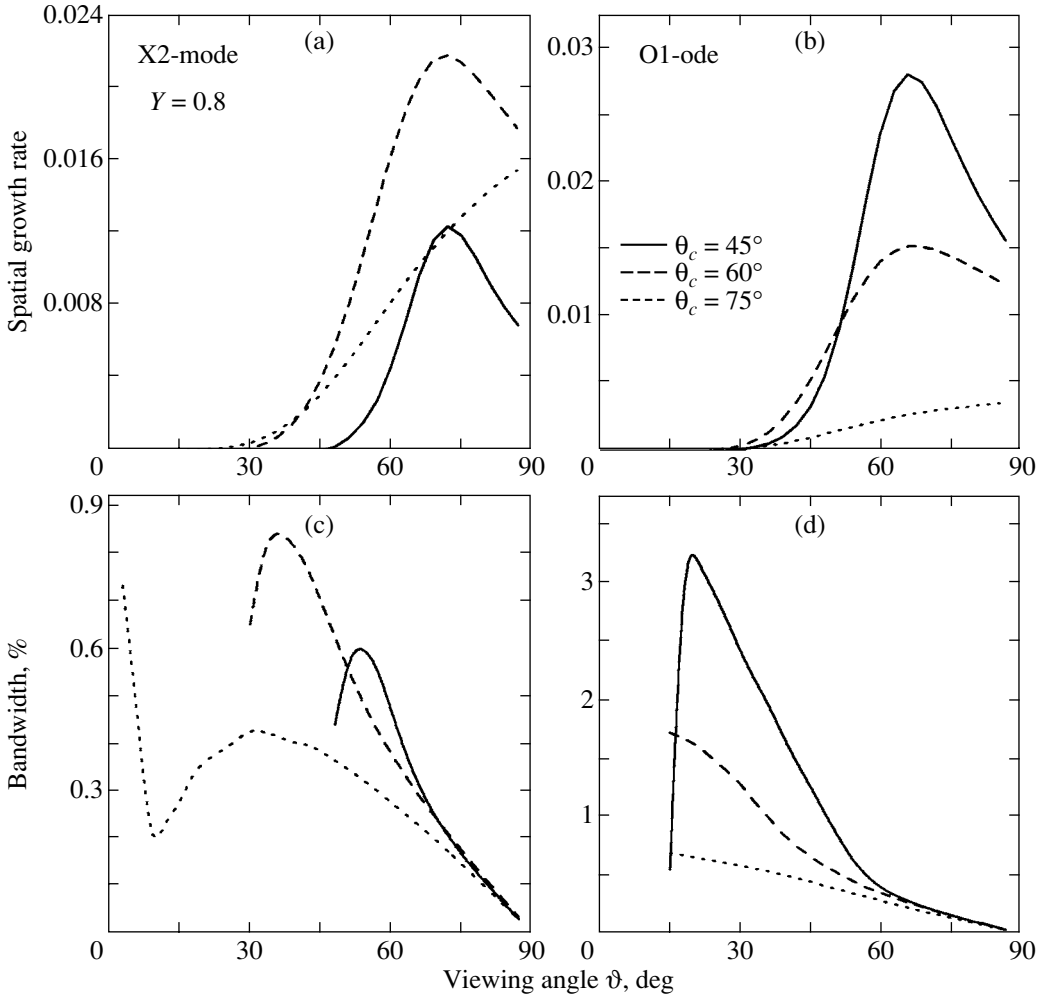


**Fig. 1.** Highest growth rates of the extraordinary waves near the second gyrofrequency harmonic (a) and the ordinary waves near the first harmonic (b) versus viewing angle at $Y = 0.8$; (c), (d) the corresponding spectral bandwidths versus viewing angle.

where $N_e$ is the number density of the fast electrons. Analysis of the observational data on the correlation between the spike emission and the accompanying continuum nonthermal emissions (Fleishman 2004b) allows the form of the model functions $f_1(p)$ and $f_2(\mu)$ to be constrained significantly. In accordance with our previous results (Fleishman 2004b), the dependence on the momentum magnitude is assumed to be described by a power law that changes to an exponential decay at large momenta:

$$f_1(p) \propto \begin{cases} \frac{(\gamma-3)p_0^{\gamma-3}}{p^\gamma}, & p_0 < p < p_{br} \\ \frac{(\gamma-3)p_0^{\gamma-3}}{p_{br}^\gamma} \exp\left(-\gamma\frac{p-p_{br}}{p_{br}}\right), & p > p_{br}. \end{cases} \quad (4)$$

The angular part $f_2$ of the distribution function was modeled by a Gaussian loss cone:

$$f_2(\mu) \propto \begin{cases} \exp\left(-\left(\frac{\mu-\cos\theta_c}{\Delta\mu}\right)^2\right), & \mu > \cos\theta_c \\ 1, & -\cos\theta_c < \mu < \cos\theta_c \\ \exp\left(-\left(\frac{\mu+\cos\theta_c}{\Delta\mu}\right)^2\right), & \mu < -\cos\theta_c, \end{cases} \quad (5)$$

where $\theta_c$ is the loss-cone angle, and $\Delta\mu$ is its width.

First, we chose a set of basic parameters of the distribution function for fast electrons and plasma frequency-to-gyrofrequency ratios. We then analyzed the dependences of the spectral bandwidth by sequentially varying each of these parameters (within the possible range of each of these in solar flares). Accordingly, we chose the following basic parameters of the distribution function: $p_0/mc = 0.2$ ($E_{\rm kin} \approx$

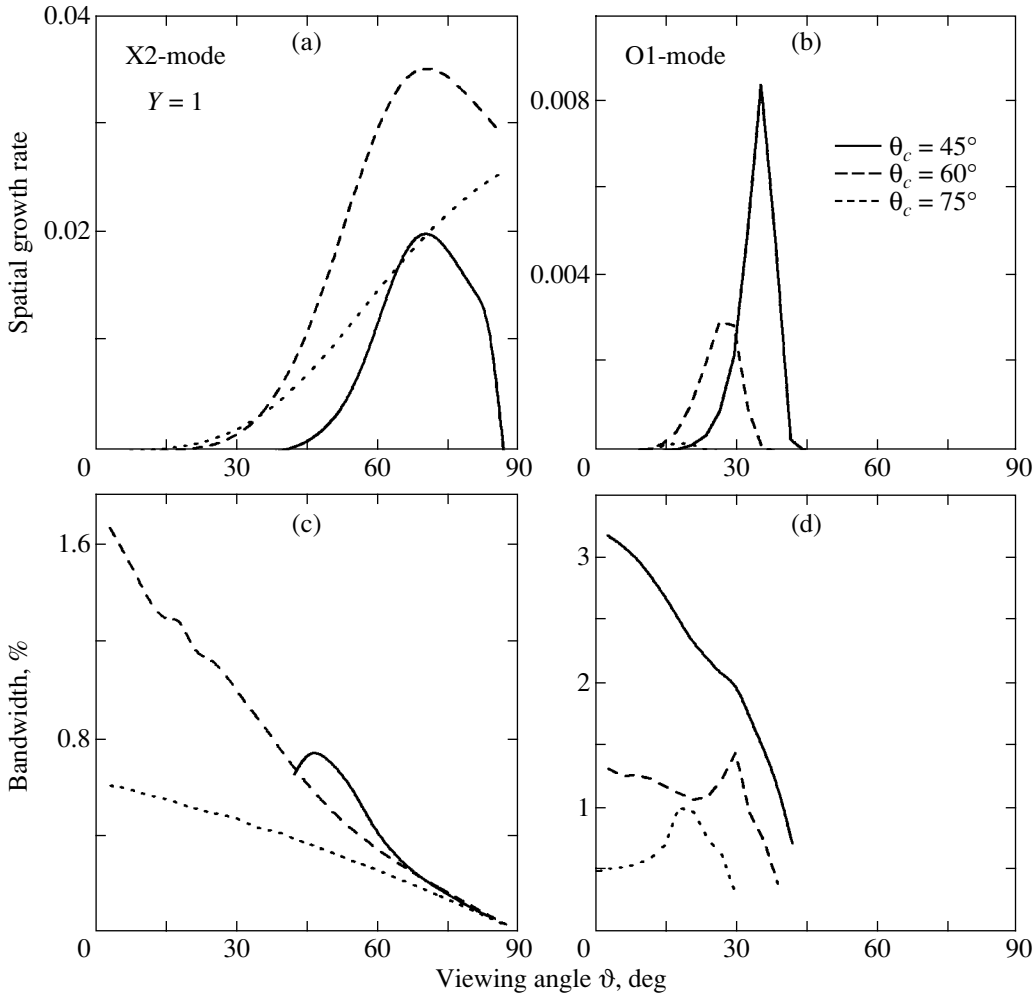


**Fig. 2.** Same as Fig. 1 at $Y = 1$.

10 keV), $p_{\rm br}/mc = 3$ ($E_{\rm kin} \approx 1.1$ MeV), $\gamma = 6$, $\theta_c = 60°$, and $\Delta\mu = 0.1$.

## DEPENDENCE OF THE NATURAL LINE BANDWIDTH ON THE PARAMETERS OF THE PROBLEM

### *Dependence on the Viewing Angle*

An important parameter (whether a given electromagnetic mode can be amplified at all depends on it) is the plasma frequency-to-gyrofrequency ratio:

$$Y = \omega_{\rm pe}/\omega_{Be}. \qquad (6)$$

We used two values of this parameter, $Y = 0.8$ and 1.2. In the former case, the extraordinary and ordinary modes have the highest growth rates near the second gyrofrequency harmonic and the fundamental tone, respectively. In the latter case, both modes reach the highest growth rate near the second gyrofrequency harmonic, with the growth rate of the extraordinary wave being approximately an order of magnitude higher than that of the ordinary wave. As a result, this choice of values allows a pairwise comparison of the spectral properties of the ECME produced by various eigenmodes near the two lowest gyrofrequency harmonics. In all of the cases considered, the shape of the spectral profile for the emission coefficient in the region of the peak is well (with an accuracy of at least 10%) described by a parabolic law, which corresponds to a Gaussian emission line (since $I \propto \exp(\kappa_\sigma(\omega, \vartheta)L)$).

Before we analyze the dependence of the natural ECME bandwidth on the parameters of the problem, let us consider the dependence of the growth rates and the corresponding bandwidths on the angle (with respect to the magnetic field) at which the source is observed. In Figs. 1a and 1b, the highest (as a function of the frequency) spatial growth rates of the extraordinary waves near the second harmonic (below, X2-waves; Figs. 1a, 4c) and the ordinary waves

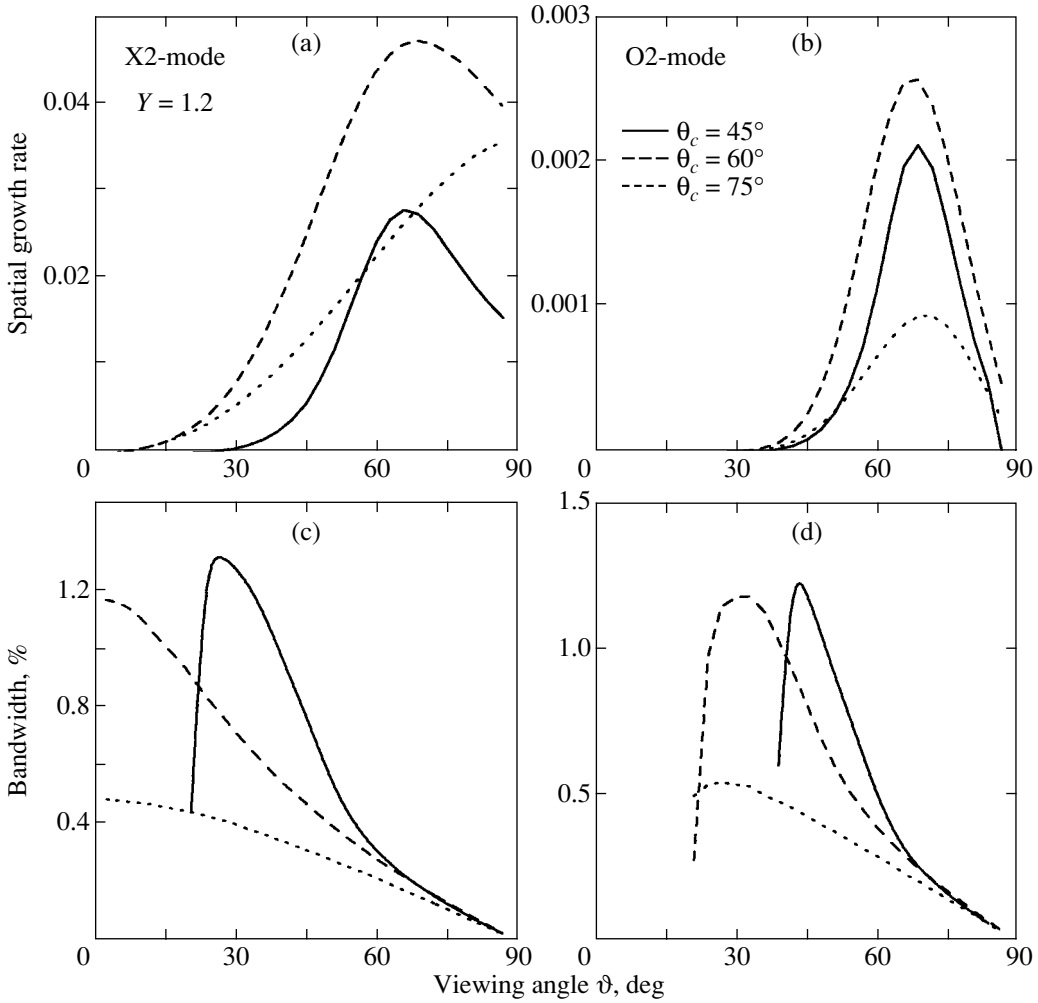


**Fig. 3.** Same as Fig. 1 at $Y = 1.2$; the ordinary mode is near the second harmonic.

near the first harmonic (below, O1-waves, Figs. 1b, 1d) are plotted against the viewing angle at $Y = 0.8$.

Note that both modes are preferentially generated in quasi-transverse (with respect to the magnetic field) directions. The lower panels show the corresponding dependences of the spectral bandwidth $\Delta s(\vartheta) = \Delta\omega(\vartheta)/\omega_{\text{peak}}(\vartheta)$, where $\omega_{\text{peak}}(\vartheta)$ is the frequency at which the wave growth rate in a given direction reaches its maximum (not an absolute maximum), and $\Delta\omega(\vartheta)$ is the full width at 0.9 of the maximum growth rate in this direction. It is easy to see that there is no simple correspondence between the curves in the upper and lower panels: in particular, neither the minimum nor the maximum of the curve that describes the spectral bandwidth corresponds to the peak of the growth rate.

The peak of the O1-mode growth rate shifts toward quasi-longitudinal directions as $Y$ increases ($Y = 1$, Fig. 2), because the emission in quasi-transverse directions becomes kinematically impossible. Accordingly, the absolute value of the growth rate begins to decrease (and the O1-wave instability disappears as $Y$ increases further). In this case, the spectral lines in the region of the largest amplification prove to be much broader than those at low values of $Y$ (Fig. 1).

The dependence of the spectral bandwidths for the X2-waves on the angle near the peak of the growth-rate curve changed only slightly compared to that in Fig. 1, although the differences are quite marked at small angles (at which the growth rate is low).

At $Y = 1.2$ (Fig. 3), the X2- and O2-waves are unstable. Note that the dependence of the growth rates for the O2-waves on the angle is much narrower than that for the X2-waves. This implies that the possible scatter of spectral widths attributable in observations to the variations of the viewing angle within the region where the wave amplification is significant is larger for the X2-waves than for the O2-waves. The spectral bandwidth proves to be less than 1% in

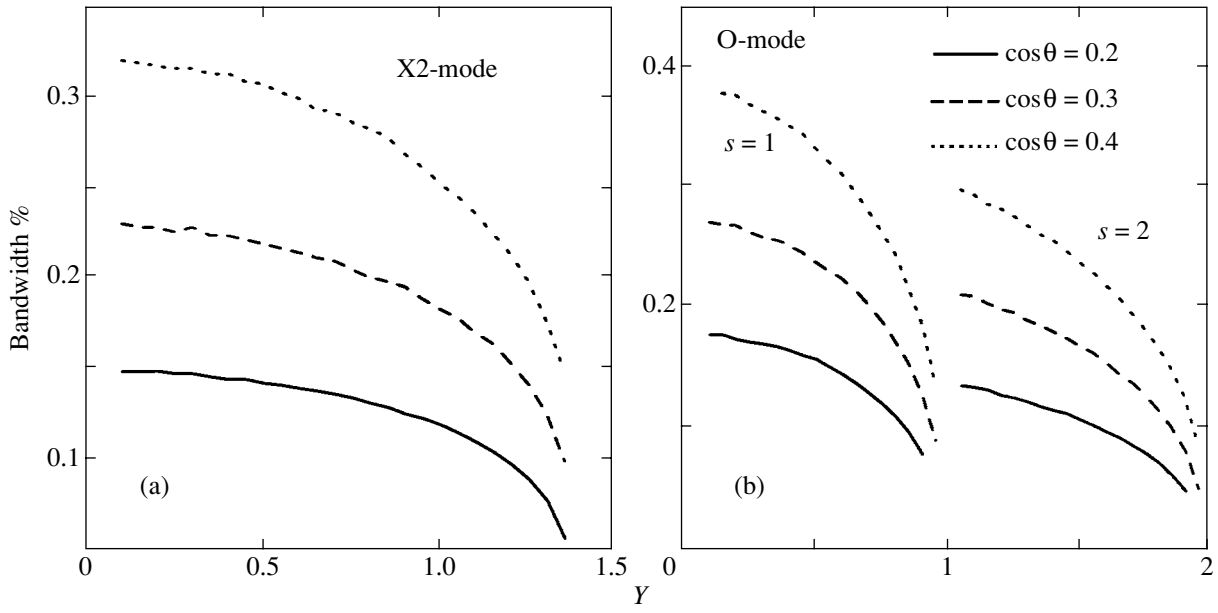


**Fig. 4.** Natural spectral bandwidth of the ECME generated at three different angles (shown in the figure) versus $Y$ for the extraordinary mode at the second harmonic (a) and the ordinary mode at the first and second harmonics (b) for a set of basic parameters.

the entire region of angles where the amplification is significant.

In accordance with the results presented in Figs. 1–3, we will analyze the growth rates for three fixed viewing angles, $\eta = \cos\vartheta = 0.2$, 0.3, 0.4. We emphasize that, in general, the viewing angle at which the growth rate reaches an absolute maximum does not closely coincide with any of the chosen viewing angles. Nevertheless, since all three values of $\eta$ are in the region of the peak, an analysis of the three corresponding curves suggests that there is a scatter of spectral bandwidths under actual conditions.

### *Dependence on the Plasma Density*

Let us consider the dependence of the spectral bandwidths on the plasma parameter $Y$ in the range of its variations from 0.1 to 2 (Fig. 4). For the X2-mode, this dependence is very weak: when $Y$ increases by a factor of 14, $\Delta s$ decreases by no more than a factor of 2. The dependence on $Y$ for the O1-mode is more pronounced: $\Delta s$ decreases by more than a factor of 2 when $Y$ increases by a factor of 8–10, and is even stronger for the O2-mode: a two-fold increase in $Y$ leads to a two-to-three-fold decrease in the spectral bandwidth. Note that all modes exhibit a narrowing of the spectral profiles of the lines *emitted in a fixed direction* as $Y$ increases.

### *Dependence on the Momentum-Magnitude Distribution*

The model function $f_1$ (4) depends on three parameters: the spectral index $\gamma$, the minimum momentum $p_0$, and the break momentum $p_{\rm br}$. The dependence of $\Delta s$ on $p_{\rm br}$ is very weak (Fig. 5), because the most numerous low-energy electrons make a dominant contribution to the line formation.

The dependence on the initial momentum $p_0$ (Fig. 6) is more pronounced. As $p_0$ increases, the bandwidth initially increases almost linearly (rather than quadratically, as is commonly assumed on the basis of the simplified estimates presented by Hewitt *et al.* (1982)) and subsequently decreases. This decrease occurs when the instability operates slightly above the threshold (so the entire range of frequencies and angles where the instability is possible gradually narrows). As $p_0$ increases further (at constant $\Delta\mu$), the instability disappears, so it makes no sense to talk about the natural line bandwidth. In the range of variations under consideration, the spectral bandwidths are still appreciably smaller than 1%.

The dependences on the electron spectral index $\gamma$ are shown in Fig. 7. It is easy to see that the bandwidths of the O1- and O2-waves are more sensitive to variations in the spectral index than those of the X2-waves. Nevertheless, the $\Delta s$ range is small, ~50% for each of the curves.

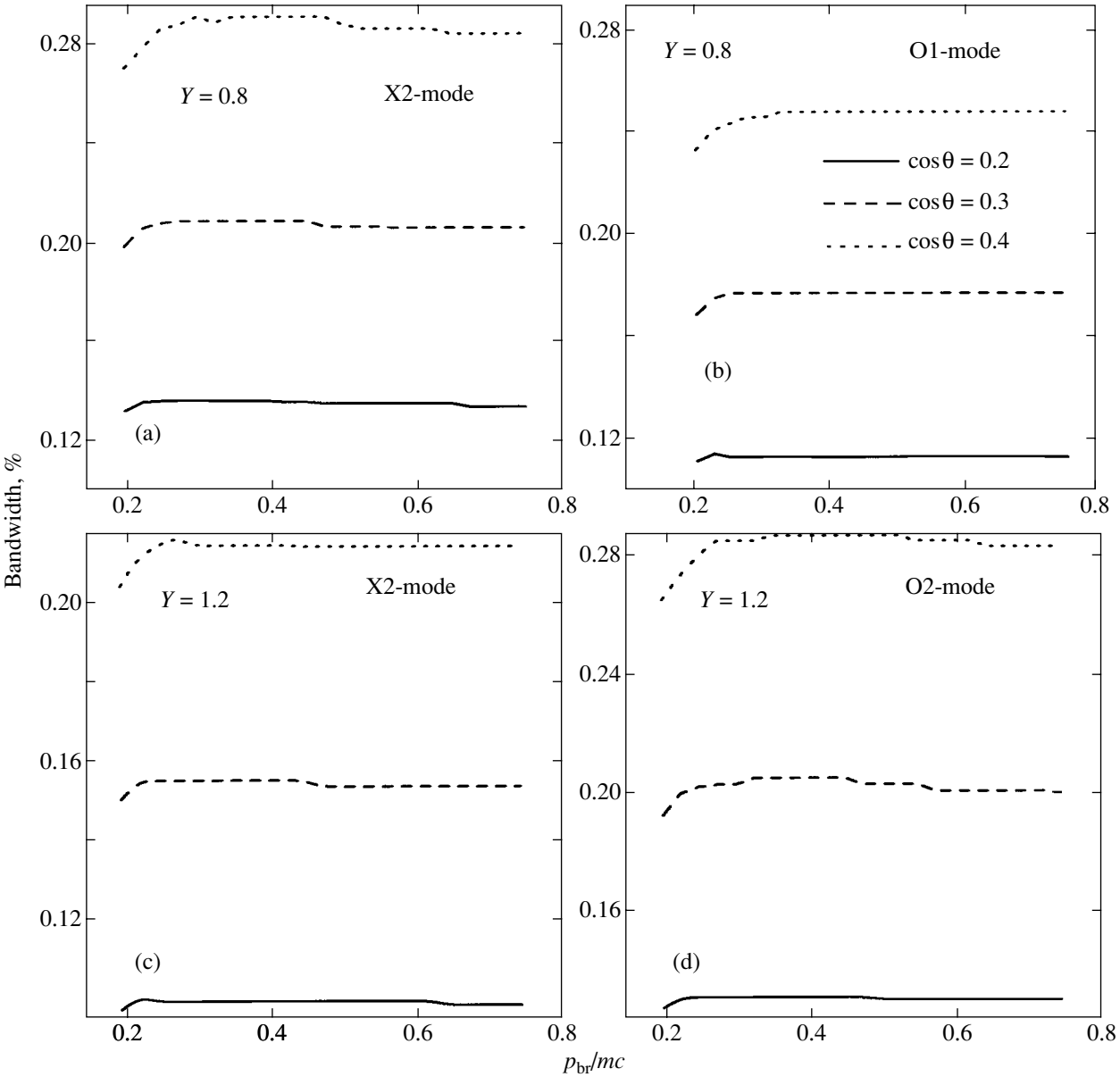


**Fig. 5.** Natural spectral bandwidth of the ECME generated at three different angles (shown in the figure) versus $p_{br}$ for the extraordinary mode at the second harmonic (a), (c) and the ordinary mode at the first (b) and second (d) harmonics for a set of basic parameters.

*Dependence on the Angular Distribution*

Figure 8 illustrates the influence of the loss-cone angle $\theta_c$ on the spectral bandwidth. The corresponding bell-shaped curves reach a maximum in the range of angles $\theta_c = 45°–60°$, while the spectral bandwidth can decrease by a factor of 2 or 3 when $\theta_c$ decreases or increases.

Of great interest is the dependence of the bandwidth on $\Delta\mu$, i.e., on the angular gradient of the distribution function within the loss cone (Fig. 9). For large gradients (small $\Delta\mu$), very narrow ECME lines with $\Delta s \lesssim 0.1\%$ are generated; however, as $\Delta\mu$ increases, the bandwidths increase, reaching $\sim 0.3–0.4\%$ at $\Delta\mu = 0.1–0.2$. Subsequently, the bandwidths again begin to decrease sharply. This decrease occurs when the instability approaches close enough to its threshold and disappears as $\Delta\mu$ increases further (in this case, the electron distribution is still highly anisotropic).

## DISCUSSION

The main results of our study of the "natural" spectral ECME line are as follows.

(1) The line profile is Gaussian.

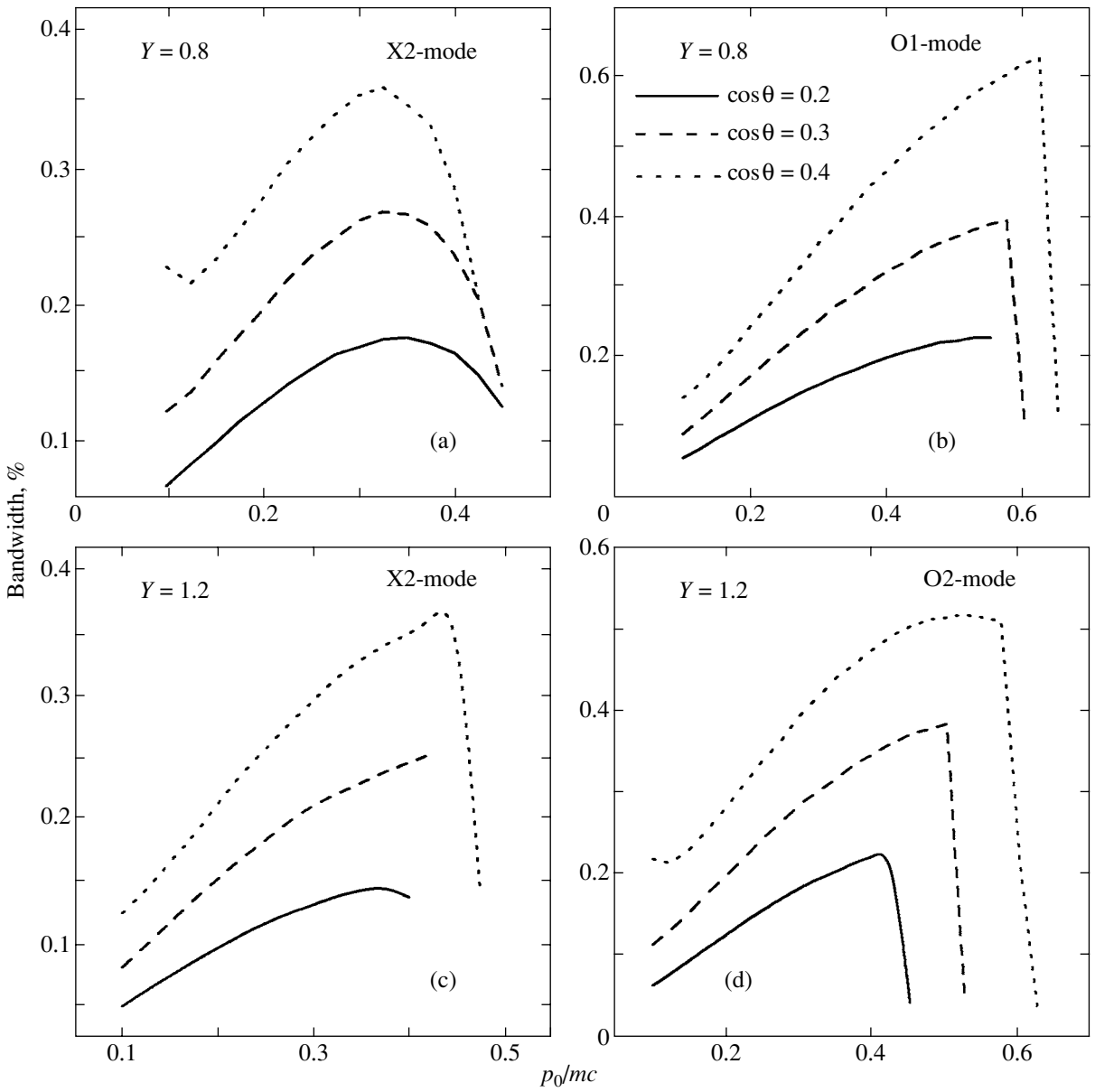


**Fig. 6.** Same as Fig. 5 for the parameter $p_0$.

(2) The line bandwidth depends significantly on the viewing angle with respect to the magnetic-field direction and on the distribution parameters of the fast electrons.

(3) The typical spectral bandwidths lie within the range 0.1–0.4%.

(4) The commonly used bandwidth estimate $\Delta\omega/\omega \sim v^2/c^2$ (Hewitt *et al.* 1982) is improper, since it not only overestimates the line bandwidth by more than an order of magnitude, but also yields an incorrect functional dependence of the bandwidth on the characteristic velocity of the emitting electrons.

Let us discuss the question of whether our results agree with the observational data on millisecond radio spikes and the extent to which a quantitative application of our results to observations is acceptable.

Indeed, we analyzed only the natural spectral ECME bandwidth in the linear approximation, while the possible line broadening due to the nonlinearity of the wave amplification process, the source inhomogeneity, and the propagation effects on the way from the source to the observer was not considered.

Qualitatively, the role of the nonlinearity is that the emission is saturated first at the center of the spectral profile and only later in the line wings. Quasi-linear saturation is known (Fleishman and Arzner 2000) to cause the growth of the emission to slow down; as a result, the pulse time profile contains a Gaus-

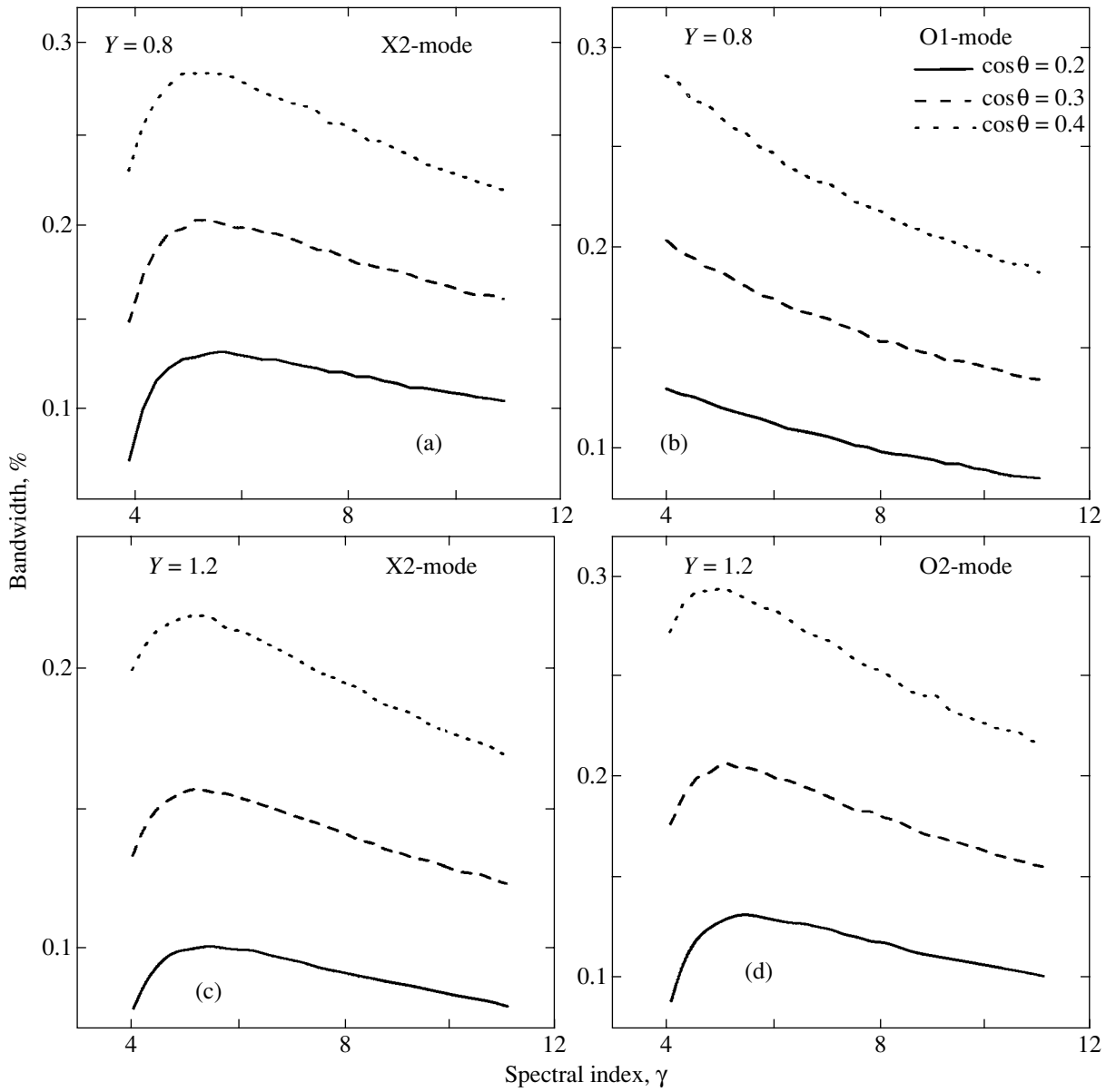


**Fig. 7.** Same as Fig. 5 for the parameter $\gamma$.

sian rather than exponential growth phase. Since solar radio spikes with a Gaussian growth phase are commonly observed (Güdel and Benz 1990; Fleishman and Mel'nikov 1998), quasi-linear effects actually play an important role in the generation of spike emission. Recently, however, Mészárosová *et al.* (2003) have also detected radio spikes with an exponential growth phase in which the nonlinear saturation effects are probably not so significant. In addition, as was discussed above, when analyzing observational data, preference is implicitly given to the spikes generated in the linear regime due to the selection criteria adopted by Csillaghy and Benz (1993). This implies that all of the spectral properties of radio spikes deduced from observations must be explained in terms of linear theory (in general, with allowance made for the inhomogeneity of the emission source).

Let us first discuss what could be responsible for the scatter of spectral bandwidths in an individual event. If we are dealing with an individual event, then we must primarily limit the $Y$ range. However, this is not very important in the problem of the spectral bandwidths, because their dependence on $Y$ is fairly weak.

Another important parameter is the viewing angle. The qualitatively correct pattern of spike clustering in some region of a magnetic trap (in this case, each spike is formed in its own local source within

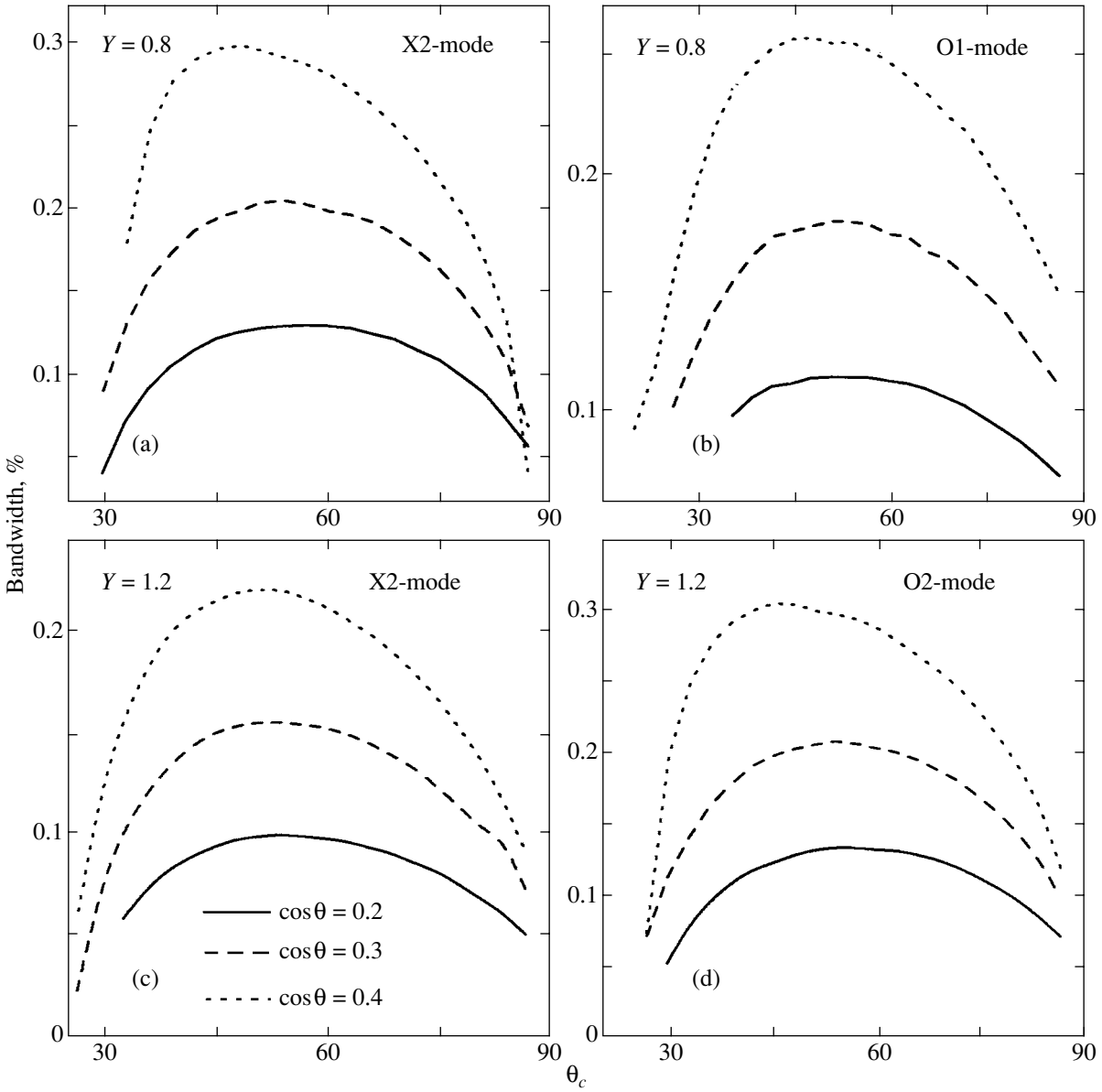


**Fig. 8.** Same as Fig. 5 for the parameter $\theta_c$.

this trap) probably corresponds to a characteristic viewing angle and a small scatter of viewing angles about this characteristic value. Since the dependence of the spectral bandwidth on the viewing angle is pronounced (Figs. 1–3), even small variations (say, within 10°–15°) can provide a significant scatter of bandwidths (by a factor of 2–4). Given the possible evolution of the distribution function for fast electrons (the changes in $\Delta\mu$, $p_0$, $\theta_c$, $\gamma$) and the variations in the optical depth from one local source to another, the expected scatter of natural spectral bandwidths in an individual event can be estimated as

$$\frac{\Delta s_{\max}}{\Delta s_{\min}} \sim 2\text{–}6. \qquad (7)$$

In general, the scatter of the observed bandwidth could be even larger if the contribution of the nonlinearity, the inhomogeneity, and the scattering is taken into account. These factors will cause the scatter to increase, but only if these affect narrow and broad spikes differently. If, however, this influence is more or less the same, then the scatter will not increase, but both the individual observed bandwidths and their mean in a given event will increase.

It is well known from observations (Csillaghy and Benz 1993) that the scatter of bandwidths in an individual event can be very large, ~3–8. We emphasize that this scatter (except for the extreme values) is inherent in the microscopic process of electron cyclotron maser emission itself (although this,

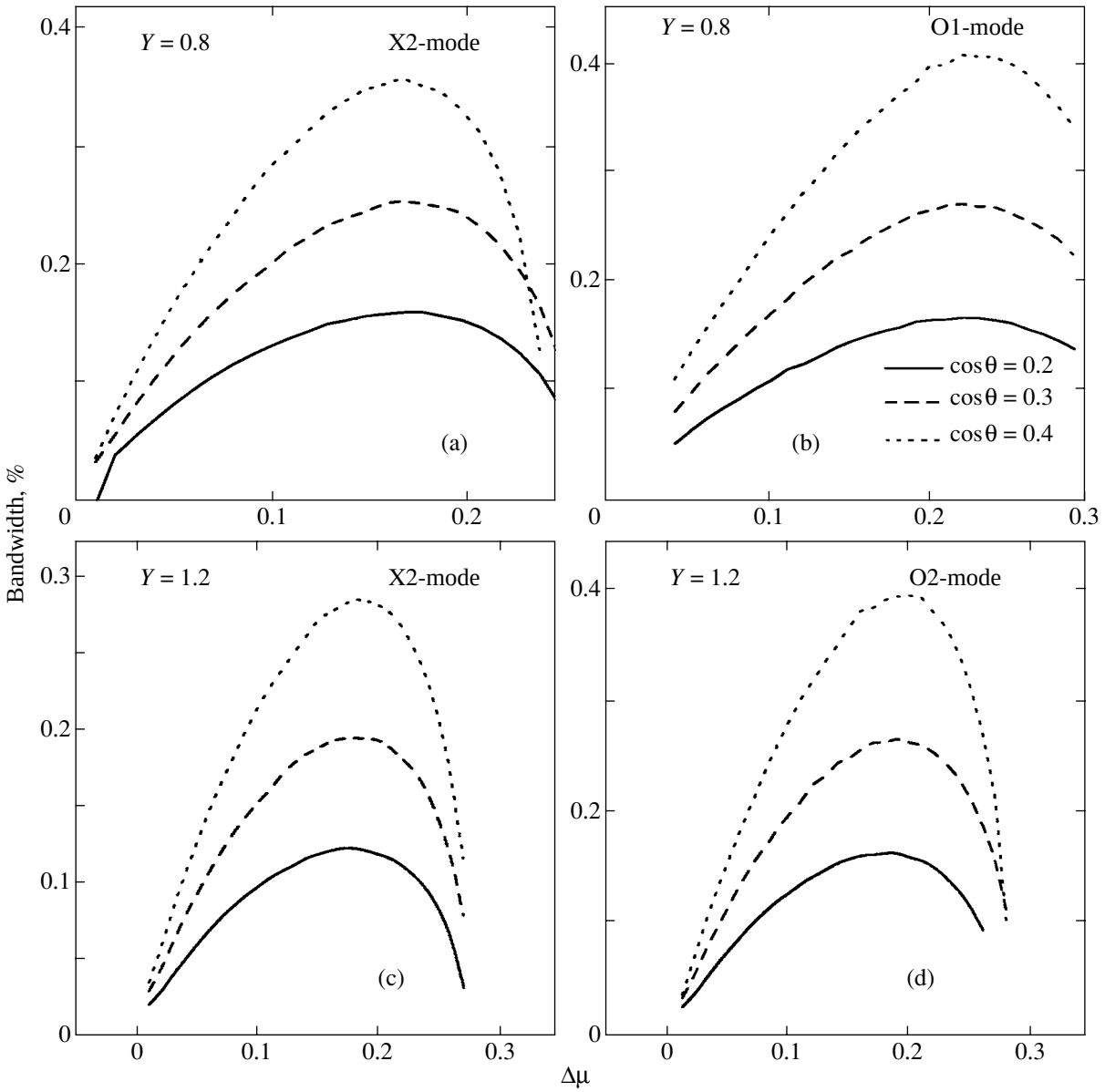


**Fig. 9.** Same as Fig. 5 for the parameter $\Delta\mu$.

of course, does not imply that nonlinearity, inhomogeneity, and scattering do not make a tangible contribution to the broadening). Moreover, the smallest FWHM bandwidths of radio spikes determined for two spike events were 0.17 and 0.41% (Messmer and Benz 2000), in good quantitative agreement with our results. Therefore, it is highly likely that the observed bandwidth of radio spikes in certain cases is determined mainly by the natural bandwidth of the ECME line, while the processes of its broadening are not so important.

Of no less importance is the question of what is responsible for the scatter of mean bandwidths at the same frequency from event to event. If we keep in mind only the natural line bandwidth, then this scatter could result from the change in the viewing angle from one event to another and from the difference between the distribution functions for fast electrons in different events (while, say, the dependence on $Y$ is too weak to account for the observed scatter of values).

In many cases, however, spikes with spectral bandwidths larger than 1% are recorded; this is very difficult to reconcile with our characteristic values of 0.1–0.4%, so an additional line broadening mechanism is required. In the linear theory, random (magnetic field and/or plasma density) inhomogeneities in the emission source can provide this broadening. This mechanism is efficient enough (Fleishman 2004a) to

account for the entire range of observed spike spectral bandwidths. It is very important that the corresponding renormalized theory of line generation in a source with random inhomogeneities (Fleishman 2004a) yields a Gaussian line profile, in agreement with the observations by Csillaghy and Benz (1993).

In general, nonlinearity effects could also lead (and actually lead) to line broadening. In this case, however, the line shape would differ markedly from a Gaussian and would be rejected when processing the observational data according to the selection criteria by Csillaghy and Benz (1993).

Obviously, observations with a high angular resolution could clarify significantly the situation with the separation of the viewing-angle effect from other effects, while the role of propagation effects can be revealed by a simultaneous analysis of the spectral and polarization properties of radio spikes.

Nevertheless, we can state already now that there is satisfactory quantitative agreement between the ECME line generation theory and the observational data on the spectral properties of millisecond radio spikes.

## ACKNOWLEDGMENTS

This work was supported in part by the Russian Foundation for Basic Research (project nos. 02-02-39005 and 03-02-17218), the Chinese NFS (no. 10273025), and the "973" program (no. G2000078403).

## REFERENCES

1. M. J. Aschwanden, Astron. Astrophys., Suppl. Ser. **85**, 1141 (1990).
2. M. M. Baumback and W. Calvert, Geophys. Res. Lett. **14**, 119 (1987).
3. A. O. Benz, Sol. Phys. **104**, 99 (1986).
4. A. Csillaghy and A.O. Benz, Astron. Astrophys. **274**, 487 (1993).
5. V. Ya. Eidman, Zh. Éksp. Teor. Fiz. **34**, 31 (1958) [Sov. Phys. JETP **7**, 22 (1958)].
6. G. D. Fleishman, Astrophys. J. **601**, 559 (2004a).
7. G. D. Fleishman, Astrophys. J. (2004b, in press).
8. G. D. Fleishman and K. Arzner, Astron. Astrophys. **358**, 776 (2000).
9. G. D. Fleishman, D. E. Gary, and G. M. Nita, Astrophys. J. **593**, 571 (2003).
10. G. D. Fleishman and V. F. Mel'nikov, Usp. Fiz. Nauk **168**, 1265 (1998) [Phys. Usp. **41**, 1157 (1998)].
11. D. A. Gurnett and R. R. Anderson, *Physics of Auroral Arc Formation*, Ed. by S.-I. Akasofu and J. D. Kan, Geophys. Monogr. Ser., Vol. 25 (AGU, Washington, D.C., 1981), p. 341.
12. M. Güdel and A. O. Benz, Astron. Astrophys. **231**, 202 (1990).
13. R. G. Hewitt, D. B. Melrose, and K. G. Rönnmark, Aust. J. Phys. **35**, 447 (1982).
14. H. Mészárosová, A. Veronig, P. Zlobec, and M. Karlický, Astron. Astrophys. **407**, 1115 (2003).
15. P. Messmer and A. O. Benz, Astron. Astrophys. **354**, 287 (2000).
16. K. Yu. Platonov and G. D. Fleishman, Astron. Zh. **78**, 238 (2001) [Astron. Rep. **45**, 203 (2001)].
17. P. L. Pritchett, R. J. Strangeway, C. W. Carlson, *et al.*, J. Geophys. Res. **104**, 10 317 (1999).
18. M. Stähli and A. Magun, Sol. Phys. **104**, 117 (1986).
19. P. H. Yoon and A. T. Weatherwax, Geophys. Res. Lett. **25**, 4461 (1998).

*Translated by V. Astakhov*

*Astronomy Letters, Vol. 30, No. 9, 2004, pp. 615–629. Translated from Pis'ma v Astronomicheskiĭ Zhurnal, Vol. 30, No. 9, 2004, pp. 676–691.*


# Disk Precession and Quasi-Periodic Brightness Oscillations of V603 Aql in 2001–2002

**V. Suleimanov[1]*, I. Bikmaev[1], K. Belyakov[1], N. Sakhibullin[1], G. Zhukov[1], Z. Aslan[2], U. Kiziloglu[3], and I. Khamitov[2]**

[1] *Kazan State University, Kremlevskaya ul. 18, Kazan, 420008 Russia*

[2] *TUBITAK National Observatory, Antalia, Turkey*

[3] *METU, Ankara, Turkey*

Received November 5, 2003

**Abstract**—We present the photometric observations of the old nova V603 Aql with the RTT 150 Russian–Turkish telescope during eleven nights of 2001–2002. We show that the star at this time was in a state with positive superhumps and its photometric period of $0^d.144$–$0^d.145$ was longer than the orbital period. We found night-to-night variations in the mean brightness of the system that are consistent with disk precession periods of $3^d.3$ and $3^d.0$ in 2001 and 2002, respectively. Analysis of the results and their comparison with the results of other authors using current theoretical models for disk precession lead us to suggest that the change in the disk precession period was caused by a change in the accretion rate in the system. V603 Aql in a state with negative superhumps was found to be brighter than it is in a state with positive superhumps by $0^m.2$–$0^m.3$. We hypothesize that the transition between these states could also be caused by a change in the accretion rate. Quasi-periodic oscillations (QPOs) of the brightness with typical time scales of 9–70 min were detected on each observing night. These time scales were found to change from night to night. The detection of QPOs with a period of about 0.05 of the orbital period and its multiples on certain nights provides evidence for the model of QPO generation through accretion-rate modulation by ionization-front oscillations on the surface of the donor star near the inner Lagrangian point.


Key words: *cataclysmic variables, photometry.*

## INTRODUCTION

One of the brightest (at maximum, its brightness reached $-1^m$) historical novae flared up in 1918 in Aquila and was designated as V603 Aql. Information about the behavior of the star during and immediately after its outburst can be found in the review by Payne-Gaposchkin (1957). At present, the brightness of the star varies within $0^m.2$–$0^m.3$ near its mean level of $11^m.8$ in the $V$ band.

Like all novae, V603 Aql is a close binary system (Warner 1995) that consists of a white dwarf and a Roche-lobe-overfilling red dwarf. The matter transferred to the white dwarf forms an accretion disk around it. The bulk of the optical emission from the binary is produced by the accretion disk, and all brightness oscillations are probably attributable to the processes that take place in this disk.

The orbital period of the binary, $0^d.1385 \pm 0^d.0005$, that was first determined by Kraft (1964) and subsequently improved by Arenas (2000) is not equal to its photometric period, $0^d.1449$, which was found by Haefner and Metz (1985). Further studies showed that the photometric period could vary on a time scale of several months over the range $0^d.1449$–$0^d.1466$ (Patterson *et al.* 1993).

Close binary systems (CBSs) whose photometric periods are several percent longer than their orbital periods are well known and constitute a subclass of SU Ursae Majoris dwarf novae (Warner 1995). During outbursts brighter than ordinary outbursts (superoutbursts), these binaries exhibit brightness oscillations with periods longer than their orbital periods by 1–7%; these are called superhumps. The prograde precession of an eccentric accretion disk with a period of several days (Vogt 1982) is currently believed to be responsible for these brightness variations, and the observed superhump period is the beat period between the orbital and precession periods. Circular accretion disks become eccentric and precessing due to the 3 : 1 resonance when the secondary component tidally influences the outer accretion disk (the orbital period is triple the Keplerian period for the outer

*E-mail: vals@ksu.ru

disk) (Whitehurst 1988; Osaki 1985, 1989; Whitehurst and King 1991; Lubow 1991). This resonance is possible in binaries with component mass ratios $q = M_{rd}/M_{wd} < 0.3$. V603 Aql and other binaries with high accretion rates whose photometric periods exceeded their orbital periods (e.g., V795 Her (Patterson and Skillman 1994) and several others (Patterson *et al.* 1993)) have come to be regarded as binaries with permanent superhumps. Having obtained a component mass ratio of $q = 0.24 \pm 0.05$ for V603 Aql, Arenas *et al.* (2000) corroborated this hypothesis. Note that previous determinations yielded higher values, $q \sim 0.4$ (Ritter and Kolb 1998).

Cataclysmic variables whose photometric periods are several percent shorter than their orbital periods are also observed among the binaries with high accretion rates: TT Ari (Udalski 1988), TV Col (Barrett *et al.* 1988), and CN Ori (Schoembs 1982). The brightness variations in these binaries are attributed to the retrograde precession of the line of nodes of accretion disks tilted with respect to the orbital plane (Patterson *et al.* 1997 (P97)). Accordingly, the observed photometric period is the beat period between the orbital and precession periods. It is not yet completely clear why the disk tilt with respect to the orbital plane appears, but it is obvious that the line of nodes of a tilted disk also precesses due to the tidal influence from the secondary component.

Further studies showed that a particular star did not absolutely belong to the class of stars with positive (the prograde apsidal precession of an eccentric disk) or negative (the retrograde nodal precession of a tilted disk) superhumps. Thus, for example, during the 1992–1994 seasons, V603 Aql exhibited a photometric period shorter than its orbital period ($0^d.1338$–$0^d.1345$, P97), while the brightness of TT Ari in 1997 varied with a period that was 8.5% longer than its orbital period (Skillman *et al.* 1998). Moreover, a detailed analysis of the power spectrum for the light curves of V603 Aql revealed (P97) signals from both positive and negative superhumps. The variations of these periods are correlated, so the relative change in the period of positive superhumps is twice that of negative superhumps. In this case, the longer the period of positive superhumps, the shorter the period of negative superhumps, and vice versa (P97).

This relationship, which was found by Patterson *et al.* (1997), indicates that the nodal precession period is approximately twice the apsidal precession period, which is in agreement with the ratio of these precession periods for the orbit of the Moon (18.6 and 8.85 yr, respectively). This suggests that the observed disk precession appears to be actually produced by tidal effects. Having analyzed the power spectrum for the flux variations of V603 Aql in spectral lines in 1990, Arenas *et al.* (2000) also found two independent periods, $0^d.146$ and $0^d.132$, which, however, do not agree with the relationship found by Patterson *et al.* (1997).

Such complex photometric behavior of this class of cataclysmic variables is suggestive of the complexity of the hydrodynamic processes in the accretion disks of these binaries. The study of these processes requires a long series of observations with the aim of analyzing the variations in the accretion-disk precession periods over time and a search for correlations of these variations with other parameters of the binary, for example, its brightness. This is one of the goals of our paper.

The quasi-periodic brightness oscillations of V603 Aql found by Haefner and Metz (1985) on time scales from 15 to 62 min (see also Udalski and Schwarzenberg-Czerny 1989) are the second problem touched on in this paper. Schwarzenberg-Czerny *et al.* (1992) also detected X-ray flux oscillations with a period of 62.9 min. All of these facts suggested that V603 Aql could be an intermediate polar, i.e., a system in which the inner accretion disk is destroyed by the magnetic field of the white dwarf and the matter near it is accreted onto the magnetic poles (Haefner and Metz 1985; Udalski and Schwarzenberg-Czerny 1989; Gnedin *et al.* 1990; Schwarzenberg-Czerny *et al.* 1992). The detected period of 62.9 min must then be the spin period of the white dwarf. However, further studies showed that this period is not stable and does not always manifest itself (Patterson *et al.* 1993, 1997; Suleimanov *et al.* 1998). It more likely resembles the quasi-periodic oscillations (QPOs) of the brightness typical of other cataclysmic variables with superhumps, for example, TT Ari (Semeniuk *et al.* 1987) and MV Lyr (Borisov 1992; Andronov and Shugarov 1982). It is not yet completely clear why these brightness variations appear, and long series of homogeneous observations are required to reveal their correlations with other binary parameters and to test the available theoretical models.

## OBSERVATIONS

The photometric observations of V603 Aql were performed in the summer of 2001 and 2002 with the 1.5-m RTT 150 Kazan University telescope installed at Mount Bakyrlytepe (Turkey). This star was observed with an ST-8E CCD array in the instrumental $v$ band. A log of observations is given in Table 1. The duration of each observation was 10 s. The photometry was performed by a differential method. The comparison stars used are shown on the finding chart (Fig. 1). According to the SIMBAD database, star 1 has the coordinates $\alpha_{2000} = 18^h49^m2^s$ and

**Table 1.** Log of observations

| Date | Telescope | Beginning–end JD 2400000.0+ | Duration, h | Number of points | $\langle V \rangle$ |
|---|---|---|---|---|---|
| Oct. 7, 1994 | Zeiss 600 | 49633.1771–0.2929 | 2.78 | 570 | $11\overset{m}{.}76$ |
| Oct. 8, 1994 | – | 49634.1759–0.2976 | 2.92 | 609 | 11.76 |
| Oct. 9, 1994 | – | 49635.1984–0.3111 | 2.71 | 579 | 11.62 |
| June 14, 2001 | RTT150 | 52075.3973–0.5730 | 4.22 | 429 | 12.10 |
| June 15, 2001 | – | 52076.5376–0.6767 | 3.34 | 399 | 11.90 |
| June 17, 2001 | – | 52078.5136–0.6701 | 3.76 | 440 | 12.15 |
| June 18, 2001 | – | 52079.5337–0.6905 | 3.76 | 441 | 11.99 |
| Aug. 23, 2001 | – | 52145.3047–0.3801 | 1.81 | 228 | 12.07 |
| Aug. 24, 2001 | – | 52146.3217–0.4440 | 2.94 | 372 | 12.02 |
| July 3, 2002 | – | 52459.3644–0.5129 | 3.56 | 378 | 11.99 |
| July 14, 2002 | – | 52470.3715–0.5679 | 4.71 | 562 | 11.97 |
| July 16, 2002 | – | 52472.3196–0.4446 | 3.00 | 496 | 11.77 |
| July 17, 2002 | – | 52473.3785–0.5607 | 4.37 | 777 | 11.85 |
| July 20, 2002 | – | 52476.4355–0.5572 | 2.92 | 523 | 12.12 |

$\delta_{2000} = 00°33'47\overset{''}{.}57$, the magnitude $V = 13\overset{m}{.}6$, and the color index $B - V = 1.0$. Star 2 has $\alpha_{2000} = 18^h48^m46^s$ and $\delta_{2000} = 00°35'51''$, $V = 14\overset{m}{.}18$, and $B - V = 2\overset{m}{.}34$. The primary reduction was made by the standard method in the MIDAS package. We subtracted the dark and bias frames from each frame and then divided it by a flat field. In each reduced frame, we performed aperture photometry of the variable star and one of the comparison stars. The result was their magnitude difference in the instrumental $v$ band. The light curves obtained are shown in Figs. 2 and 3. Note that star 2 was used as a comparison star only when reducing the observations of August 23, 2001.

In addition, we used the observations of V603 Aql performed in 1994 with a four-channel $WBVR$ photometer attached to the Zeis-600 Special Astrophysical Observatory telescope for a comparative analysis of the results. The $v$-band light curves (Fig. 4) were used. The comparison star was HD 176 808 with the coordinates $\alpha_{2000} = 19^h02^m01\overset{s}{.}3$ and $\delta_{2000} = 00°41'50''$, the magnitude $V = 9\overset{m}{.}12$, and the color index $B - V = 0\overset{m}{.}32$. Details on the observing and reduction conditions can be found in our previous paper Suleimanov *et al.* (1998) and in Table 1.

## RESULTS OF THE SEARCH FOR PERIODICITIES

We searched for periods and quasi-periods in the light curves of V603 Aql using the L2 and WINEFK computer programs that were kindly made available to us by Yu. Kolpakov (Institute of Astronomy, Russian Academy of Sciences) and V. Goranskii (Sternberg Astronomical Institute), respectively.

**Table 2.** Found photometric periods of V603 Aql close to its orbital period. $P_1$ is the fundamental period, $P_2$ are the probable additional periods

| Epoch | Number of nights | $P_1$ | $P_2$ |
|---|---|---|---|
| Oct. 1994 | 3 | $0\overset{d}{.}135$ | $0\overset{d}{.}13$ |
| | | | 0.139 |
| July 2001 | 4 | 0.1442 | 0.1360 |
| | | | 0.13(?) |
| Aug. 2001 | 2 | 0.145 | |
| July 2002 | 5 | 0.1449 | 0.13 |
| | | | 0.139 |

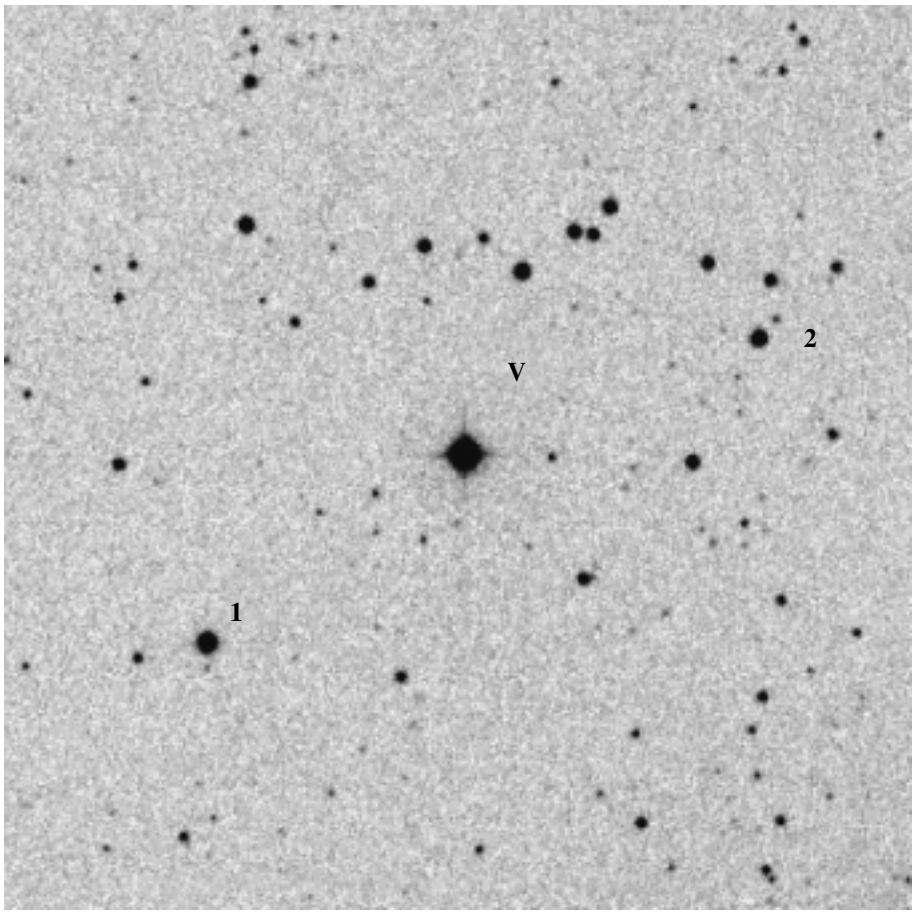


**Fig. 1.** Finding chart and comparison stars for V603 Aql. The side of the square of the finding chart is 5′ in length.

*Periods Close to the Orbital Period*

In searching for photometric periods close to the orbital period, we divided all of our observations into four groups (see Table 2) and searched for periods in each group independently. The results of our search for periods are also given in Table 2. The power spectra for all four groups are shown in Fig. 5. One period is dominant for each night. However, apart from the peak that corresponds to this period, the power spectrum also exhibits other, alias peaks that correspond to the beat periods between the fundamental period and the periods in the window spectrum. In general, the most significant peaks are those that correspond to the beats with a period of 1 day, although the beats with other periods are also important. The L2 program written by Kolpakov allows the window spectrum of the analyzed light curves to be computed; this can reveal alias peaks other than the beats with a period of 1 day. The alias peaks are marked by letters A in Fig. 5. At the same time, some of the less significant peaks are not aliases of the fundamental period and may correspond to independent oscillations. These periods are presented in column $P_2$ of Table 2. To check whether these oscillations are independent, we used a standard procedure: analysis of the power spectrum for the light curves with the fundamental period subtracted. In all cases, the chosen secondary periods or their alias peaks became dominant in the power spectrum.

It is clear from the results presented in Table 2 that the photometric period in 2001–2002 exceeded the orbital period and was fairly stable, $0\overset{d}{.}144$–$0\overset{d}{.}145$. In Fig. 6, the light curves are folded with the fundamental period.

We chose the period among the alias peaks from the condition that it be closest to the orbital period. Independent confirmation of the validity of the chosen periods is the detected night-to-night variability of V603 Aql in June 2001 and July 2002 with a period of about $3\overset{d}{.}3$ and $3\overset{d}{.}0$, respectively (Fig. 7). According to current views, this period is the precession period of an eccentric accretion disk, while the observed photometric periods of $0\overset{d}{.}1442$ and $0\overset{d}{.}1449$ are the beat periods between the orbital ($0\overset{d}{.}1385$) and precession periods of the binary.

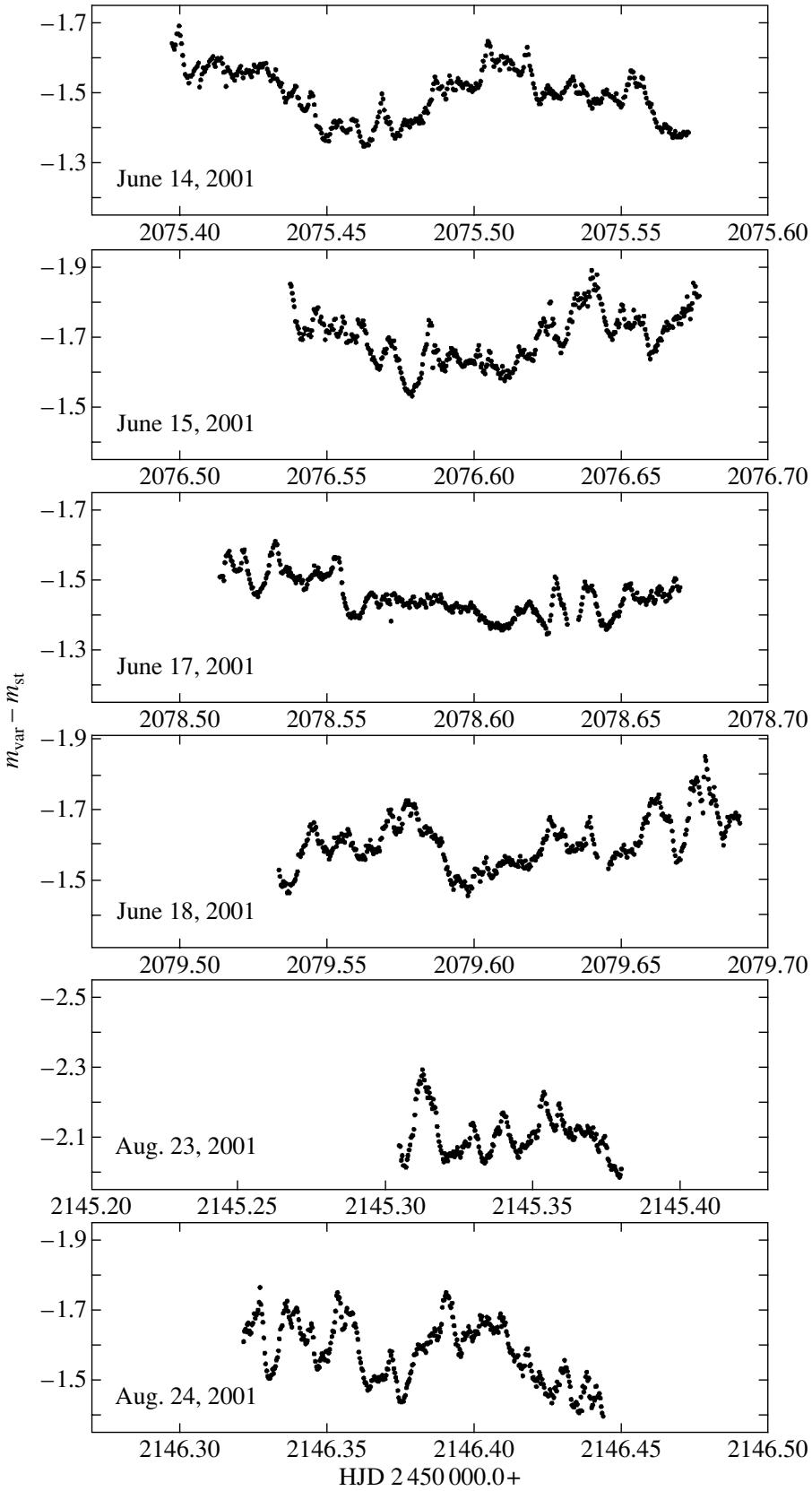


**Fig. 2.** Light curves for V603 Aql in 2001.

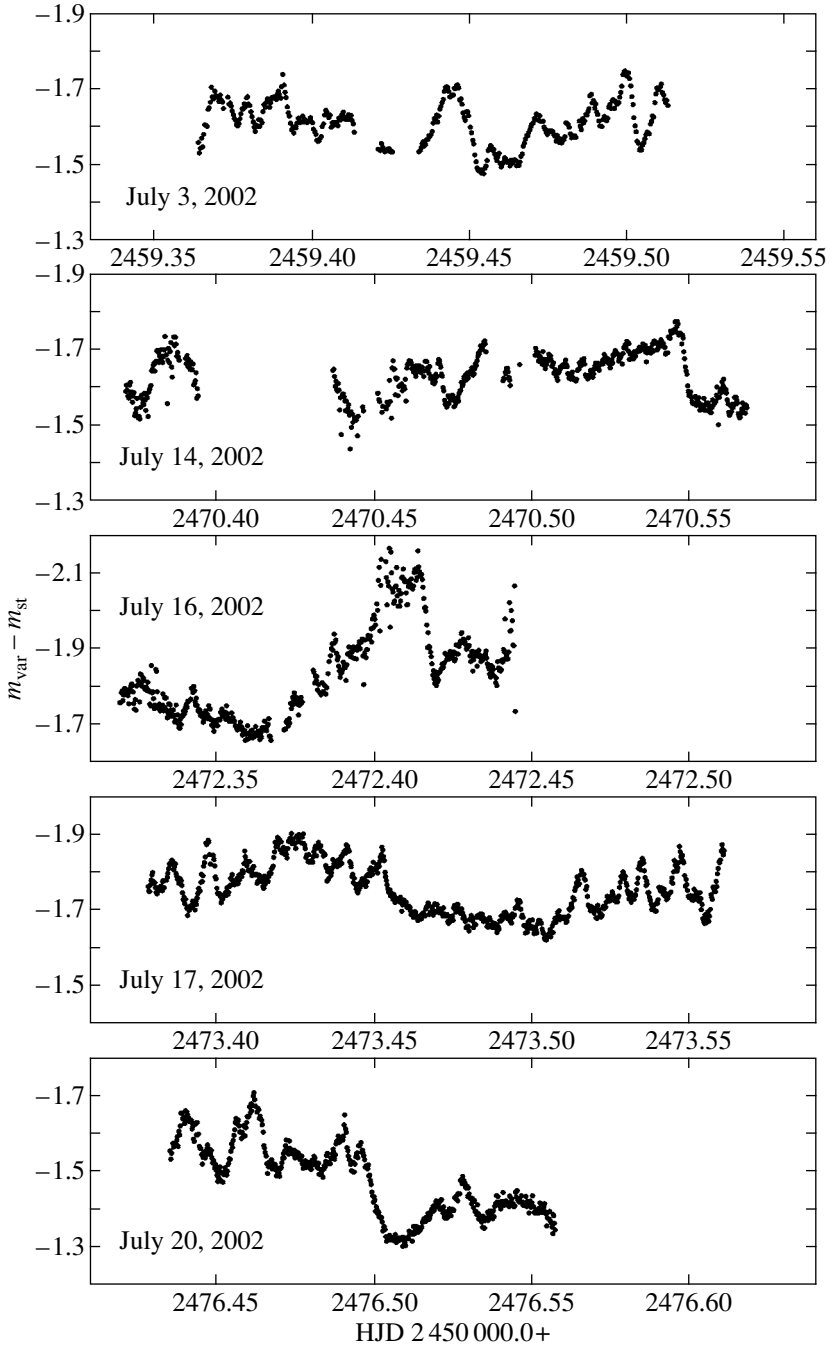


**Fig. 3.** Light curves for V603 Aql in 2002.

Analysis of the 1994 observations indicates that the photometric period was shorter than the orbital period. Consequently, the accretion disk in the binary V603 Aql underwent retrograde precession and was probably tilted with respect to the orbital plane. These data confirm those of Patterson *et al.* (1997). The star exhibited no detectable night-to-night brightness oscillations during this period.

### *Quasi-Periodic Brightness Oscillations*

To study the quasi-periodic brightness oscillations of V603 Aql on time scales of several tens of minutes that are clearly seen in the light curves (see Figs. 2–4), we analyzed the power spectra of the brightness variations on each individual night. The characteristic quasi-periods found on each night are

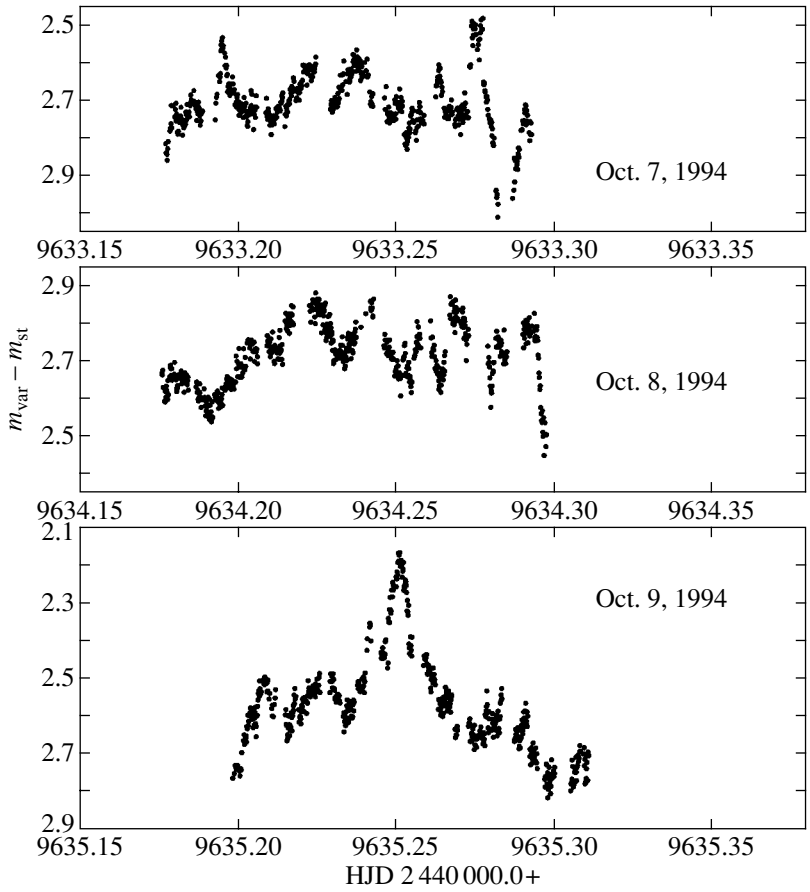


**Fig. 4.** Light curves for V603 Aql in 1994.

given in Table 3. The oscillations with periods of 19–25 min are the most prominent in the light curves.

The power spectra for individual nights in June 2001 are shown in Fig. 8. Several features can be noted. Clearly, the periods and amplitudes of the brightness oscillations change from night to night. In addition, brightness oscillations with periods that are multiples of the shorter periods are observed. The longer multiple periods generally have larger amplitudes, although these are fitted by a double or triple wave. Periods close to 61–62 min are observed on certain nights, but these oscillations fall far short of being recorded on each night.

An interesting feature is the change in the overall pattern of variability from night to night that is seen for the observations in June 2001 and July 2002. In particular, the variability amplitude on time scales of several tens of minutes on June 15 and 18, 2001, is much higher than that on June 17 and 19, 2001. This is also seen from the variability amplitude parameter in the power spectra on the same nights in Fig. 8. The same picture is also observed for the observations in July 2002. The amplitude of the quasi-periodic brightness oscillations on July 3, 14, 16, and 20 is higher than that on July 17, 2002. Note also that oscillations with a period of 9–10 min and often oscillations with periods that are multiples of this period (approximately 19, 40, and 60 min) also show up on the nights when the total oscillation amplitude is low. Oscillations with periods that are multiples of 9–10 min also show up on the nights when the oscillations with the fundamental period are undetectable. Other prominent periods are 11–15 min and their multiples.

It should be noted that the power spectrum also clearly shows the peaks associated with the beats between the brightness oscillations. Thus, for example, the peaks in the power spectrum that correspond to 11–12 min are probably the beats between the period of 9–10 min and the Keplerian period of the outer accretion disk, 50–70 min.

It is also clear that the amplitude of the quasi-periodic brightness oscillations in 1994 was higher than that in 2001–2002.

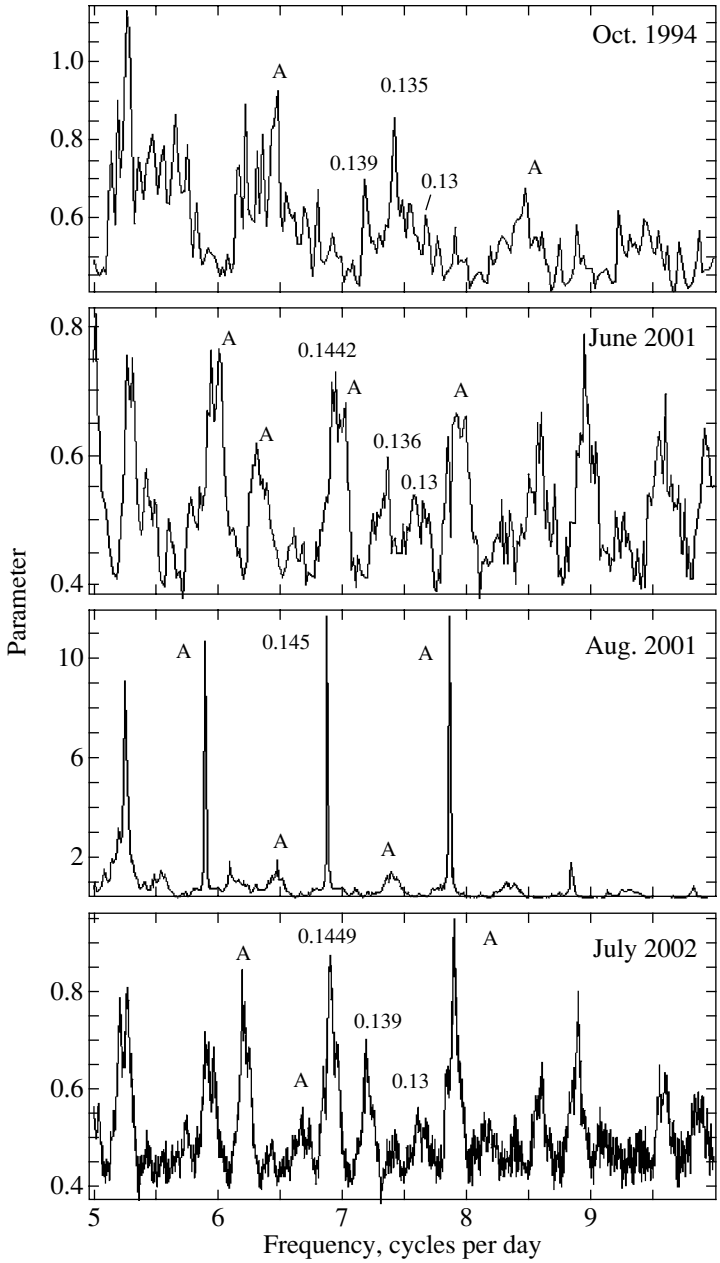


**Fig. 5.** Power spectra for the light curves of V603 Aql at four epochs of observations.

## DISCUSSION

### *Disk Precession*

The detected photometric periods suggest that the precession of the line of apsides was dominant in the dynamics of the accretion disk around V603 Aql in 2001–2002. Therefore, it is interesting to check how closely our periods correspond to the period–magnitude relation found for V603 Aql by Patterson *et al.* (1993) (Fig. 9a). We see that our periods fall nicely on this relation, which is simultaneously independent confirmation of both the validity of the detected periods and the validity of the reduction of the star's magnitude to Johnson's $V$ band. Given our data, the period–magnitude relation for the binary is

$$\frac{dP_{\rm pos}}{dm} = -0.009 \pm 0.0016. \quad (1)$$

The change in the photometric period suggests that the disk precession period changes, because

$$P_{\rm prec}^{-1} = P_{\rm orb}^{-1} - P_{\rm pos}^{-1}, \quad (2)$$

while the change in the apsidal precession period of an eccentric disk is commonly attributed to a change

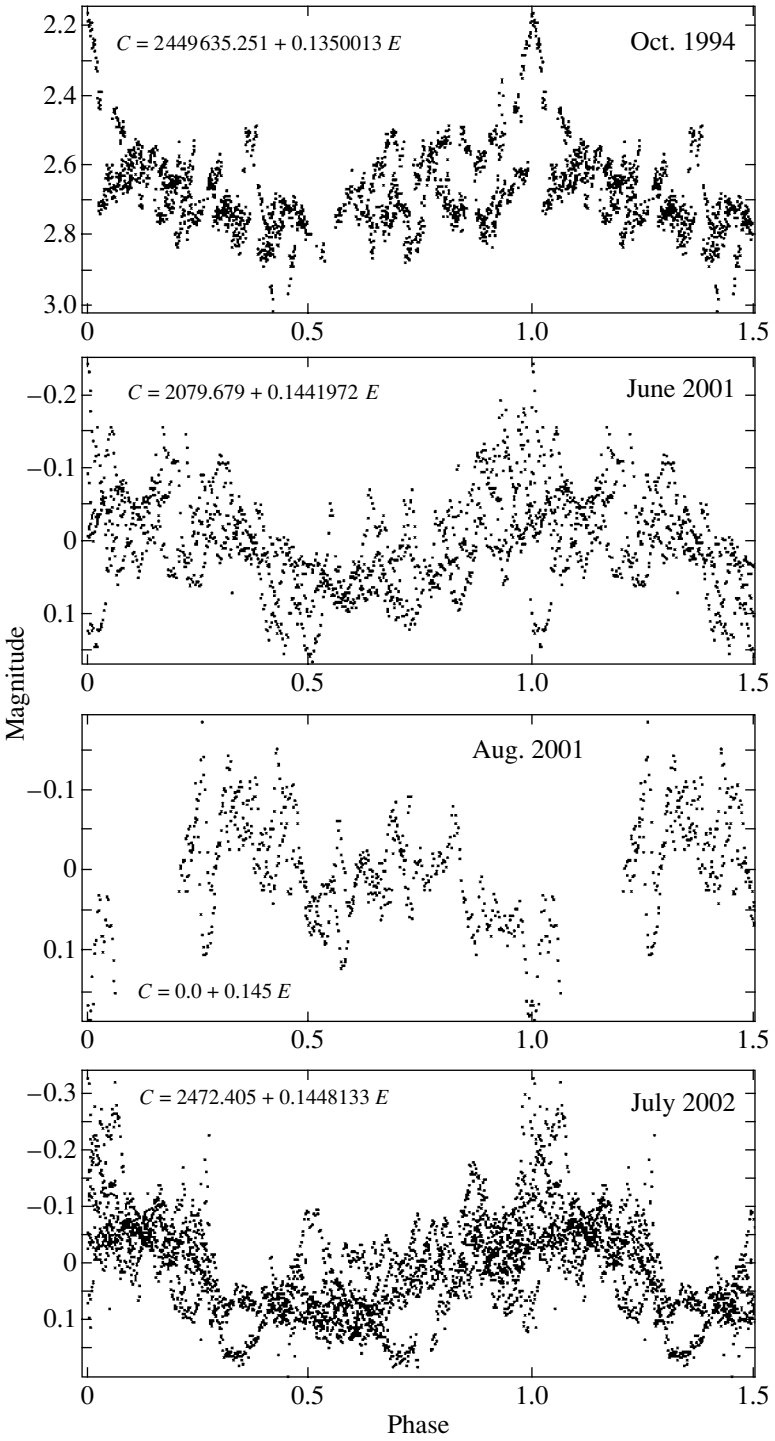


**Fig. 6.** Light curves of V603 Aql folded with the photometric periods for four epochs of observations.

in the outer radius of the accretion disk. Osaki (1985) derived a simple formula for the relationship between the precession period of an accretion disk and its size in the linear approximation:

$$P_{\rm prec}^{-1} = \frac{3}{4}\frac{q}{\sqrt{1+q}} r^{3/2} P_{\rm orb}^{-1}. \qquad (3)$$

Here, $r$ is the size of the disk in units of the separation $a$ between the components. The meaning of this relationship is clear: the larger the disk, the stronger the influence of the secondary component, and the faster the precession. Subsequently, this relationship was refined to include nonlinear terms (Murray 2000) and hydrodynamic effects (Montgomery 2001). The

**Table 3.** Found quasi-periods in the light curves of V603 Aql

| Date | Period, min | Amplitude |
|---|---|---|
| Oct. 7, 1994 | 57.3, 38.3, 28.2, 18.9, 9.1 | $0^m.20$, $0^m.16$, $0^m.1$, $0^m.09$, $0^m.06$ |
| Oct. 8, 1994 | 65.6, 45.9, 16.0, 11.9, 9.5 | 0.13, 0.13, 0.10, 0.07, 0.05 |
| Oct. 9, 1994 | 59.5, 29.6, 14.1, 11.2, 9.5 | 0.22, 0.17, 0.09, 0.06, 0.04 |
| June 14, 2001 | 61.2, 18.9, 14, 9.5 | 0.06, 0.03, 0.02, 0.02 |
| June 15, 2001 | 57.7, 24.8, 19.1, 11.52 | 0.12, 0.07, 0.04, 0.04 |
| June 17, 2001 | 24.3, 15.6, 11.8, 9.0 | 0.04, 0.04, 0.02, 0.015 |
| June 18, 2001 | 73.4, 37.8, 24, 19.2, 9.0 | 0.13, 0.08, 0.07, 0.05, 0.02 |
| Aug. 23, 2001 | 23.2, 15.6, 13.1, 9.2 | 0.13, 0.09, 0.08, 0.05 |
| Aug. 24, 2001 | 44.6, 26.9, 18.7, 15, 9.2 | 0.11, 0.09, 0.06, 0.06 0.04 |
| July 3, 2002 | 60.5, 39.7, 20.0, 14.4, 10.6 | 0.11, 0.12, 0.06, 0.05 0.03 |
| July 14, 2002 | 54.7, 36.6, 28.4, 19.7, 10.0 | 0.1, 0.08, 0.08, 0.04 0.03 |
| July 16, 2002 | 61.0, 47.4, 41.9, 20.7, 9.97 | 0.12, 0.14, 0.11, 0.07 0.03 |
| July 17, 2002 | 69.6, 46.0, 19.5, 15.4, 9.2 | 0.08, 0.07, 0.04, 0.04 0.02 |
| July 20, 2002 | 62.2, 49.1, 20.7, 11.6, 10.0 | 0.12, 0.13, 0.04, 0.03 0.02 |

latter give rise to spiral density waves in the disk whose influence must be taken into account (Bisikalo *et al.* 1998; Truss *et al.* 2001). Finally, the relationship between the precession period of the disk and its size is

$$P_{\rm prec}^{-1} = \left[ b(r)\frac{q}{\sqrt{1+q}} - \left(\frac{a_s}{a\tan i}\frac{P_{\rm orb}}{2\pi}\right)^2 \frac{1}{6r^2}\right] P_{\rm orb}^{-1}, \quad (4)$$

where $a_s$ is the speed of sound near the outer edge of the disk, and $i$ is the pitch angle of the spiral density waves. The function $b(r)$ is expressed in terms of the Laplace coefficients and is shown graphically in Fig. 1 from Murray (2000). Thus, the change in the disk precession period can be caused by a change in both the disk size and the spiral-wave pitch angle, although the latter seems unlikely. Assuming the temperature at the outer radius of the disk to be 3000 K, the pitch angle of the spiral waves to be 17° (Montgomery 2001), $q = 0.24 \pm 0.05$, and $P_{\rm orb} = 0^{\rm d}.1385$ (Arenas *et al.* 2000), we find that the change in the photometric period from $0^{\rm d}.1442$ to $0^{\rm d}.1466$ corresponds to the change in the radius from $0.345^{+0.04}_{-0.025}$ to $0.4^{+0.04}_{-0.025}$ $a$. Note that the contribution of the second term in Eq. (4) at the assumed parameters is about 4%.

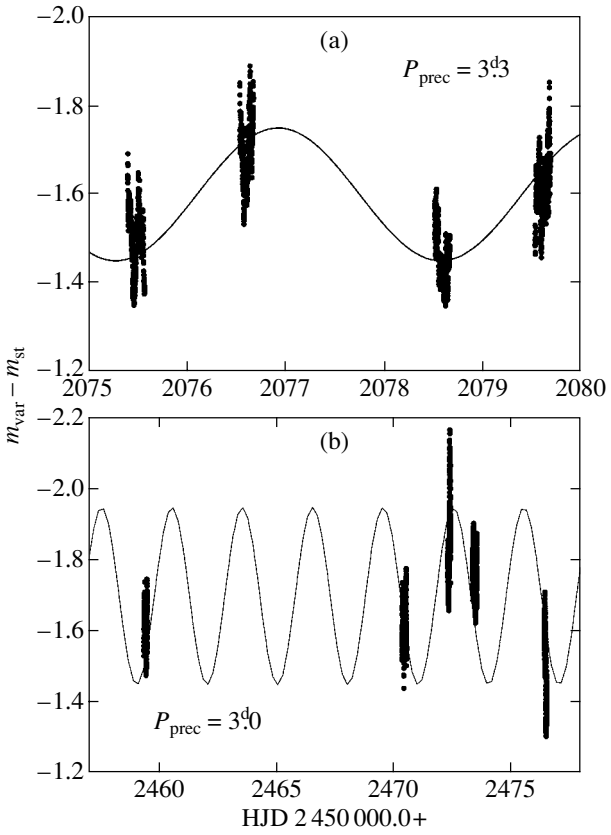


**Fig. 7.** Precession periods of V603 Aql in (a) June 2001 and (b) July 2002.

Formulas (3) and (4) were derived for disks in the orbital plane. We use them to estimate the size of the binary's disk in a state when the apsidal precession of the eccentric disk is dominant and the disk inclination to the orbital plane, if present, is small. For a circular disk tilted with respect to the orbital plane, there is also a relationship between the size, inclination, and precession period of the disk. However, there are no simple estimation formulas for the relationship between the precession period and the size of a precessing tilted eccentric disk. The dynamics of such a disk was numerically analyzed by Wood *et al.* (2000), who showed that a small (~5°) disk inclination does not

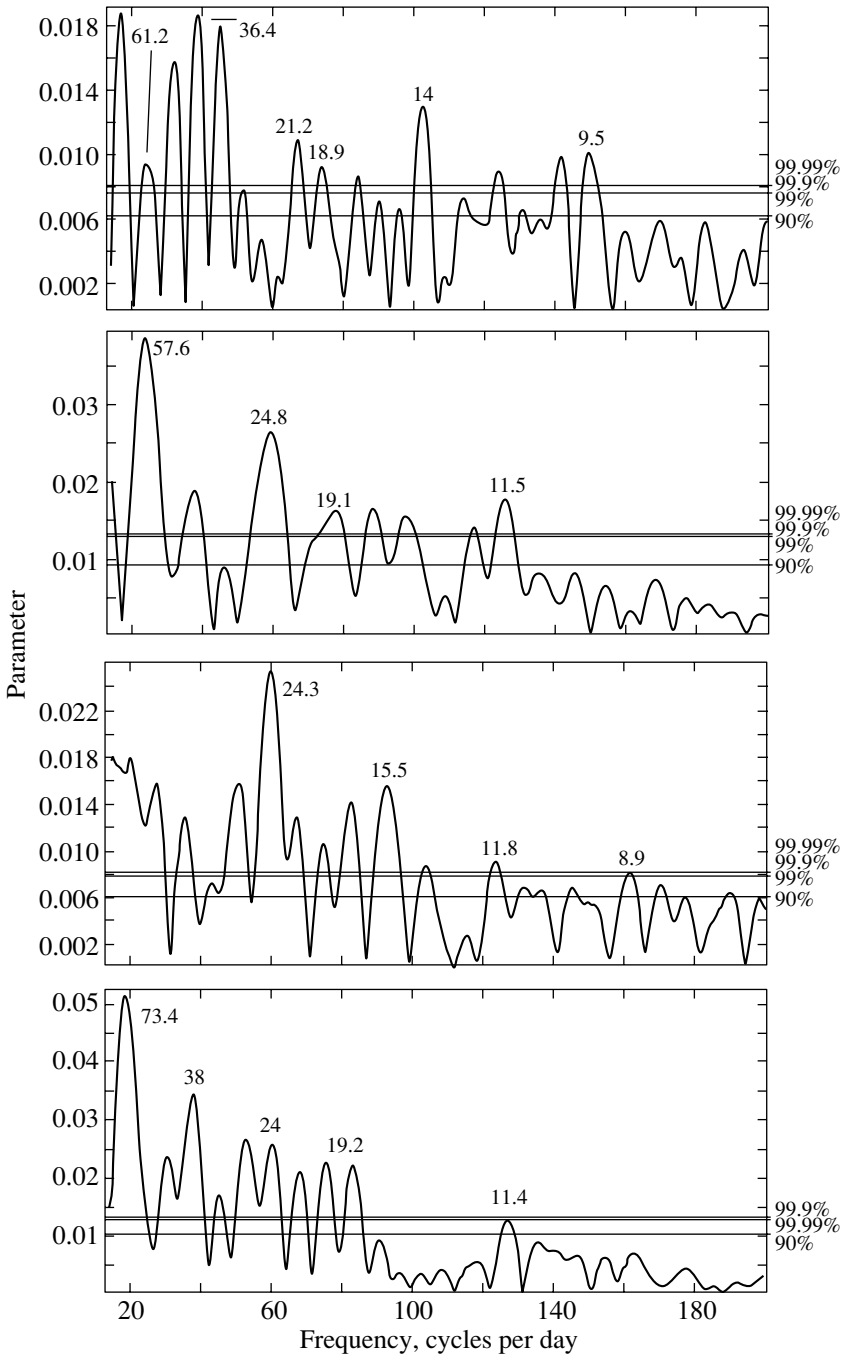


**Fig. 8.** Power spectra for the light curves of V603 Aql on individual nights in June 2001.

change the precession dynamics of the line of apsides of an eccentric disk. Since the disk inclination to the orbital plane is small in the state of V603 Aql under consideration (the apsidal precession is dominant), we believe that we have the right to use formulas (3) and (4) to estimate the size of the disk.

Consequently, when the radius of the disk changed by $0.055a$, the brightness changed by $0^m.3$ (see Fig. 9a), which yields

$$\frac{dr}{dm} = -0.183. \quad (5)$$

Let us consider what could be responsible for this relationship between the radius and brightness of the binary. We assume that the binary's brightness averaged over several days characterizes an average state

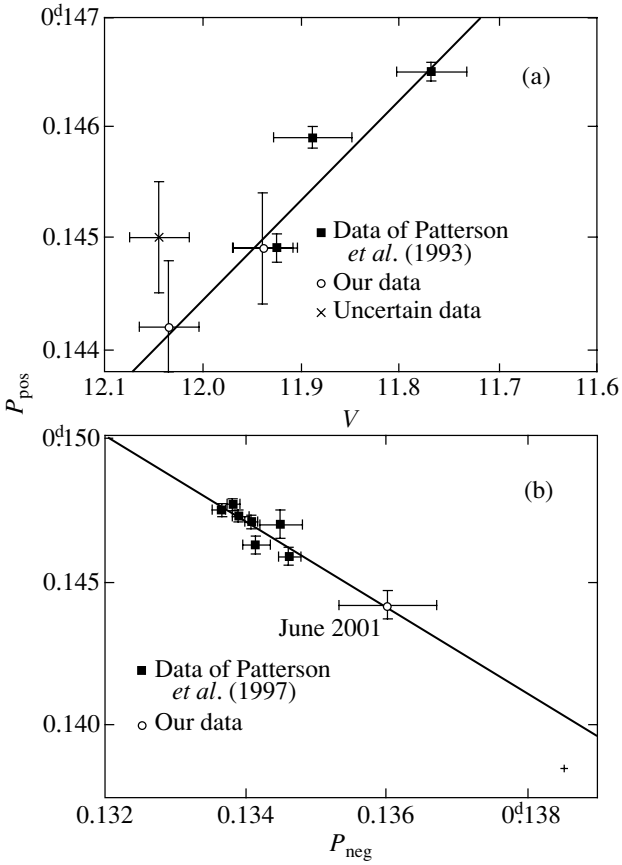


**Fig. 9.** (a) Photometric period–magnitude relation. The uncertain data for August 2001 are marked by crosses. (b) The relation between the periods of positive and negative superhumps.

of the accretion disk that can be described in terms of the standard theory of steady-state disk accretion (Shakura and Sunyaev 1973).

Let us consider several reasons why the brightness of the disk will change with its radius.

Patterson *et al.* (1993) attempted to apply the relationship between the brightness and size of the disk in dwarf novae during their outbursts. However, according to this relationship, the change in brightness must have been much larger (not $0^m.3$, but about $1^m$) for such a change in the radius. This comes as no surprise, because the disks of dwarf novae during their outbursts are highly nonstationary, while the disk of V603 Aql is in a quasi-steady state.

We may consider a situation where the radius of the binary's disk increases for some reason at a constant accretion rate. In this case, the bolometric luminosity of the binary increases, but if the $V$ band falls within the power-law ($F_\nu \sim \nu^{1/3}$) part of the disk spectrum, then the brightness will increase only slightly and all of the additional emissions will be observed at longer wavelengths. If the $V$ band was initially in the Rayleigh–Jeans part of the spectrum, then the change in brightness will be larger, but it must be accompanied by a change in $B-V$ by a comparable value, which is not observed (Bruch and Engel 1994). In principle, we can probably fit such parameters of the disk that the $V$-band brightness of the binary will increase by $0^m.3$ when the radius of the disk increases by $0.055a$. However, the results of this fitting will depend on the local disk spectra used.

Finally, we can assume that the change in brightness is attributable to an increase in the area of the part of the disk that emits in the $V$ band proportional to the increase in radius. Note that we observe disk precession at the outer radii that make the largest contribution to the $V$-band brightness. This range of radii, which make the largest contribution to the binary's visual brightness is characterized by the corresponding range of effective temperatures. Naturally, if this range of effective temperatures is located at larger radii, then the binary's visual brightness will increase due to the increase in the emitting area. The relationship between the disk radius and the effective temperature is well known (Shakura and Sunyaev 1973):

$$\sigma T_{\rm eff}^4 \approx \frac{3}{8\pi}\frac{GM_{\rm wd}\dot{M}}{R^3}.$$

Clearly, the radius at which a particular effective temperature is reached can increase only due to an increase in accretion rate $\dot{M}$.

The described situation is equivalent to considering the change in the outer radius of the disk due to a change in the accretion rate, provided that the effective temperature $T_{\rm out}$ at the outer edge of the disk remains constant. In this case, the outer radius of the disk will depend on the accretion rate as $R_{\rm out} \sim \dot{M}^{1/3}$. It is easy to show that the luminosity of the disk in the $V$ band (and at all the wavelengths at which the disk spectrum is $F_\lambda \sim \lambda^{-2.33}$) will then be proportional to the square of the outer radius. Therefore, the change in the $V$-band brightness of the disk with outer radius can be represented as

$$\Delta m = -2.5\log\left(\frac{R_{\rm out}}{R'_{\rm out}}\right)^2. \qquad (6)$$

When substituting the derived largest and smallest radii, 0.345 and $0.4a$, respectively, this relation yields a change in brightness by $0^m.32$, in excellent agreement with our observations. Thus, we conclude that the change in the radius and precession period of the disk could result from a change in the accretion rate.

In view of the derived relationship between the $V$-band brightness of the binary and the size of the disk, it is of interest to consider the cause of the binary's transition from the state with positive superhumps

to the state with negative superhumps. We assume that this transition is attributable to an increase in the accretion rate in the binary and, hence, to an increase in its brightness and the size of the accretion disk. Indeed, we can see from Table 1 that V603 Aql was, on average, about $0^m.3$ brighter in 1994 than it was in 2001–2002 (the mean brightness was $11^m.71$ and $11^m.99$, respectively). Approximately the same difference can be found in published observations of V603 Aql from 1991 (Patterson *et al.* 1993; the binary in the state with positive superhumps) and 1992–1994 (P97; the binary in the state with negative superhumps). The mean $B$ magnitude from Table 1 in the paper of 1993 is $11^m.86$; given the binary's color index $B - V = -0^m.04$ (Bruch and Engel 1994), it yields $V = 11^m.9$. The mean $V$ magnitude from Table 1 of P97 is $11^m.71$. During the observations of V603 Aql by Haefner and Metz (1985), the binary was in the state with positive superhumps and its $V$-band brightness was $11^m.8$–$12^m.0$ (see Fig. 1 in their paper). We conclude that V603 Aql in the state with negative superhumps was $0^m.2$–$0^m.3$ brighter than it was in the state with positive superhumps. According to relation (5) (if it is also valid under these conditions), this implies that the accretion disk of the binary in the state with negative superhumps is $0.037$–$0.056a$ larger than it is in the state with positive superhumps.

Hence, apsidal precession dominates in the observational manifestations at relatively small sizes of the disk, while the nodal precession of an eccentric disk tilted with respect to the orbital plane dominates when its size increases. This behavior of the disk can be explained most naturally if the disk inclination to the orbital plane is assumed to be different at different distances from the white dwarf; the larger the distance, the higher the inclination (see Fig. 10). therefore, a larger disk has a higher inclination. In turn, this behavior of the disk inclination with radius may provide evidence for the hypothesis that the disk inclination results from the influence of the magnetic field of the secondary component (for a discussion of this problem, see Murray *et al.* 2002). Indeed, since the influence of a dipole magnetic field of the secondary component tilted with respect to the spin axis must rapidly (as $R^{-3}$) weaken with increasing distance to it, the disk inclination caused by this magnetic field must also decrease.

Note that the disk inclination to the orbital plane in the scheme shown in Fig. 10 was grossly exaggerated for clarity. In particular, the deviation of the disk from the orbital plane calculated by Murray *et al.* (2002) is a few hundredths of the disk radius and is comparable to its half-thickness in the standard model. Therefore, the increase in the self-irradiation of the disk and its irradiation by the boundary layer caused by the increase in the disk inclination with radius cannot be significant. However, the enhanced visual brightness of the binary in the state with negative superhumps can be caused in part by an enhancement of the self-irradiation, and, hence, the increase in the radius (and accretion rate) obtained from relation (5) may prove to be overestimated.

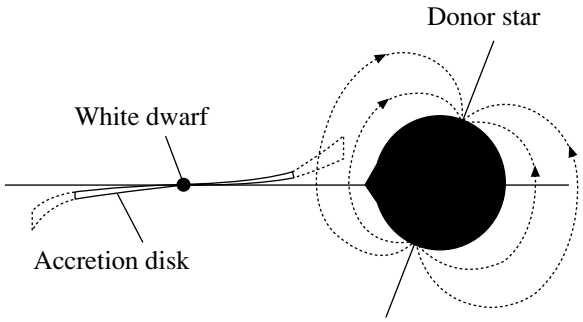


**Fig. 10.** Schematic view of the dependence of the inclination of an accretion disk to the orbital plane on its radius. The deviations of the disk from the orbital plane were exaggerated for clarity.

Another possible scenario for the binary's transition from one state to the other is not ruled out either. If the magnetic field of the secondary star undergoes periodic amplifications (an analogue of solar activity), then the influence of the magnetic field will be sometimes stronger and sometimes weaker, even at a constant accretion rate and accretion-disk radius. Consequently, the disk inclination will also sometimes increase and sometimes decrease. In this case, it would be natural to attribute the brightening of the binary to the increase in the disk self-irradiation. This scenario can be confirmed by the detection of cyclicity in the transition of V603 Aql from one state to another, but this may take several decades of observations.

The disk inclination to the orbital plane can also result from the instability of the disk against vertical perturbations under the tidal influence of the secondary component (Lubow 1992). The growth rate of this instability is much lower (a few percent) than the growth rate of the instability that leads to the disk eccentricity. Nevertheless, as in the previous model, a relatively large disk is probably more strongly affected by the instability that causes its inclination.

Let us consider the possible physical nature of other photometric periods. The period of $0^d.139$ is fairly close (within the $\pm 0^d.0005$ error limits) to the orbital period and is probably associated with it.

The period of $0^d.1360$ observed in June 2001 appears to be the period of negative superhumps. Our data point falls nicely on the relationship between

the periods of positive and negative superhumps (see Fig. 9b) found by Patterson *et al.* (1997).

The period of $0^d.13$ arouses considerable interest. Theoretical calculations of the precession dynamics of an eccentric tilted disk (Wood *et al.* 2000) predict that the following beat periods between the periods of positive and negative superhumps must be observed in the power spectra of the light curves for binaries with such disks:

$$P_b^{-1} = 2P_{\rm neg}^{-1} \pm P_{\rm pos}^{-1}. \quad (7)$$

The period corresponding to the negative sign for June 2001 is $0^d.129$, which is equal to the observed period of $0^d.13$, within the error limits. Thus, we conclude that this observed period could be the theoretically predicted beat period between positive and negative superhumps.

### *Quasi-Periodic Brightness Oscillations*

At present, the nature of the quasi-periodic brightness oscillations on times scales of several tens of minutes in binaries with precessing accretion disks remains unknown. To all appearances, their nature must somehow be associated with the disk precession. Two hypotheses have been put forward (see, e.g., Pavlenko and Shugarov 1999). First, this could be one or more blobs in the disk, and the periods of the brightness variations would then correspond to the Keplerian periods of these blobs. Second, according to King (1989), when the surface of the secondary star near the inner Lagrangian point is illuminated by hard radiation from the accretion disk and the boundary layer, ionization-front oscillations with a period $0.05P_{\rm orb}$ emerge, which cause the accretion rate to be modulated with the same period. This hypothesis looks attractive, because the inner Lagrangian point for a tilted disk is not shielded by the disk, and such an ionization front can emerge. For MV Lyra, this fundamental period was not detected, but its multiples were found (Pavlenko and Shugarov 1999). In our observations, the oscillation period of the ionization front (about 10 min for V603 Aql) on certain nights shows up at the detection limit. It seems natural that this period does not show up on each night, because the inner Lagrangian point is not always illuminated, due to the disk precession.

In the first hypothesis, the origin of the blobs remains unclear. The presence of spiral density waves may be responsible for their appearance. In particular, Bisikalo *et al.* (2001) showed that when mass transfer in a binary system ceases, a blob, a single-arm spiral wave (Fridman *et al.* 2003) whose Keplerian period is equal to 0.1–0.2 of the orbital period, is formed in its residual accretion disk. Such blobs may also be formed when the accretion rate changes.

## CONCLUSIONS

Our photometric $V$-band observations of the binary V603 Aql with the RTT 150 telescope have yielded the following results.

In 2001–2002, the binary was in a state with positive superhumps, and its photometric period ($0^d.144$–$0^d.145$) exceeded the orbital period, being proportional to its brightness: the higher the brightness, the longer the period.

We found periodic variations in the mean brightness of the binary from night to night. These variations agree with the disk precession periods deduced from the photometric period: $3^d.3$ and $3^d.0$ in 2001 and 2002, respectively.

Analysis of the results and their comparison with the results of other authors suggest that the change in the accretion rate could be responsible for the changes in the brightness of the binary and in the precession period of its accretion disk. The higher the accretion rate, the larger the radius of the disk (for the same effective temperature at the outer edge of the disk) and its luminosity. In turn, the larger the radius of the disk, the stronger the tidal influence on it from the secondary component, and the faster its precession.

We also found that, in the state with negative superhumps, V603 Aql is $0^m.2$–$0^m.3$ brighter than it is in the state with positive superhumps. Having assumed that these brightness variations were also attributable to the increase in the accretion rate and the disk sizes, we suggested that the disk inclination to the orbital plane at each radius depends on the distance of a given disk ring from the white dwarf. The farther the ring from the white dwarf, the higher its inclination to the orbital plane. Therefore, at a relatively low accretion rate and small sizes of the disk, the inclination of its outer parts to the orbital plane is small, and the apsidal precession of the eccentric disk is dominant in the photometric variability of the binary. As the accretion rate increases, the disk increases in size and its outer parts acquire an inclination to the orbital plane. In this case, the nodal precession is predominantly responsible for the binary's brightness variations, and the binary passes to the state with negative superhumps.

We analyzed other detected periods in the binary's brightness oscillations and probably found the theoretically predicted beat period between the periods of positive and negative superhumps.

The characteristic time scales of the binary's quasi-periodic brightness oscillations lie within the range 9–70 min and change from night to night. Oscillations with a period of 9–10 min and an amplitude of $0^m.02$–$0^m.03$ and their multiples show up on individual nights. These oscillations may result

from the accretion-rate modulation by ionization-front oscillations on the surface of the secondary star near the inner Lagrangian point. Such a front can appear at certain times when the secondary star is illuminated by hard radiation from the inner regions of a tilted precessing disk. However, oscillations unrelated to this period also show up, and their nature may be associated with the presence of blobs in the disk.

## ACKNOWLEDGMENTS

We wish to thank V. Goranskii and Yu. Kolpakov who provided the computer programs designed to search for and analyze periodicities in light curves. We are also grateful to the referees whose remarks improved the quality of the paper. This work was supported by the Russian Foundation for Basic Research (project no. 02-02-17174) and an RF Presidential grant for Support of Leading Scientific Schools (grant no. NSh-1789.2003.2).

## REFERENCES

1. I. L. Andronov and S. Yu. Shugarov, Astron. Tsirk., No. 1218 (1982).
2. J. Arenas, M. Catalan, T. Augusteijn, and A. Retter, Mon. Not. R. Astron. Soc. **311**, 135 (2000).
3. P. Barrett, D. O'Donoghue, and B. Warner, Mon. Not. R. Astron. Soc. **233**, 759 (1988).
4. D. V. Bisikalo, A. A. Boyarchuk, O. A. Kuznetsov, and V. M. Chechetkin, Astron. Zh. **75**, 706 (1998) [Astron. Rep. **42**, 621 (1998)].
5. D. V. Bisikalo, A. A. Boyarchuk, and A. A. Kil'pio, Astron. Zh. **78**, 707 (2001) [Astron. Rep. **45**, 611 (2001)].
6. G. V. Borisov, Astron. Astrophys. **261**, 154 (1992).
7. A. Bruch and A. Engel, Astron. Astrophys., Suppl. Ser. **104**, 79 (1994).
8. A. M. Fridman, A. A. Boyarchuk, D. V. Bisikalo, *et al.*, Phys. Lett. A (2003, in press).
9. Yu. N. Gnedin, N. V. Borisov, and T. M. Hatsvishvili, Pis'ma Astron. Zh. **16**, 635 (1990) [Sov. Astron. Lett. **16**, 272 (1990)].
10. R. Haefner and K. Metz, Astron. Astrophys. **145**, 311 (1985).
11. A. R. King, Mon. Not. R. Astron. Soc. **241**, 365 (1989).
12. R. Kraft, Astrophys. J. **139**, 457 (1964).
13. S. H. Lubow, Astrophys. J. **381**, 259 (1991).
14. S. H. Lubow, Astrophys. J. **398**, 525 (1992).
15. M. Montgomery, Mon. Not. R. Astron. Soc. **325**, 761 (2001).
16. J. R. Murray, Mon. Not. R. Astron. Soc. **314**, L1 (2000).
17. J. R. Murray, D. Chakrabarty, G. Wynn, and L. Kramer, Mon. Not. R. Astron. Soc. **335**, 247 (2002).
18. Y. Osaki, Astron. Astrophys. **144**, 369 (1985).
19. Y. Osaki, Publ. Astron. Soc. Jpn. **41**, 1005 (1989).
20. E. Pavlenko and S. Yu. Shugarov, Astron. Astrophys. **343**, 909 (1999).
21. J. Patterson and D. Skillman, Publ. Astron. Soc. Pac. **106**, 1141 (1994).
22. J. Patterson, G. Thomas, D. Skillman, and M. Diaz, Astrophys. J., Suppl. Ser. **86**, 235 (1993).
23. J. Patterson, J. Kemp, J. Saad, *et al.*, Publ. Astron. Soc. Pac. **109**, 468 (1997).
24. C. Payne-Gaposchkin, *The Galactic Novae* (North-Holland, 1957), p. 84.
25. H. Ritter and U. Kolb, Astron. Astrophys., Suppl. Ser. **129**, 83 (1998).
26. R. Schoembs, Astron. Astrophys. **115**, 190 (1982).
27. A. Schwarzenberg-Czerny, A. Udalski, and R. Monier, Astrophys. J. **401**, L19 (1992).
28. I. Semeniuk, A. Schwarzenberg-Czerny, H. Duerbeck, *et al.*, Acta Astron. **37**, 197 (1987).
29. N. I. Shakura and R. A. Sunyaev, Astron. Astrophys. **24**, 337 (1973).
30. D. Skillman, D. Harvey, J. Patterson, *et al.*, Astrophys. J. Lett. **503**, L67 (1998).
31. V. Suleimanov, G. Zhukov, and D. Senio, Astron. Astrophys. Trans. **15**, 117 (1998).
32. M. Truss, J. Murray, and G. Wynn, Mon. Not. R. Astron. Soc. **324**, L1 (2001).
33. A. Udalski, Acta Astron. **38**, 315 (1988).
34. A. Udalski and A. Schwarzenberg-Czerny, Acta Astron. **39**, 125 (1989).
35. N. Vogt, Astrophys. J. **252**, 653 (1982).
36. B. Warner, *Cataclysmic Variable Stars* (Cambridge Univ. Press, Cambridge, 1995).
37. R. Whitehurst, Mon. Not. R. Astron. Soc. **232**, 35 (1988).
38. R. Whitehurst and A. King, Mon. Not. R. Astron. Soc. **249**, 25 (1991).
39. M. Wood, M. Montgomery, and J. Simpson, Astrophys. J. **535**, L39 (2000).

*Translated by V. Astakhov*

*Astronomy Letters, Vol. 30, No. 9, 2004, pp. 630–633. Translated from Pis'ma v Astronomicheskiĭ Zhurnal, Vol. 30, No. 9, 2004, pp. 692–696.*


# Occultations of Stars Brighter Than $15^m$ by the Largest Trans-Neptunian Objects in 2004–2014

**D. V. Denissenko***

*Space Research Institute, Russian Academy of Sciences, Profsoyuznaya ul. 84/32, Moscow, 117997 Russia*

Received March 2, 2004

**Abstract**—We computed the occultations of stars brighter than $15^m$ by the largest trans-Neptunian objects (TNOs) for the next ten years. In our search, we used the following catalogs: Hipparcos; Tycho2 with the coordinates of 2 838 666 stars taken from UCAC2 (Herald 2003); and UCAC2 (Zacharias *et al.* 2003) with 16 356 096 stars between $12^m.00$ and $14^m.99$ north of $-45°$ declination. We predicted the occultations of stars by the seventeen largest numbered TNOs, the recently discovered 2004 DW, and four known binary Kuiper Belt objects. We selected 64 events at solar elongations of no less than 30°, including the extremely rare occultation of a $6^m.5$ star by the double asteroid (66 652) 1999 $RZ_{253}$ on October 4, 2007. Observations of these events by all available means are extremely important, since they can provide unique information about the sizes of TNOs and improve our knowledge of their orbits dramatically. © *2004 MAIK "Nauka/Interperiodica"*.

Key words: *trans-Neptunian objects, Kuiper Belt, stellar occultations.*

## INTRODUCTION

Over 800 trans-Neptunian objects (TNOs) have been discovered since 1992, 67 of which are numbered and 7 have proper names as of February 2004. No reliable measurements of their diameters have been obtained so far. The angular sizes of even the largest objects are about $0.04'' \pm 0.01''$ (Quaoar), which is at the resolution limit of the Hubble Space Telescope. Most of the size estimates are based on indirect methods that depend strongly on assumptions. The albedos of TNOs are commonly assumed to be 0.04–0.08, but their values clearly vary among different objects.

At present, the only direct method of measuring the sizes of single TNOs is to observe the occultations of stars by them. Over 500 occultations of stars by Main Belt asteroids have been observed so far, with five or more chords having been measured for 17% of them. For some objects, the sizes and shapes were determined with an equivalent angular resolution of $0.002''$ (Dunham *et al.* 2002). The predictions of close conjunctions with stars from 1999 until 2005 have been published for Centaurs (5145), Pholus, and (10 199) Chariklo (Stone *et al.* 2000), but no positive results have been obtained as yet.

## OCCULTATIONS BY TNOs

The distances of TNOs from the Earth are typically 30–50 AU, corresponding to a horizontal equatorial parallax of $0.2''$–$0.3''$. This implies that an occultation will occur somewhere on the Earth only if the geocentric path of the object will pass within 200–300 mas of the occulted star. In combination with the very slow angular motion of TNOs (0.1–1 mas $s^{-1}$), this makes the rate of stellar occultations by them about three orders of magnitude lower than that for Main Belt asteroids and a factor of about 100 lower than that for Jovian Trojans, i.e., inversely proportional to $a^2$.

Estimates show that any given TNO will occult a star brighter than $15^m$, on average, once every four or five years. We might expect one occultation in 10 years by 20 largest TNOs for $\sim 10^5$ HIPPARCOS stars brighter than $10$–$11^m$ and only one event in a century for $\sim 10^4$ stars brighter than $6.5^m$.

## THE ACCURACY OF STAR CATALOGS

An error in the coordinates of the occulted star can increase the uncertainty in both the time and position of the event. At a distance of 40 AU, 1 mas corresponds to 30 km. A $0.25''$ error in the star coordinates will shift the occultation path by $\sim 1$ Earth radius. Since the orbital positions of TNOs are known with $0.25''$ accuracy, an error of $0.05''$ in the star

*E-mail: denis@hea.iki.rssi.ru

1063-7737/04/3009-0630$26.00 

coordinates is acceptable. Before 2003, the coordinates with an accuracy of ∼1 mas were known for ∼100 000 stars in the HIPPARCOS catalogue. The Tycho2 catalogue, which includes about two million stars that are mostly brighter than $12^m$, is essentially a by-product of the same HIPPARCOS project. The systematic and statistical errors in the Tycho2 coordinates are typically within the range 0.1″–0.2″, but reach 0.5″–1.0″ in some fields of the sky. Thus, Tycho2 is unsatisfactory for predicting the occultations by Kuiper Belt objects.

The situation in astrometry changed radically in 2003 with the release of the second USNO CCD Astrograph Catalogue UCAC2 (Zacharias *et al.* 2003) with coordinates and proper motions for 48 million stars between $8^m$ and $16^m$. The positional errors in UCAC2 are 15–20 and 40–50 mas for $12^m$ and $15^m$ stars. This catalogue does not cover areas north of $+45^\circ \ldots +52^\circ$ declination, but this is not a problem, since none of the objects included in the current search will go beyond ±45° declinations over the next 10 years.

## PREDICTIONS FOR 2004–2014

The occultations of stars from January 27, 2004, until December 31, 2014, were computed for the following objects:

(a) The recently discovered largest known TNO 2004 DW with an absolute magnitude of $H_0 = 2.2$–2.4 (Marsden 2004);

(b) 17 numbered objects with $H_0 < 5.5$

2.6 (50 000) Quaoar
3.2 (28 978) Ixion
3.3 (55 565) 2002 $AW_{197}$
3.3 (55 636) 2002 $TX_{300}$
3.6 (55 637) 2002 $UX_{25}$
3.7 (20 000) Varuna
4.2 (42 301) 2001 $UR_{163}$
4.5 (19 308) 1996 $TO_{66}$
4.7 (26 375) 1999 $DE_9$
4.7 (38 628) Huya
4.8 (24 835) 1995 $SM_{55}$
4.9 (19 521) Chaos
4.9 (47 171) 1999 $TC_{36}$ (binary)
5.2 (26 181) 1996 $GQ_{21}$
5.3 (55 638) 2002 $VE_{95}$
5.4 (15 874) 1996 $TL_{66}$
5.4 (48 639) 1995 $TL_8$

(c) 3 numbered binary TNOs

5.8 (26 308) 1998 $SM_{165}$
5.9 (66 652) 1999 $RZ_{253}$
6.6 (58 534) 1997 $CQ_{29}$

(Trujillo and Brown 2002; Brown and Trujillo 2002; Noll and Stephens 2002; Noll and Stephens 2003).

The diameters of single bodies were estimated from their absolute magnitudes $H_0$ using the formula $\log D[\text{km}] = 3.52 - 0.2H_0$, which corresponds to the assumed albedo of 0.16 and is a conservative estimate. For (50 000) Quaoar, this formula yields 1000 km, in good agreement with the lower limit from the Hubble direct imaging ($1260 \pm 300$ km). If the albedo is 0.04, the actual TNO size will be exactly twice the value listed in the table. For binary asteroids with components of the same size and albedo, the diameter of each body will be $0.71 \times D$.

The orbits of the selected TNOs from astorb.dat as of January 27, 2004 (Bowell 2004) were integrated until the end of 2014 by taking into account the perturbations from major planets. Geocentric conjunctions within 0.5″ with HIP and UCAC2 stars were found. For 2004, the occultations by 36 largest unnumbered objects with $H_0 < 5.5$ were also computed, and nine events were found. The mean value of the current ephemeris uncertainty (CEU) was 0.26″ and 1.0″ for the numbered and unnumbered objects, respectively.

The results of our search are presented in the table. The table gives the time intervals (rounded off by 5 min) when an occultation can occur on the night side of the Earth with 0.25″ uncertainty. Due to the different velocity of TNOs relative to the Earth (from 25 km $s^{-1}$ at opposition to 5 km $s^{-1}$ or less near the stationary point), these intervals can vary from ∼ 10 min to 1.5 h for the occultation by Varuna in 2012. The extra 0.25″ were added for double asteroids, since the orbital distances in these pairs are also estimated to be 6000–8000 km.

The exceptional occultation of the $6^m.5$ K0 star HIP 111 398 = HD 213 780 = SAO 146 161 = ZC 3313 in Aquarius by the binary object (66 652) 1999 $RZ_{253}$ in 2007 should be particularly noted. It is extremely important to observe this TNO in 2004–2007 with large telescopes to refine the relative positions of the components at the occultation epoch. An international campaign involving observers in Australia, New Zealand, China, Japan, eastern Russia and Hawaii October 4, 2007 should be organized to measure the sizes and shape of this binary system.

Finding charts and preliminary path plots for the occultations listed here are available at http://hea.iki.rssi.ru/∼denis/TNOocc.html or may be requested by E-mail at denis@hea.iki.rssi.ru.

Occultations of stars by TNOs in 2004–2014

| Date of event | | | Time (UT) | Object | Diameter, | Dur., s | Star name | R.A. (2000.0) Dec | | | | | | Mag. |
|---|---|---|---|---|---|---|---|---|---|---|---|---|---|---|
| Year | Mon | DD | | name | km | | | hh | mm | ss.sss | dd | mm | ss.ss | |
| 2004 | Jan | 29 | 23:35–23:55 | 2003 AZ84 | 568 | 23.4 | 2UCAC 36806754 | 07 | 12 | 19.883 | +14 | 04 | 20.02 | $14^m.5$ |
| 2004 | Feb | 14 | 22:10–22:35 | 2001 XR254 | 255 | 14.2 | TYC 1343-00785-1 | 06 | 54 | 14.687 | +21 | 37 | 48.10 | 11.6 |
| 2004 | Mar | 07 | 03:15–03:30 | 2000 CO105 | 268 | 14.7 | 2UCAC 39141168 | 08 | 23 | 16.013 | +20 | 33 | 01.42 | 12.3 |
| 2004 | Mar | 08 | 02:10–02:25 | 1999 CC158 | 241 | 11.6 | 2UCAC 40185292 | 09 | 15 | 58.264 | +23 | 38 | 56.76 | 13.7 |
| 2004 | Mar | 20 | 13:35–13:45 | 1996 TL66 | 275 | 10.5 | 2UCAC 36232084 | 03 | 00 | 28.306 | +12 | 40 | 40.89 | 13.4 |
| 2004 | Mar | 27 | 00:20–00:40 | 2002 KW14 | 302 | 21.2 | 2UCAC 24855750 | 15 | 34 | 29.721 | −18 | 18 | 28.41 | 13.6 |
| 2004 | Apr | 07 | 10:30–11:00 | 2001 KD77 | 252 | 24.7 | 2UCAC 23658681 | 16 | 58 | 51.823 | −20 | 36 | 51.67 | 11.7 |
| 2004 | Jun | 26 | 19:55–20:05 | Chaos | 347 | 11.6 | 2UCAC 40137180 | 04 | 08 | 53.436 | +23 | 56 | 34.41 | 13.2 |
| 2004 | Jun | 29 | 18:25–19:10 | 1997 CQ29 | 158 | 9.5 | 2UCAC 34467578 | 11 | 04 | 07.504 | +07 | 39 | 54.56 | 14.5 |
| 2004 | Aug | 08 | 23:15–23:30 | 2001 QD298 | 257 | 10.5 | 2UCAC 24989527 | 21 | 52 | 30.098 | −18 | 08 | 13.32 | 14.5 |
| 2004 | Nov | 15 | 09:00–09:25 | 2000 CN105 | 340 | 32.5 | 2UCAC 35937214 | 10 | 34 | 08.639 | +11 | 59 | 33.61 | 14.3 |
| 2005 | Mar | 13 | 21:25–21:35 | 2002 UX25 | 631 | 21.6 | 2UCAC 34953654 | 01 | 37 | 42.194 | +09 | 22 | 06.65 | 13.2 |
| 2005 | May | 07 | 01:05–01:40 | 1999 RZ253 | 219 | 14.9 | 2UCAC 28298467 | 22 | 29 | 21.656 | −10 | 02 | 41.04 | 14.9 |
| 2005 | Sep | 29 | 07:50–08:10 | 1995 SM55 | 363 | 16.6 | 2UCAC 39255131 | 02 | 07 | 19.531 | +21 | 06 | 25.09 | 14.1 |
| 2005 | Oct | 24 | 08:05–08:30 | 1998 SM165 | 229 | 9.4 | 2UCAC 33162437 | 01 | 31 | 09.061 | +04 | 23 | 37.99 | 14.4 |
| 2005 | Dec | 27 | 09:15–09:35 | Huya | 380 | 17.9 | 2UCAC 30864992 | 14 | 20 | 27.168 | −02 | 54 | 42.58 | 11.7 |
| 2006 | Jun | 18 | 20:25–20:50 | 1999 KR16 | 229 | 17.4 | 2UCAC 28922119 | 14 | 18 | 38.914 | −08 | 29 | 05.17 | 13.7 |
| 2006 | Jul | 26 | 07:55–08:25 | Ixion | 759 | 55.9 | 2UCAC 22945926 | 16 | 34 | 14.971 | −22 | 04 | 37.89 | 13.7 |
| 2006 | Oct | 07 | 19:30–19:45 | Ixion | 759 | 36.0 | 2UCAC 22946030 | 16 | 35 | 05.045 | −22 | 11 | 08.86 | 13.8 |
| 2007 | Aug | 04 | 04:20–04:35 | 2002 VE95 | 288 | 15.8 | 2UCAC 35331886 | 04 | 14 | 47.942 | +10 | 08 | 18.19 | 13.0 |
| 2007 | Oct | 04 | 11:10–11:50 | 1999 RZ253 | 219 | 11.2 | HIP 111398 | 22 | 34 | 06.604 | −09 | 36 | 30.64 | 6.5 |
| 2008 | Jan | 22 | 06:55–07:30 | Chaos | 347 | 26.0 | 2UCAC 40810575 | 04 | 21 | 06.919 | +25 | 33 | 26.70 | 10.8 |
| 2008 | Feb | 11 | 04:20–04:40 | Varuna | 603 | 28.8 | TYC 1913-00670-1 | 07 | 18 | 50.100 | +25 | 43 | 19.31 | 11.3 |
| 2008 | Sep | 10 | 12:25–13:15 | Quaoar | 1000 | 149.5 | 2UCAC 26249129 | 17 | 05 | 49.913 | −15 | 20 | 44.26 | 13.7 |
| 2008 | Sep | 30 | 07:20–07:40 | Ixion | 759 | 44.6 | 2UCAC 22496420 | 16 | 44 | 05.610 | −23 | 18 | 07.11 | 13.6 |
| 2008 | Oct | 07 | 19:40–19:55 | Ixion | 759 | 37.3 | 2UCAC 22496543 | 16 | 44 | 33.933 | −23 | 19 | 19.45 | 12.8 |
| 2008 | Dec | 07 | 01:55–02:20 | Varuna | 603 | 29.0 | 2UCAC 40846256 | 07 | 29 | 48.171 | +25 | 40 | 07.71 | 14.8 |
| 2009 | Mar | 10 | 08:25–08:40 | 2002 VE95 | 288 | 19.7 | 2UCAC 34960757 | 04 | 17 | 00.297 | +09 | 18 | 45.63 | 13.3 |
| 2009 | May | 01 | 13:50–14:15 | Quaoar | 1000 | 54.1 | 2UCAC 26252549 | 17 | 18 | 12.542 | −15 | 24 | 49.90 | 14.3 |
| 2009 | Jul | 18 | 04:40–04:50 | 2002 VE95 | 288 | 10.8 | HIP 21308 | 04 | 34 | 30.274 | +10 | 00 | 58.46 | 7.7 |
| 2009 | Aug | 22 | 10:40–11:15 | 2002 UX25 | 631 | 68.5 | 2UCAC 35326247 | 02 | 09 | 00.114 | +10 | 07 | 56.40 | 14.1 |
| 2009 | Sep | 25 | 11:05–11:30 | 1995 TL8 | 275 | 15.1 | TYC 1223-00579-1 | 02 | 40 | 23.728 | +15 | 46 | 01.74 | 11.6 |
| 2009 | Oct | 09 | 10:15–10:35 | 2002 TX300 | 724 | 28.6 | 2UCAC 41650964 | 00 | 37 | 13.610 | +28 | 22 | 22.98 | 13.1 |
| 2009 | Oct | 15 | 17:55–18:10 | Quaoar | 1000 | 45.8 | 2UCAC 26023237 | 17 | 12 | 33.132 | −15 | 30 | 54.97 | 15.0 |
| 2010 | Feb | 19 | 22:55–23:20 | Varuna | 603 | 32.3 | TYC 1914-00301-1 | 07 | 29 | 22.470 | +26 | 07 | 23.23 | 11.0 |
| 2010 | Jul | 19 | 01:35–02:05 | Ixion | 759 | 42.4 | 2UCAC 22032118 | 16 | 54 | 25.862 | −24 | 24 | 22.86 | 11.5 |
| 2011 | Feb | 22 | 02:25–02:50 | 1995 TL8 | 275 | 18.3 | 2UCAC 37301105 | 02 | 39 | 37.120 | +15 | 41 | 48.75 | 13.6 |
| 2011 | Jun | 01 | 11:05–11:25 | Ixion | 759 | 30.3 | 2UCAC 21584537 | 17 | 03 | 39.446 | −25 | 01 | 27.82 | 14.7 |
| 2011 | Aug | 03 | 22:35–23:10 | 1999 RZ253 | 219 | 10.8 | 2UCAC 29384710 | 22 | 59 | 38.963 | −07 | 02 | 53.38 | 14.6 |
| 2011 | Nov | 04 | 00:35–00:50 | Quaoar | 1000 | 35.9 | 2UCAC 26027484 | 17 | 24 | 23.771 | −15 | 38 | 43.34 | 14.6 |
| 2011 | Dec | 18 | 11:40–12:50 | 1999 TC36 | 347 | 40.7 | 2UCAC 32137136 | 01 | 35 | 51.911 | +01 | 13 | 15.69 | 14.1 |
| 2012 | Apr | 16 | 04:20–04:55 | Ixion | 759 | 55.9 | TYC 6816-00401-1 | 17 | 12 | 26.791 | −25 | 34 | 10.85 | 10.8 |
| 2012 | May | 01 | 03:35–03:55 | 1999 RZ253 | 219 | 10.2 | 2UCAC 29759182 | 23 | 04 | 54.428 | −06 | 29 | 06.50 | 14.9 |
| 2012 | Jun | 01 | 17:55–18:15 | Quaoar | 1000 | 41.3 | 2UCAC 26259184 | 17 | 32 | 11.415 | −15 | 24 | 30.06 | 13.5 |
| 2012 | Jun | 04 | 01:10–01:30 | 1996 GQ21 | 302 | 14.0 | 2UCAC 28386513 | 15 | 19 | 25.744 | −09 | 50 | 28.94 | 14.8 |
| 2012 | Oct | 07 | 04:30–04:45 | 2002 AW197 | 724 | 30.2 | 2UCAC 32701289 | 09 | 34 | 01.570 | +02 | 31 | 43.27 | 14.7 |
| 2012 | Oct | 28 | 19:50–21:25 | Varuna | 603 | 144.8 | 2UCAC 41016878 | 07 | 53 | 29.509 | +26 | 05 | 51.86 | 13.4 |
| 2013 | Jan | 29 | 06:10–06:30 | Varuna | 603 | 24.2 | 2UCAC 41187592 | 07 | 47 | 50.499 | +26 | 31 | 18.27 | 14.8 |
| 2013 | Feb | 18 | 11:40–12:50 | Chaos | 347 | 93.9 | 2UCAC 41496855 | 04 | 49 | 59.491 | +27 | 50 | 52.79 | 14.4 |
| 2013 | May | 28 | 18:35–18:55 | 1999 KR16 | 229 | 10.1 | 2UCAC 29288802 | 15 | 13 | 08.695 | −07 | 07 | 13.91 | 11.7 |
| 2013 | Jun | 02 | 22:20–22:35 | Ixion | 759 | 30.4 | 2UCAC 21139770 | 17 | 14 | 19.280 | −26 | 08 | 23.27 | 14.4 |
| 2013 | Oct | 23 | 13:20–13:35 | Ixion | 759 | 31.3 | 2UCAC 21137306 | 17 | 10 | 57.419 | −26 | 07 | 23.91 | 14.2 |
| 2013 | Dec | 06 | 09:10–09:20 | Huya | 380 | 11.0 | TYC 5025-00448-1 | 15 | 39 | 28.493 | −05 | 37 | 11.16 | 10.1 |
| 2013 | Dec | 20 | 14:05–14:40 | 2002 TX300 | 724 | 55.4 | TYC 2276-01081-1 | 00 | 52 | 46.890 | +31 | 03 | 39.18 | 11.4 |
| 2013 | Dec | 27 | 17:20–17:50 | 1995 SM55 | 363 | 23.4 | 2UCAC 42006839 | 02 | 40 | 01.674 | +29 | 27 | 23.90 | 13.3 |
| 2014 | Jan | 24 | 01:35–01:50 | Quaoar | 1000 | 34.9 | 2UCAC 26041319 | 17 | 43 | 03.235 | −15 | 45 | 10.63 | 14.6 |
| 2014 | Mar | 01 | 16:30–16:45 | 2004 DW | 1200 | 45.9 | TYC 5476-00882-1 | 09 | 58 | 22.549 | −08 | 16 | 55.27 | 12.1 |
| 2014 | Mar | 10 | 15:25–15:55 | 1997 CQ29 | 158 | 6.3 | 2UCAC 32542503 | 11 | 58 | 36.918 | +02 | 28 | 27.68 | 11.9 |
| 2014 | Apr | 15 | 01:50–02:00 | 1996 TL66 | 275 | 9.9 | 2UCAC 34961430 | 04 | 26 | 07.463 | +09 | 23 | 13.78 | 14.7 |
| 2014 | Jul | 24 | 14:20–15:10 | Huya | 380 | 51.0 | TYC 5024-00589-1 | 15 | 36 | 41.149 | −04 | 36 | 29.35 | 11.7 |
| 2014 | Aug | 14 | 21:40–22:40 | 1996 GQ21 | 302 | 48.1 | HIP 75882 | 15 | 29 | 58.355 | −10 | 03 | 19.73 | 9.1 |
| 2014 | Sep | 13 | 08:35–09:20 | 2002 VE95 | 288 | 27.1 | 2UCAC 34784210 | 05 | 31 | 16.439 | +08 | 55 | 17.49 | 12.3 |
| 2014 | Oct | 20 | 14:45–15:25 | 1999 RZ253 | 219 | 12.4 | 2UCAC 29941401 | 23 | 09 | 49.521 | −05 | 59 | 47.15 | 14.5 |
| 2014 | Nov | 08 | 22:00–22:15 | Quaoar | 1000 | 35.4 | 2UCAC 26039148 | 17 | 40 | 27.392 | −15 | 41 | 59.91 | 13.9 |

## OBSERVING METHODS

Observations can be performed by several techniques and with various types of instrumentation. In principle, the highest temporal resolution is not required for occultations by TNOs. For event durations on the order of several tens of seconds and, in some cases, up to 2–3 min, 1–3 s integration time will already give an unprecedented chord measurement accuracy. Therefore, one can use a CCD array in both standard and drift-scan modes, photometers, high-sensitivity video cameras, and even visual observations with a stopwatch. The CCD readout time should be minimized by binning pixels and exposing a small window instead of a full frame. An optimal exposure time should be chosen on the basis of the magnitude of the occulted star and the detector sensitivity. Precise absolute timing of the star's disappearance and reappearance is not critical, since at ~5–10 min uncertainty in the event time, even 1-s accuracy will improve the orbital position of the object by two orders of magnitude. Measuring the event duration at one observing site will provide a lower limit on the size of the occulting body, which is a valuable result by itself. To determine the object's shape, at least three chords at different observatories within the path should be measured.

For the occultations of bright stars, fast photometers can provide measurements of the diameter of the occulted star with an unprecedented angular resolution. Since TNOs move at 0.1–1 mas $s^{-1}$ rate (a factor of 500–5000 slower than the Moon) against the stellar background, the occultations by them can reveal new close binaries that cannot be resolved by other methods.

## DISCUSSION

The search was deliberately limited to the largest objects with an ephemeris uncertainty of 0.3″ or better. Although smaller objects can (and definitely will!) occult brighter stars, the detection probability of such events would be much lower than that for the occultations listed here. It would be preferable to concentrate on 2–5 "special" events on each year. Success can be achieved only by preplanned joint efforts. Worldwide observations with as many telescopes as possible are necessary. The prediction of events till 2014 will allow one to make changes in the tight observing schedules of large telescopes in advance. Additional observations of the selected TNOs to improve their ephemerides and increase the prediction accuracy are highly desirable. New large objects will undoubtedly be discovered in the near future. Predictions of the occultations of stars by them will be posted at the author's site together with updates on those listed here.

After this paper had already been submitted, the discovery of 2003 $VB_{12}$ with unusual orbital parameters ($a \approx 510$ AU, $q \approx 76.1$ AU) and $H_0 = 1.5$–1.7 was announced. A search for its conjunctions with stars brighter than $15^m$ has given no occultation candidates for the next 10 years. However, the orbital elements of 2003 $VB_{12}$ require further improvement.

## POSSIBLE APPLICATIONS

Successful observations of stellar occultations by TNOs will make a contribution in several areas of astronomy at once. They will allow the following:

(1) To directly measure the sizes and shapes of distant objects in the Solar system with ~ 1% accuracy, which is unachievable by other methods;

(2) To reveal the TNO composition and, for binary systems, to directly measure their density using mass estimates from the orbital size and period;

(3) To improve the orbital position by a factor of 10–50, which can be valuable for space missions to TNOs;

(4) To discover probable close binary objects with separations between their components of ~1000 km.

(5) To give unique information and food for theorists to analyze the origin and evolution of the Solar system;

## ACKNOWLEDGEMENTS

I would like to thank A. Yascovich, who provided copies of the UCAC2 catalogue, and A. Plekhanov, who wrote the LinOccult program to draw maps of the occultation paths posted at the website.

## REFERENCES

1. E. Bowell, http://www.lowell.edu/users/elgb (2004).
2. M. E. Brown and C. A. Trujillo, IAU Circ., No. 7807 (2002).
3. D. W. Dunham, E. Goffin, J. Manek, *et al.*, Mem. Soc. Astr. Ital. **73**, 662 (2002).
4. D. Herald, Cat. 1291....0H (2003); http://vizier.u-strasbg.fr.
5. B. G. Marsden, Minor Planet Electronic Circ. 2004-D15 (2004).
6. K. Noll and D. Stephens, IAU Circ., No. 7824 (2002).
7. K. Noll and D. Stephens, IAU Circ., No. 8143 (2003).
8. R. C. Stone, S. W. McDonald, J. L. Elliot, and E. Bowell, Astron. J. **119**, 2008 (2000).
9. C. A. Trujillo and M. E. Brown, IAU Circ., No. 7787 (2002).
10. N. Zacharias, S. E. Urban, M. I. Zacharias, *et al.*, Cat. 1289....0Z (2003); http://vizier.u-strasbg.fr.

*Translated by D. Denissenko*

*Astronomy Letters, Vol. 30, No. 9, 2004, pp. 634–646. Translated from Pis'ma v Astronomicheskiĭ Zhurnal, Vol. 30, No. 9, 2004, pp. 697–710.*


# Equation of State under Nuclear Statistical Equilibrium Conditions

**D. K. Nadyozhin*** **and A. V. Yudin**

*Institute for Theoretical and Experimental Physics, ul. Bol'shaya Cheremushkinskaya 25, Moscow, 117259 Russia*

Received March 23, 2004

**Abstract**—We investigate a three-parameter equation of state for stellar matter under nuclear statistical equilibrium conditions in the ranges of temperatures $3 \times 10^9$–$10^{11}$ K and densities $10^4$–$10^{13}$ g cm$^{-3}$ and for various ratios of the total number of neutrons to the total number of protons within the range 1–1.5. These conditions correspond to the initial stages of the gravitational collapse of iron stellar cores that are accompanied by nonequilibrium matter neutronization. We analyze the effect of the excited levels of atomic nuclei on the thermodynamic properties of the matter. We show that this effect is insignificant at low densities, $\rho \lesssim 10^{10}$ g cm$^{-3}$, but it leads to an expansion of the instability region, $\gamma < 4/3$, at higher densities. The incorporated effects of the Fermi degeneracy of free nucleons prove to be insignificant, because their concentrations are low at low temperatures. In the future, we plan to investigate the effects of Coulomb interactions and neutron-rich nuclei on the thermodynamic properties of the matter.


Key words: *nuclear astrophysics, stars—structure and evolution.*

## INTRODUCTION

The evolution of high-mass stars ends with the depletion of all nuclear energy sources in their central regions, where the temperature and the density increase to $(4–8) \times 10^9$ K and $10^9$–$10^{10}$ g cm$^{-3}$, respectively. Under such physical conditions, all of the direct and reverse reactions proceed so fast that so-called nuclear statistical equilibrium (NSE) is established, when the concentrations of all nuclides and the thermodynamic properties of the matter are determined by thermodynamic equilibrium conditions (Hoyle 1946; Burbidge *et al.* 1957). In this case, the adiabatic index $\gamma$ becomes less than 4/3 over wide temperature and density ranges, which leads to the collapse of the central stellar core and to the subsequent supernova explosion (Hoyle 1946; Hoyle and Fowler 1960).

Studying the thermodynamic properties of stellar matter under NSE conditions is an important trend in the theory of the final evolutionary stages of stars and stellar nucleosynthesis. However, only a few authors have analyzed in detail the corresponding equation of state over wide temperature and density ranges—from the onset of the dissociation of iron-group elements to the predominance of free nucleons and $\alpha$ particles. By the equation of state, we mean the entire set of thermodynamic quantities (pressure, specific energy, and entropy) as functions of the temperature and the density. Apart from the temperature and the density, the equilibrium concentrations of the nuclides and the equation of state also depend on the ratio $\theta$ of the total number of protons to the total number of neutrons (both free and bound in atomic nuclei), which can change only under the influence of fairly slow $\beta$-processes.

Clifford and Tayler (1965) first calculated the concentrations of a large number (211) of nuclides in the ranges of temperatures $(2–9) \times 10^9$ K and densities $10^3$–$10^9$ g cm$^{-3}$ and for $\theta$ close to the nuclide stability band ($\theta = 1–1.25$). However, they did not consider the equation of state. Imshennik and Nadyozhin (1965) probably made the first attempt to study the equation of state in full. These authors made the following simplifying assumptions: the set of iron-group elements was represented by only one isotope, $^{56}$Fe, and a thermodynamic equilibrium of the $\beta$-processes with a zero neutrino chemical potential was assumed, which allowed $\theta$ to be excluded as the third independent variable. Nevertheless, this simplified formulation of the problem proved to be an adequate first approximation for ascertaining the main properties of the equation of state under NSE conditions. Imshennik and Chechetkin (1970) used the kinetic equilibrium approximation for the $\beta$-processes to determine $\theta$ as a function of the temperature and the density, elucidated the validity conditions for this approximation, and analyzed the

*E-mail: nadezhin@mail.itep.ru

1063-7737/04/3009-0634$26.00 

equation of state using the laws of thermodynamics for systems with a variable number of particles. El Eid and Hillebrandt (1980) considered the equation of state at subnuclear densities, $10^{12}$–$10^{14}$ g cm$^{-3}$, by taking into account the nonideality effects attributable to nucleon–nucleon nuclear interactions. Murphy (1980) discussed a three-parameter equation of state for densities and temperatures in the ranges $5 \times 10^{10}$–$5 \times 10^{13}$ g cm$^{-3}$ and $5 \times 10^{9}$–$5 \times 10^{11}$ K, respectively, and for a wide $\theta$ range (1.2–9). Such effects as the nuclear interaction and the presence of electron–positron pairs were disregarded in this work.

The main goal of this work is to study the equation of state described by three independent variables, $T$, $\rho$, and $\theta$, with an allowance made for such effects as the multiple excitation of nuclides and the partial degeneracy of free neutrons and protons. We pay particular attention to the ranges of densities $10^{4}$–$10^{13}$ g cm$^{-3}$ and temperatures (3–100) $\times 10^{9}$ K. These ranges incorporate the physical conditions that correspond to the initial neutrino-transparent stage of collapse, the most important stage for the detection of electron neutrinos from nonequilibrium stellar matter neutronization.

This work is the first step in implementing a project that envisages an analysis of the contribution from Coulomb interactions and highly neutron-rich nuclides to the equation of state. The nuclear interaction between nucleons can appreciably affect the equation of state only at densities $\rho \gtrsim 10^{13}$ g cm$^{-3}$ and at high temperatures, when a significant fraction of the heavy nuclides dissociate (El Eid and Hillebrandt 1980). These conditions correspond to a "deep," neutrino-opaque stage of collapse, in which the contribution from the neutrino component to the equation of state should be taken into account.

## BASIC RELATIONS

Instead of the number of nuclides per unit volume, $n$, it is convenient to use the dimensionless concentration $Y = m_{\rm u} n/\rho$ (where $\rho$ is the matter density, and $m_{\rm u}$ is the atomic mass unit), which is the number of nuclides per baryon. Under NSE conditions, the concentrations $Y$ of various nuclides $(A, Z)$ can be determined from the general chemical equilibrium equations that relate the chemical potentials $\mu$ of the reacting particles:

$$\mu_{A,Z} = (A - Z)\mu_{\rm n} + Z\mu_{\rm p}, \qquad (1)$$

where $\mu_{A,Z}$, $\mu_{\rm n}$, and $\mu_{\rm p}$ are the chemical potentials of the nuclide $(A, Z)$, neutrons n, and protons p, respectively.

For an ideal gas of nondegenerate and nonrelativistic particles,

$$\mu_i = m_i c^2 + kT \ln\left[\frac{n_i}{g_i}\left(\frac{h^2}{2\pi m_i kT}\right)^{3/2}\right], \qquad (2)$$

where $m_i c^2$ is the rest energy of the particles of type $i$, $n_i$ is the number of particles of type $i$ per unit volume, and $g_i = 2I_i + 1$ is their statistical weight. Given this expression for the chemical potential, the nuclide concentrations $Y_{A,Z}$ satisfy the equations

$$Y_{A,Z} = \frac{1}{2}\omega_{A,Z}\left(\frac{\widetilde{m}_{A,Z}}{\widetilde{m}_{\rm n}^{A-Z}\widetilde{m}_{\rm p}^{Z}}\right)^{3/2} \times \left(\frac{\lambda_T^3\rho}{2m_{\rm u}}\right)^{A-1} Y_{\rm n}^{A-Z} Y_{\rm p}^{Z} \exp\frac{Q_{A,Z}}{kT}, \qquad (3)$$

where $Q_{A,Z}$ is the binding energy of the nuclide $(A, Z)$; $\widetilde{m}_{A,Z}$, $\widetilde{m}_{\rm p}$, and $\widetilde{m}_{\rm n}$ are the atomic nucleus, proton, and neutron masses in atomic mass units $m_{\rm u}$; $\lambda_T \equiv \left(\frac{h^2}{2\pi m_{\rm u} kT}\right)^{1/2}$; and $\omega_{A,Z} = \sum_j (2I_j + 1)\exp(-E_j/kT)$ is the partition function of the nuclides, including the ground (nonexcited) state with $j = 0$, $E_0 = 0$, $I_0 = I_{\rm gs}$. The condition for the conservation of the total numbers of neutrons, $N_{\rm n}$, and protons, $N_{\rm p}$, in the system (both free and bound in atomic nuclei) fixed by a given density $\rho = m_{\rm u}(N_{\rm n} + N_{\rm p})$ and the specification of their ratio $\theta = N_{\rm n}/N_{\rm p}$ lead to two additional relations,

$$Y_{\rm n} + \sum_{A,Z}(A - Z)Y_{A,Z} = \frac{\theta}{1+\theta}, \qquad (4)$$

$$Y_{\rm p} + \sum_{A,Z} Z Y_{A,Z} = \frac{1}{1+\theta},$$

which together with Eqs. (3) allow the concentrations of all particles to be determined as functions of $\rho$, $T$, and $\theta$.

For the temperature $T_9 = 3$, the Fermi degeneracy of free neutrons and protons (heavy nuclei may be assumed to be nondegenerate up to the nuclear densities) becomes significant even at densities $\rho \gtrsim 10^{11}$ g cm$^{-3}$. Therefore, the Fermi–Dirac statistics should be used to determine the relationship between the chemical potentials $\mu_{\rm n,p}$ of the neutrons and protons and their concentrations $Y_{\rm n,p}$. The expansion of the corresponding integrals in terms of half-integer Fermi–Dirac functions (Blinnikov *et al.* 1996) that includes both the degeneracy and the relativistic corrections ensures a high accuracy up to nuclear densi-

ties and temperatures on the order of $T_9 = 500-1000$:

$$Y_{\rm n,p} = \frac{m_{\rm u}}{\rho\lambda_{\rm n,p}^3}\frac{\sqrt{2}}{\alpha_{\rm n,p}^{3/2}} \times \left[F_{1/2}\left(\psi_{\rm n,p}\right) + \frac{5}{4\alpha_{\rm n,p}}F_{3/2}\left(\psi_{\rm n,p}\right) + \frac{7}{32\alpha_{\rm n,p}^2}F_{5/2}(\psi_{\rm n,p})\right], \quad (5)$$

where $F_{1/2}, F_{3/2}, F_{5/2}$ are the half-integer Fermi–Dirac functions of the reduced neutron and proton chemical potentials (degeneracy parameters) $\psi_{\rm n}$ and $\psi_{\rm p}$:

$$\psi_{\rm n,p} = \frac{\mu_{\rm n,p} - m_{\rm n,p}c^2}{kT}, \quad (6)$$
$$\alpha_{\rm n,p} = \frac{m_{\rm n,p}c^2}{kT}, \quad \lambda_{\rm n,p}^3 = \frac{1}{8\pi}\left(\frac{h}{m_{\rm n,p}c}\right)^3.$$

Equations (3) should now be substituted with the equations

$$Y_{A,Z} = \omega_{A,Z}\widetilde{m}_{A,Z}^{3/2}\frac{m_{\rm u}}{\rho\lambda_T^3} \times \exp\left[(A-Z)\psi_{\rm n} + Z\psi_{\rm p} + \frac{Q_{A,Z}}{kT}\right]. \quad (7)$$

Below, we use the system of equations (4)–(7) to calculate the concentrations of all nuclides, including free neutrons and protons. Before performing such calculations, we must determine the set of nuclides $(A, Z)$ that can contribute appreciably to the equation of state. It is well known that, apart from $^4$He, only the nuclides that represent the iron-group elements with the highest binding energy per nucleon can have appreciable concentrations under NSE conditions. Therefore, in addition to $^4$He, we take into account the isotopes of the elements ranging from Ca to Kr in our calculations. For a smoother transition from the iron group to $^4$He, we also include the following chain of stable $\alpha$ nuclides in our calculations: $^{12}$C, $^{16}$O, $^{20}$Ne, $^{24}$Mg, $^{28}$Si, $^{32}$S, and $^{36}$Ar. A detailed analysis indicates that even–even nuclides (with even $A$ and $Z$) dominate under NSE conditions at moderately high temperatures ($T_9 \lesssim 8$). At higher temperatures, odd–even and odd–odd nuclides can also have appreciable concentrations. Apart from free neutrons and protons, we included 137 nuclides in our calculations. These are listed in the table, which also gives the ground-state spins $I_{\rm gs}$ and the number of experimentally known excited levels $N_{\rm ex}$ that were used in our calculations. The nuclide binding energies and the excited-level parameters were taken from the online NUCLEUS (Potet *et al.* 1995) and Isotope Explorer (Chu *et al.* 1999) databases, respectively.

## THE INCLUSION OF EXCITED LEVELS

The influence of excited levels of atomic nuclei on the equation of state is one of the most important effects that simultaneously have the largest uncertainty. However, the wide variety of approaches in this field makes it possible to find a trade-off between the accuracy of the result obtained, the ease of calculation, and the uniformity that allows acceptable results to be obtained for the large number of nuclei under consideration. For the reasons given below, we divide the domain of the nuclear partition functions into low- and high-temperature subdomains with the boundary at $T_9 = 40$. In all equations of this section, the temperature is measured in energy units ($k = 1$).

### *The Low-Temperature Range* ($T_9 < 40$)

Based on the paper by Rauscher *et al.* (1997), we use the standard model of a noninteracting Fermi gas (a statistical model of the nucleus) in this temperature range that well describes the results of the much more cumbersome combinatorial approach, the Monte Carlo method, etc. for an appropriate choice of parameters. In this case, the nuclear partition function is defined by

$$\omega(T) = \sum_{i=0}^{N}(2I_i+1)e^{-\frac{E_i}{T}} + \int_{E_N}^{\infty}\rho(E_{\rm ex})e^{-\frac{E_{\rm ex}}{T}}dE_{\rm ex}, \quad (8)$$

where the first term describes the summation over the experimentally known low-lying energy levels up to $E_N$, and the second term reproduces the contribution from the remaining energy levels. In the model of a Fermi gas,

$$\rho(E_{\rm ex}) = \frac{\sqrt{\pi}}{12a^{1/4}}\frac{\exp(2\sqrt{aU})}{U^{5/4}}, \qquad U = E_{\rm ex} - \delta. \quad (9)$$

The parameters $a$ and $\delta$ that describe, among other things, the shell and nucleon correlation effects are determined in accordance with the results by Rauscher *et al.* (1997).

The statistical model for the level density described above is inapplicable at $E_{\rm ex} \sim \delta(A, Z)$ if $\delta$ is positive. In this range of excitation energies, in addition to data on the experimentally known energy levels, we use the so-called constant-temperature formula

$$\rho(E_{\rm ex}) \sim \exp\left(\frac{U}{T_{\rm nuc}}\right), \quad (10)$$

where the parameter $T_{\rm nuc}$ and the preexponential factor can be determined from the continuity condition for the function $\rho(E_{\rm ex})$ and its derivative while going to formula (10) for the level density.

Nuclides included in the calculations

| $Z$ | $A$ | $I_{gs}$ | $N_{ex}$ | $Z$ | $A$ | $I_{gs}$ | $N_{ex}$ |
|---|---|---|---|---|---|---|---|
| He 2 | **4** | 0 | 15 | Fe 26 | 52, 53, **54** | 0, 3.5, 0 | 20, 21, 50 |
| C 6 | **1**2 | 0 | 55 | | 55, **56, 57** | 1.5, 0, 0.5 | 42, 111, 65 |
| O 8 | **1**6 | 0 | 75 | | **58**, 59,60 | 0, 1.5, 0 | 66, 40, 24 |
| Ne 10 | **20** | 0 | 131 | | 61, 62 | 1.5, 0 | 4, 10 |
| Mg 12 | **24** | 0 | 94 | Co 27 | 55, 56, 57 | 3.5, 4, 3.5 | 72, 26, 94 |
| Si 14 | **28** | 0 | 188 | | 58, **59**,60 | 2, 3.5, 5 | 92, 73, 105 |
| S 16 | **32** | 0 | 25 | | 61, 62, 63 | 3.5, 2, 3.5 | 29, 15, 6 |
| Ar 18 | **36** | 0 | 33 | | 64, 65 | 1, 3.5 | 8, 1 |
| Ca 20 | **40**, 41, **42** | 0, 3.5, 0 | 98, 28, 107 | Ni 28 | 56, 57, **58** | 0, 1.5, 0 | 22, 2, 30 |
| | **43, 44**, 45 | 3.5, 0, 3.5 | 73, 71, 41 | | 59,**60, 61** | 1.5, 0, 1.5 | 68, 82, 76 |
| | **46**, 47,**48*** | 0, 3.5, 0 | 46, 15, 10 | | **62**,63,**64** | 0, 0.5, 0 | 67, 12, 64 |
| Sc 21 | 43, 44, **45** | 3.5, 2, 3.5 | 66, 56, 85 | | 65, 66 | 2.5, 0 | 10, 20 |
| | 46, 47, 48 | 4, 3.5, 6 | 96, 41, 46 | Cu 29 | 61, 62, **63** | 1.5, 0, 1.5 | 58, 65, 80 |
| | 49 | 3.5 | 1 | | 64, **65**,66 | 1, 1.5, 1 | 90, 19, 18 |
| Ti 22 | 44, 45, **46** | 0, 3.5, 0 | 26, 24, 104 | | 67, 68, 69 | 1.5, 1, 1.5 | 2, 3, 6 |
| | **47, 48, 49** | 2.5, 0, 3.5 | 66, 218, 35 | Zn 30 | **64**,65, **66** | 0, 2.5, 0 | 101, 15, 98 |
| | **50**,51 | 0, 1.5 | 39, 13 | | **67, 68**, 69 | 2.5, 0, 0.5 | 29, 50, 27 |
| V 23 | 47, 48, 49 | 1.5, 4, 3.5 | 21, 52, 79 | | **70** | 0 | 22 |
| | **50***, **51**, 52 | 6, 3.5, 3 | 65, 109, 30 | Ga 31 | **69, 71** | 1.5, 1.5 | 17, 15 |
| | 53 | 3.5 | 22 | Ge 32 | **70**, 71, **72** | 0, 0.5, 0 | 115, 58, 112 |
| Cr 24 | 48, 49, **50** | 0, 2.5, 0 | 17, 11, 79 | | **73,74**,75 | 4.5, 0, 0.5 | 8, 137, 49 |
| | 51, **52, 53** | 3.5, 0, 1.5 | 100, 86, 65 | | **76*** | 0 | 68 |
| | **54**, 55, 56 | 0, 1.5, 0 | 61, 31, 21 | As 33 | 71,**75** | 2.5, 1.5 | 24, 58 |
| | 57 | 1.5 | 1 | Se 34 | **74, 76, 78** | 0, 0, 0 | 56, 91, 95 |
| Mn 25 | 51, 52, 53 | 2.5, 6, 3.5 | 44, 41, 65 | | **80, 82***, 83 | 0, 0, 4.5 | 53, 18, 10 |
| | 54, **55**, 56 | 3, 2.5, 3 | 52, 90, 78 | | 84, 85, 86 | 0, 2.5, 0 | 20, 1, 1 |
| | 57, 58, 59 | 2.5, 1, 1.5 | 33, 17, 2 | | 87, 88, 89 | 2.5, 0, 2.5 | 1, 1, 1 |
| | | | | Br 35 | **79, 81** | 1.5, 1.5 | 53, 42 |
| | | | | Kr 36 | **78, 80, 82** | 0, 0, 0 | 53, 23, 28 |
| | | | | | **83, 84**, 86 | 4.5, 0, 0 | 24, 31, 7 |

Note: Stable nuclides are highlighted in bold.

* Formally, $^{48}$Ca, $^{50}$V, $^{76}$Ge, and $^{82}$Se are unstable isotopes. Their half-lifes are $5.1 \times 10^{19}$, $1.5 \times 10^{17}$, $1.09 \times 10^{21}$, and $1.21 \times 10^{20}$ yr, respectively.

Using Eq. (8) for the partition function with the level density from (9) involves two difficulties. The first difficulty is obvious and consists in extending the integration over the excitation energy in the second term of Eq. (8) to infinity. Clearly, the excitation energy $E_{ex}$ cannot be higher than the nuclear binding energy $Q_{A,Z}$; moreover, the level density cannot be exponentially high at $E_{ex} \approx Q_{A,Z}$, because there remain progressively fewer possibilities to distribute the nucleons in states in such a way that none of

them and no combination of them, for example, an $\alpha$ particle, would have energies higher than their separation energy. To determine the influence of the energy levels with $E_{\rm ex} \approx Q_{A,Z}$ on the partition function, we compared the results of the integration over the excitation energy in Eq. (8) to infinity and to half the binding energy and found this effect to be negligible for the low-temperature range. Hence, it is justifiable to extend the integration in (8) to infinity. The second difficulty, which has repeatedly been discussed in the literature (see, e.g., Fowler *et al.* (1978) and Mazurek *et al.* (1979)), is that Eq. (9) also includes the states with nucleons excited above their separation energy. To subtract these states, we use the approximate procedure described below, which allows the magnitude of this effect to be estimated.

If a nucleon is excited above its separation energy, then these states pertain to the "nucleon + residual nucleus" system rather than to the original nucleus. The number of free states for a nucleon in a nucleus (for definiteness, let us first consider neutrons) in the energy range $\epsilon$–$(\epsilon + d\epsilon)$ is

$$\eta(\epsilon)d\epsilon = 2\frac{\frac{4\pi}{3}R_{A,Z}^3}{(hc)^3}4\pi\sqrt{2m_{\rm n}c^2\epsilon+\epsilon^2}(\epsilon+m_{\rm n}c^2) \times \left[1-\frac{1}{e^{\frac{\epsilon}{T}-\psi_{\rm n}}+1}\right]d\epsilon. \quad (11)$$

Here, $m_{\rm n}$ and $\psi_{\rm n}$ are the neutron mass and chemical potential, respectively, and $R_{A,Z}$ is the radius of the original nucleus. The excitation energy of the original nucleus $E_{\rm ex}$ is divided between the neutron and the residual nucleus (we ignore the recoil energy):

$$E_{\rm ex} = E_{\rm ex}^{\rm new} + S_{\rm n} + \epsilon, \quad (12)$$

where $E_{\rm ex}^{\rm new}$ is the excitation energy of the nucleus $(A-1, Z)$, and $S_{\rm n} = Q_{A,Z} - Q_{A-1,Z}$ is the neutron separation energy.

The total number of continuum states can be found as the product of the number of neutron states $\eta(\epsilon)d\epsilon$ and the number of states of the residual nucleus, which is expressed in terms of its state density $\rho_{A-1,Z}(E_{\rm ex}^{\rm new})$ with the excitation energy $E_{\rm ex}^{\rm new}$ defined by Eq. (12). Here, we disregard the momentum and parity selection rules that would cause the number of possible states to decrease, thereby placing an upper limit on the magnitude of the continuum effect. The corrected state density is then

$$\rho_{A,Z}^{\rm corr}(E_{\rm ex}) = \rho_{A,Z}(E_{\rm ex}) - \int_0^\infty\int_0^\infty \rho_{A-1,Z}(E_{\rm ex}^{\rm new})\eta(\epsilon) \times \delta(E_{\rm ex} - E_{\rm ex}^{\rm new} - S_{\rm n} - \epsilon)dE_{\rm ex}^{\rm new}d\epsilon,$$

where $\delta(E_{\rm ex} - E_{\rm ex}^{\rm new} - S_{\rm n} - \epsilon)$ is the delta function. As a result of using the uncorrected value of $\rho_{A-1,Z}$ in the integrand, we take into account not just the states with one excited neutron, but all of the states with *at least one* excited neutron, because $\rho_{A-1,Z}$ contains the continuum eigenstates. Multiplying the expression by $e^{-E_{\rm ex}/T}$ and integrating now yield the corrected value of the partition function

$$\omega_{A,Z}^{\rm corr} = \omega_{A,Z} - \omega_{A-1,Z}\,P_{\rm n}, \quad (13)$$

$$P_{\rm n} = \frac{4\pi R_{A,Z}^3}{3}\,n_{\rm n}(\psi_{\rm n},T)\,e^{-\frac{S_{\rm n}}{T}-\psi_{\rm n}}.$$

Here, $n_{\rm n}(\psi_{\rm n},T)$ is the neutron concentration as a function of the temperature and the chemical potential, the dependence on which describes the possibility of the existence of nucleon states with energies above the separation energy $S_{\rm n}$ when the decay with neutron escape is forbidden by the Pauli principle. Taking into account the same contribution from protons, we obtain the following formula for estimating the magnitude of the effect of continuum states on the nuclear partition function in the first approximation:

$$\omega_{A,Z}^{\rm corr} = \omega_{A,Z} - \omega_{A-1,Z}P_{\rm n} - \omega_{A-1,Z-1}P_{\rm p}, \quad (14)$$

where $P_{\rm p}$ is defined by analogy with $P_{\rm n}$, and $\omega_{A-1,Z-1}$ is the partition function of the nucleus $(A-1, Z-1)$. To show how the derived expression for the corrected partition function matches up with previous works, let us consider the case of nonrelativistic and nondegenerate nucleons. Assuming that $\omega_{A-1,Z} \approx \omega_{A-1,Z-1} \approx \omega_{A,Z}$ with logarithmic accuracy, we obtain $\omega_{A,Z}^{\rm corr} \approx \omega_{A,Z}(1 - P_{\rm n} - P_{\rm p})$. Assuming then that $A \simeq 2Z$ is large enough and finding the logarithm of the latter expression by taking into account the smallness of $P_{\rm n}$ and $P_{\rm p}$ compared to unity yields

$$\ln\omega_{A,Z}^{\rm corr} - \ln\omega_{A,Z} \approx -\frac{3}{\pi^2}\frac{(aT)^{3/2}}{\sqrt{\pi A}}\left(e^{-\frac{S_{\rm n}}{T}} + e^{-\frac{S_{\rm p}}{T}}\right), \quad (15)$$

where we expressed the radius $R_{A,Z}$ in the formulas for $P_{\rm n,p}$ in terms of the standard definition of the parameter $a$ in the model of a Fermi gas. This expression closely matches the correction term in the paper by Tubbs and Koonin (1979) in the same approximation.

Since the corrected expression for the partition function depends not only on the temperature but also on the matter density and composition, it makes sense to study the continuum effect on the thermodynamic quantities of the matter on the $(T, \rho)$ plane. This is also justifiable, because even if this effect is large for a given nucleus, reaching several tens of percent for certain nuclei at high temperatures (recall that this is an upper limit), the equilibrium concentration of these nuclei could be negligible and could have no effect on the thermodynamics.

Our calculations indicate that the maximum change in the thermodynamic functions in the low-temperature range due to the subtraction of the continuum is a few fractions of a percent for the entire domain of the quantities $(T_9 \le 40, \rho, \theta)$ under consideration. Thus, we have shown that the model of a Fermi gas for calculating the nuclear partition functions in this domain is adequate, and that the possible corrections to it are small.

### *The High-Temperature Range* ($T_9 > 40$)

As the temperature rises, progressively higher excited levels of the nucleus, whose number, energies, and parameters are unknown, begin to contribute to the partition function. The model of a Fermi gas predicts an increase in the mean excitation energy as $\langle E\rangle \approx aT^2$, which is definitely erroneous at high temperatures. We proceed from an expression for the excitation energy that allows the satisfaction of the condition $\langle E\rangle \le Q_{A,Z}$ to be directly checked:

$$\langle E\rangle = Q_{A,Z}\,\vartheta(T), \quad 0 \le \vartheta(T) \le 1, \qquad (16)$$

where $\vartheta(T)$ is a dimensionless function of the temperature. Using the relation $\langle E\rangle = T\left(\frac{\partial \ln\omega}{\partial \ln T}\right)$, we obtain the corresponding expression for the nuclear partition function:

$$\ln\omega(T) = Q_{A,Z}\int \frac{\vartheta(T)}{T^2}dT \qquad (17)$$
$$= \text{const} - \frac{Q_{A,Z}}{T}\left(\mathcal{A} - \frac{\mathcal{B}}{2T} - \frac{\mathcal{C}}{3T^2}\right).$$

Here, we use the expression $\vartheta(T)=\mathcal{A}-\frac{\mathcal{B}}{T}-\frac{\mathcal{C}}{T^2}$ for the function $\vartheta(T)$, where $\mathcal{A} \le 1$ is a free parameter, and $\mathcal{B}, \mathcal{C}$, and the integration constant can be determined for each nuclide $(A, Z)$ from the continuity condition for the partition function and its first two derivatives at temperature $T_9 = 40$. The value of $\mathcal{A}$ gives the maximum fraction of the binding energy that can be stored in the form of excited-level energy. We found that the thermodynamic quantities are moderately sensitive to the specific value of $\mathcal{A}$ up to densities $\rho \sim 10^{12}$ g cm$^{-3}$, and that the difference between them for $\mathcal{A} = 0.5$ and 1 (for all nuclei) does not exceed two percent; in fact, it is much smaller almost everywhere. In our calculations, we used $\mathcal{A} = 0.8$.

### *Results of the Described Approach*

Results of the described approach are illustrated by Figs. 1 and 2. In Fig. 1, the thick solid line indicates the calculated logarithm of the partition function for $^{56}$Fe, and the thin solid line indicates its value that corresponds to the model of a Fermi gas. The thick and thin dashed lines indicate the corresponding mean excitation energies $\langle E\rangle$. We see that $\langle E\rangle$ calculated using the model of a Fermi gas becomes inadequate even at $T_9 \approx 100$, suggesting that the corresponding partition function is also inapplicable in this range.

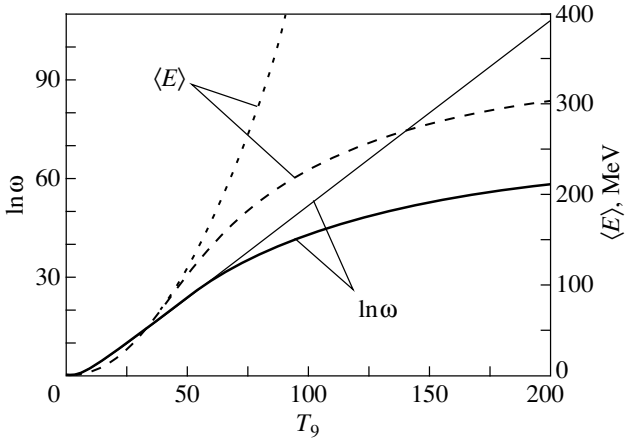


**Fig. 1.** Logarithm of the partition function (left scale) and mean excitation energy (right scale) for $^{56}$Fe versus temperature.

Figure 2 shows the curves for a set of nuclei that allows the range of the partition functions to be judged. We clearly see that the almost linear temperature dependence $\ln\omega \approx aT$, corresponding to the model of a Fermi gas, changes to a flatter dependence corresponding to our simple approximation. This approximation is in satisfactory agreement with the results of more complex approaches (see, e.g., Tubbs and Koonin 1979) and proves to be quite adequate for our purposes in view of the weak sensitivity of the thermodynamic quantities mentioned above.

## EQUILIBRIUM CONCENTRATIONS

We can get an idea of the calculated equilibrium concentrations from Figs. 3–9, in which the mass fractions $X_{A,Z} = AY_{A,Z}$ are plotted against $T$, $\rho$, and $\theta$. In general, at moderately high temperatures (before the onset of the intense dissociation of nuclides), the most abundant nuclides are those with individual neutron-to-proton ratios $(A - Z)/Z$ close to $\theta$. This natural result, which was pointed out by Clifford and Tayler (1965) long ago, is traceable in all these figures, particularly in Fig. 7 where the mass fraction is plotted against $\theta$ as an example.

An increase in the density causes the nuclide dissociation to be delayed with rising temperature (cf. Figs. 4 and 5). An increase in $\theta$ has no significant effect on the dissociation temperature, but contributes to the appearance of neutron-rich nuclides that

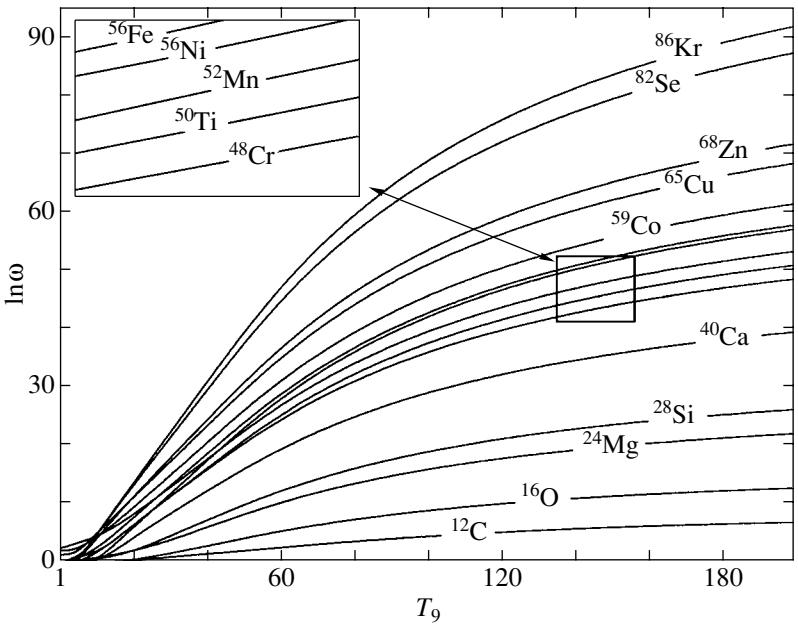


**Fig. 2.** Logarithms of the partition functions versus temperature for several selected nuclides.

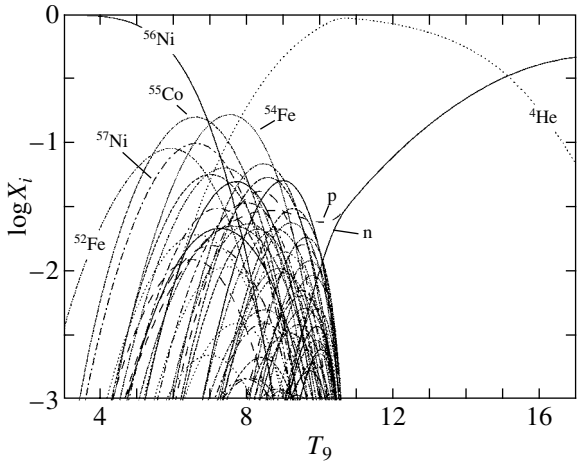


**Fig. 3.** Mass fractions versus temperature for $\rho = 10^9$ g cm$^{-3}$ and $\theta = 1$.

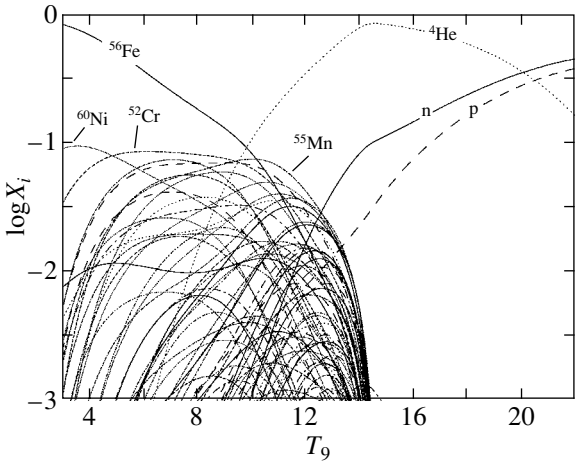


**Fig. 4.** Same as Fig. 3 for $\rho = 10^{10}$ g cm$^{-3}$ and $\theta = 30/26$.

are represented here by selenium isotopes, $^{84-89}$Se (Figs. 6, 7).

Free nucleons are of particular interest, because these play a leading role in the process of matter neutronization, which is accompanied by an increase in $\theta$ as the gravitational collapse develops. Figures 8 and 9 show the proton and neutron mass fractions, $X_\mathrm{p}$ and $X_\mathrm{n}$, for three densities. Including excited levels causes $X_\mathrm{n}$ to decrease, but has virtually no effect on $X_\mathrm{p}$. Figure 10 shows the curves on which the numbers of neutrons and protons ($Y_\mathrm{n}$ and $Y_\mathrm{p}$) are equal to the total number of all nuclides ($\Sigma Y_{A,Z}$); to the right of the corresponding curves, free nucleons dominate over nuclides by the number of particles.

## THERMODYNAMIC PROPERTIES

For the known concentrations of all nuclides, $Y_{A,Z}$, free neutrons, $Y_\mathrm{n}$, and protons, $Y_\mathrm{p}$, and for the given neutron and proton chemical potentials, $\psi_\mathrm{n,p}$, as functions of $(T, \rho, \theta)$, the total pressure $P$, specific energy $E$, and specific entropy $S$ can be determined

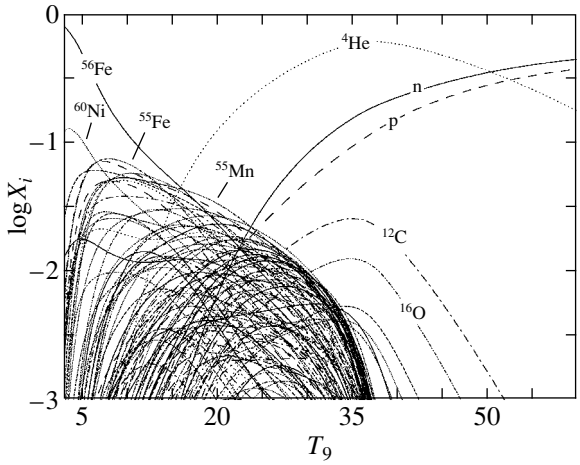


**Fig. 5.** Same as Fig. 4 for $\rho = 10^{12}$ g cm$^{-3}$.

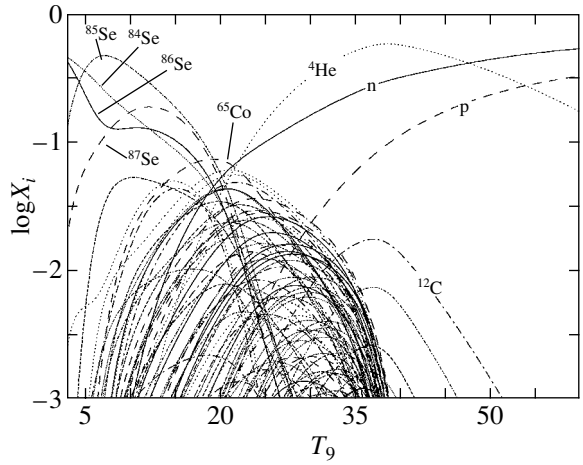


**Fig. 6.** Same as Fig. 3 for $\rho = 10^{12}$ g cm$^{-3}$ and $\theta = 1.5$.

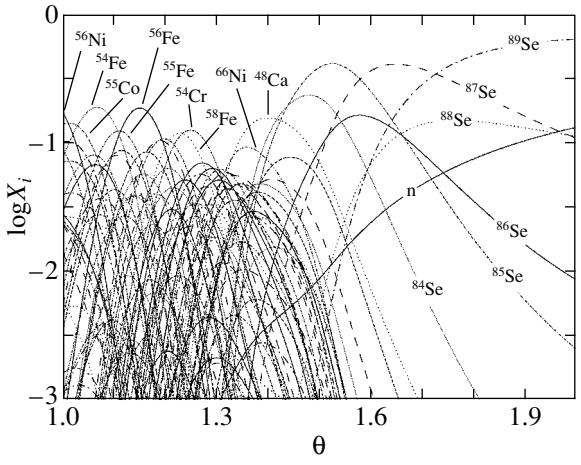


**Fig. 7.** Mass fractions versus $\theta$ at $T_9 = 8$ and $\rho = 10^{10}$ g cm$^{-3}$.

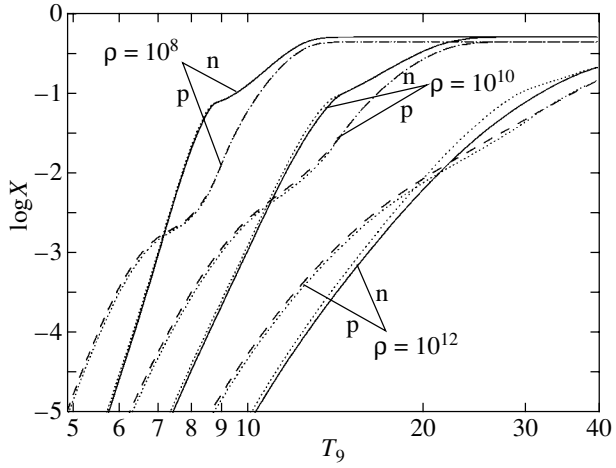


**Fig. 8.** Mass fractions of free nucleons versus temperature for selected densities and $\theta = 30/26$. The solid and dashed lines correspond to neutrons and protons, respectively. The dotted line indicates the case without excited states.

using the relations

$$P = \left\{ \frac{k}{m_\mathrm{u}} \rho T \sum_{A,Z} Y_{A,Z} \right\} + P_\mathrm{n} + P_\mathrm{p} + P_\mathrm{e} + \frac{1}{3} a T^4, \tag{18}$$

$$E = \frac{k}{m_\mathrm{u}} T \left\{ \sum_{A,Z} \left[ \frac{3}{2} - \frac{Q_{A,Z}}{kT} + T \frac{\omega'_{A,Z}}{\omega_{A,Z}} \right] Y_{A,Z} \right. \tag{19}$$

$$\left. + \frac{m_\mathrm{u} c^2}{kT} \frac{\Delta_\mathrm{e} + \Delta_\mathrm{p} + \theta \Delta_\mathrm{n}}{1+\theta} \right\} + E_\mathrm{n} + E_\mathrm{p} + E_\mathrm{e} + \frac{a T^4}{\rho},$$

$$S = \frac{k}{m_\mathrm{u}} \left\{ \sum_{A,Z} \left( \frac{5}{2} - \frac{Q_{A,Z}}{kT} + T \frac{\omega'_{A,Z}}{\omega_{A,Z}} \right) Y_{A,Z} \right. \tag{20}$$

$$\left. + \psi_\mathrm{n} Y_\mathrm{n} + \psi_\mathrm{p} Y_\mathrm{p} - \frac{\theta \psi_\mathrm{n} + \psi_\mathrm{p}}{1+\theta} \right\}$$

$$+ S_\mathrm{n} + S_\mathrm{p} + S_\mathrm{e} + \frac{4}{3} \frac{a T^3}{\rho}.$$

The first terms given in braces in these relations describe the contribution from all nuclides $(A, Z)$, while the last terms describe the contribution from blackbody radiation (here, in contrast to the section entitled The Inclusion of Excited Levels, $a$ is the radiation density constant). The following notation is used in the expression for $E$:

$$\Delta_\mathrm{e} = \frac{m_\mathrm{e}}{m_\mathrm{u}} = 5.4857990 \times 10^{-4}, \tag{21}$$

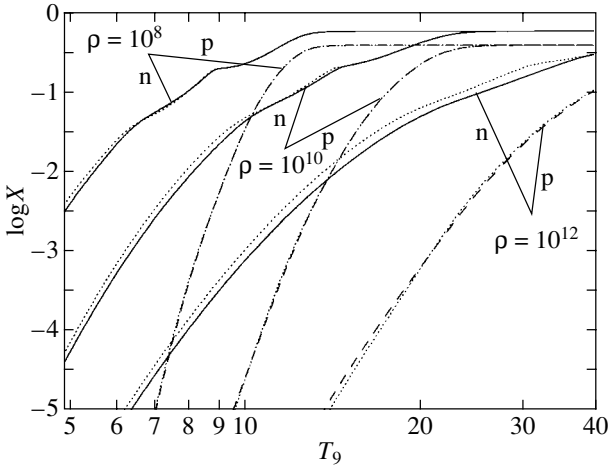


**Fig. 9.** Same as Fig. 8 for $\theta = 1.5$.

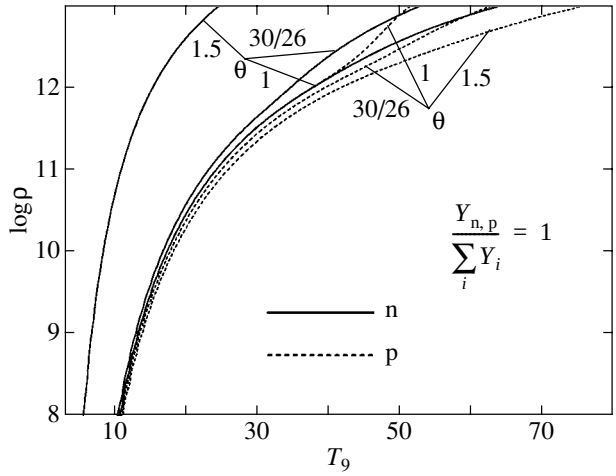


**Fig. 10.** Lines on which the number of free nucleons is equal to the total number of heavier nuclides for $\theta = 1, 30/26$, and 1.5. The solid and dashed lines pertain to free neutrons and protons, respectively.

$$\Delta_{\rm p} = \frac{m_{\rm p}}{m_{\rm u}} - 1 = 7.2764875 \times 10^{-3},$$
$$\Delta_{\rm n} = \frac{m_{\rm n}}{m_{\rm n}} - 1 = 8.6648933 \times 10^{-3}.$$

These are related to the additional terms that describe the rest energies of the atomic electrons (the term with $\Delta_{\rm e}$), free protons ($\Delta_{\rm p}$) and neutrons ($\Delta_{\rm n}$). The contributions from the electron–positron component ($P_{\rm e}$, $E_{\rm e}$, $S_{\rm e}$) can be calculated by means of the EPEOS code (Blinnikov *et al.* 1996), which uses the complete Fermi–Dirac statistics.

The pressure, specific kinetic energy, and entropy of partially degenerate free neutrons and protons can be calculated using the following formulas (Blinnikov *et al.* 1996):

$$P_i = \frac{2}{3}\frac{m_i c^2}{\lambda_i^3}\frac{\sqrt{2}}{\alpha_i^{5/2}} \times \left[F_{3/2}(\psi_i) + \frac{3}{4\alpha_i}F_{5/2}(\psi_i) + \frac{3}{32\alpha_i^2}F_{7/2}(\psi_i)\right],$$

$$E_i = \frac{m_i c^2}{\lambda_i^3 \rho}\frac{\sqrt{2}}{\alpha_i^{5/2}} \times \left[F_{3/2}(\psi_i) + \frac{5}{4\alpha_i}F_{5/2}(\psi_i) + \frac{7}{32\alpha_i^2}F_{7/2}(\psi_i)\right], \quad (22)$$

$$S_i = \frac{5}{3}\frac{k}{\lambda_i^3 \rho}\frac{\sqrt{2}}{\alpha_i^{3/2}}\left\{F_{3/2}(\psi_i) - \frac{3}{5}\psi_i F_{1/2}(\psi_i) + \frac{21}{20\alpha_i}\left[F_{5/2}(\psi_i) - \frac{5}{7}\psi_i F_{3/2}(\psi_i)\right] + \frac{27}{160\alpha_i^2}\left[F_{7/2}(\psi_i) - \frac{7}{9}\psi_i F_{5/2}(\psi_i)\right]\right\},$$

where $i = {\rm n}$ for neutrons and $i = {\rm p}$ for protons. To calculate the half-integer Fermi–Dirac functions in Eqs. (5) and (22), we used approximation formulas from the EPEOS package that were based on spline interpolation at intermediate values of the argument with a relative error of no more than $10^{-4}$. At large negative and positive values of the argument, the interpolation smoothly transforms into the corresponding asymptotic expansions. Equations (4)–(7) and (18)–(22) allow us to calculate the thermodynamic quantities as functions of $T$, $\rho$, and $\theta$ and their derivatives with respect to $T$, $\rho$, and $\theta$. Here, we do not give the fairly cumbersome analytical expressions for these derivatives. These can be expressed in terms of the equilibrium nuclide concentrations and the nucleon chemical potentials ($\psi_{\rm n}$ and $\psi_{\rm p}$) by differentiating the above equations. Figure 11 demonstrates a typical dependence of $\psi_{\rm n,p}$ on $T$ and $\rho$. We see that $\psi_{\rm n}$ and $\psi_{\rm p}$ remain negative over the wide $T$ and $\rho$ ranges characteristic of the initial stages of gravitational collapse. As a result, the free-nucleon degeneracy effects prove to be virtually insignificant: these begin to contribute to the equation of state only at $T_9 \gtrsim 100$ and $\rho \gtrsim 10^{13}$ g cm$^{-3}$, since $\psi_{\rm n,p} \gtrsim -2$. At low temperatures, the free nucleons remain nondegenerate up to the subnuclear densities due to their low concentrations, because almost all of the neutrons and protons prove to be packed in atomic nuclei.

The reduced electron chemical potential $\psi_{\rm e}$ calculated by the EPEOS code is shown in Fig. 12. It depends only on two variables, $T$ and $\rho Y_{\rm e}$, where $Y_{\rm e} \equiv 1/(1+\theta)$. In the ranges $T_9 \approx 10$–$100$ and $\rho \approx 10^{10}$–$10^{13}$ g cm$^{-3}$ of greatest interest for the initial

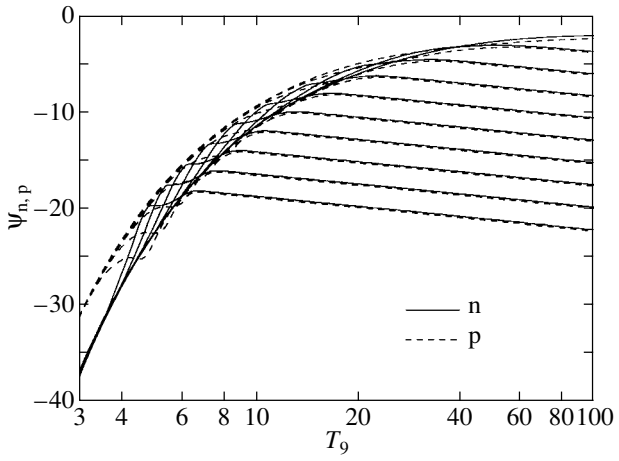


**Fig. 11.** Reduced neutron and proton chemical potentials versus temperature for $\theta = 30/26$ at densities that decrease by an order of magnitude when going from each overlying curve to the underlying curve. The uppermost and lowermost curves for neutrons (solid lines) and protons (dashed lines) pertain to $\rho = 10^{13}$ g cm$^{-3}$ and $\rho = 10^4$ g cm$^{-3}$, respectively.

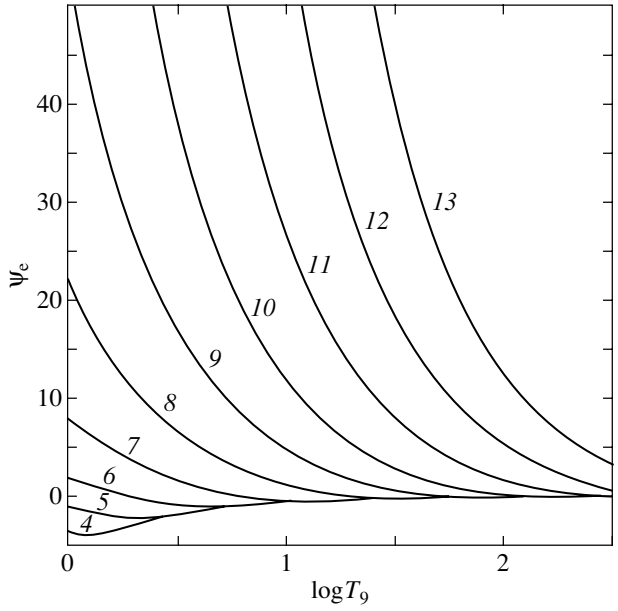


**Fig. 12.** Reduced electron chemical potential $\psi_e$ versus temperature at various values of $\log \rho Y_e$ (the numbers near the curves).

stage of collapse, $\psi_e \approx 10$–$40$ and the electron chemical potential $\mu_e = m_e c^2 + kT\psi_e$ proves to be high enough, 10–100 MeV, for nonequilibrium neutronization of stellar matter to develop.

The dependence of the equation of state on the third variable $\theta$ implies that we are dealing with a system with a variable number of particles. Under NSE conditions, the first law of thermodynamics can be written as (see also Imshennik and Chechetkin 1970)

$$dE + PdV = TdS + \Psi dY_l, \qquad V = \frac{1}{\rho}, \qquad (23)$$

where $Y_l$ is the lepton charge per nucleon. In the absence of neutrinos (our case), $Y_l = Y_e = 1/(1+\theta)$. The quantity $\Psi$ is defined as

$$\Psi = -\frac{1}{m_u}\left(\mu_n - \mu_p - \mu_e\right) \qquad (24)$$
$$= -\frac{k}{m_u}T\left(\psi_n - \psi_p - \psi_e + \frac{Q_n}{kT}\right).$$

Here, $Q_n = c^2(m_n - m_p - m_e) = 0.78235$ MeV.

During neutronization, $\theta$ increases and $dY_l < 0$. Therefore, in an adiabatic process ($dE + PdV = 0$), the positive sign of $\Psi$ implies an increase in entropy with $\theta$, while the negative sign is indicative of its decrease. Since part of the energy during neutronization is carried away by neutrinos, the positivity of $\Psi$ is only a necessary but not sufficient condition for the increase in entropy. Figure 13 shows the dimensionless quantity

$$\Phi = \frac{m_u}{kT}\Psi = -\left(\psi_n - \psi_p - \psi_e + \frac{Q_n}{kT}\right).$$

The horizontal dotted line separates the domains of positive and negative $\Phi$.

The most important quantity for the theory of gravitational collapse, the adiabatic index $\gamma$, is defined as

$$\gamma = \left(\frac{\partial \log P}{\partial \log \rho}\right)_{S,\theta} = \frac{\rho}{P}\left[\left(\frac{\partial P}{\partial \rho}\right)_{T,\theta} + \frac{T}{\rho^2}\frac{\left(\frac{\partial P}{\partial T}\right)^2_{\rho,\theta}}{\left(\frac{\partial E}{\partial T}\right)_{\rho,\theta}}\right]. \qquad (25)$$

Figures 14a–14c show lines of constant $\gamma$ on the $(T, \rho)$ plane at three values of $\theta = 1, 30/26, 1.5$ characteristic of the initial stage of collapse. Each figure is a superposition of two sets of lines of constant $\gamma$ calculated with (solid lines) and without (dashed lines) excited states. At low densities ($\rho \lesssim 10^9$ g cm$^{-3}$), both sets of lines virtually merge together, suggesting that $\gamma$ is weakly sensitive to the nuclide excitation parameters. However, at densities $\rho \gtrsim 10^{10}$ g cm$^{-3}$, the excitation of nuclides causes mainly a reduction in $\gamma$, which is accompanied by an expansion of the instability ravine, the region inside which $\gamma < 4/3$. The boundaries of this region are specified by the lines on which $\gamma$ is exactly equal to 4/3—the heavy solid and dashed lines in Fig. 14. A characteristic feature of the function $\gamma(T, \rho, \theta)$ is the existence of two deep minima that are clearly seen in Fig. 14 and lie at $T$ and $\rho$ and change only slightly from figure to figure. One of the minima $\gamma_{min} \approx 1.07, 0.94, 0.92$ (Figs. 14a, 14b, and 14c, respectively) at $\rho \approx 2 \times 10^7$ g cm$^{-3}$ (for all three figures) and $T_9 = 6.3, 7.5, 7.6$ (Figs. 14a, 14b,

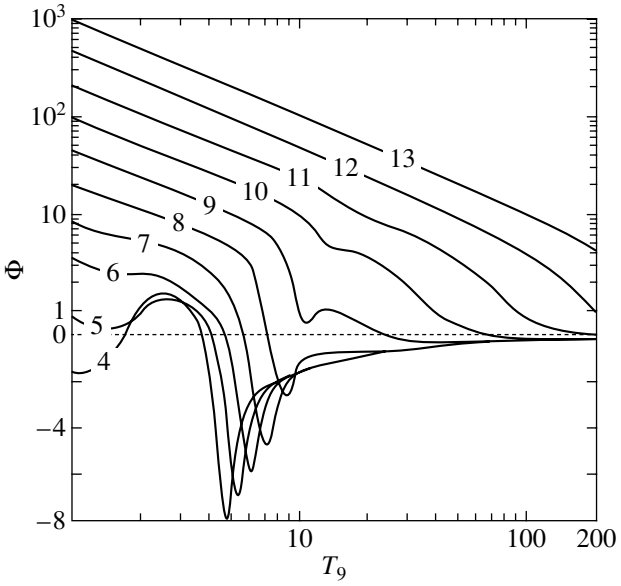


**Fig. 13.** Quantity $\Phi = \frac{m_u}{kT}\Psi$ versus temperature at $\theta = 30/26$ and various densities ($\log\rho$ is marked by numbers near the curves). The lower ($\Phi \le 1$) and upper ($\Phi > 1$) parts of the vertical axis are given on linear and logarithmic scales, respectively.

and 14c, respectively) results from the dissociation of nuclides into $\alpha$ particles and free nucleons in the presence of electron–positron pairs, while the other minimum $\gamma_{\min} \approx 1.04$–$1.05$ at $\rho \approx (5$–$6) \times 10^7$ g cm$^{-3}$ and $T_9 \approx 10.5$–$10.6$ arises from the dissociation of $\alpha$ particles into free nucleons under the same conditions (Imshennik and Nadyozhin 1965).

At low and high densities, $\gamma$ becomes less than 4/3 due to the appearance of electron–positron pairs and the dissociation of nuclides into $\alpha$ particles and free nucleons, respectively. For $\theta = 1$ (Fig. 14a), $\gamma < 4/3$ is a simply connected domain: one of the above effects smoothly replaces the other. However, for $\theta = 30/26$, a low ($\gamma - 4/3 \approx 0.002$) neck that separates the instability ravine into two parts arises at $3 \lesssim T_9 \lesssim 4$ (Fig. 14b). This is because the most abundant nuclide at such temperatures is $^{56}$Ni for $\theta = 1$ and $^{56}$Fe for $\theta = 30/26$; the binding energy of the latter nuclide is higher by 8.4 MeV. As a result, the $^{56}$Fe dissociation begins at a higher temperature than does the $^{56}$Ni dissociation, and the overlap between the above two factors of the reduction in $\gamma$ proves to be insufficient. At $\theta$ that are appreciably larger than 30/26, the instability ravine again becomes simply connected (Fig. 14c). The reason is the same: the most abundant nuclides are those with lower binding energies per nucleon than that for $^{56}$Fe.

In Fig. 15, the dimensionless entropy per nucleon ($S_b = \frac{m_u}{k}S$) is plotted against $T$ at fixed $\rho$.

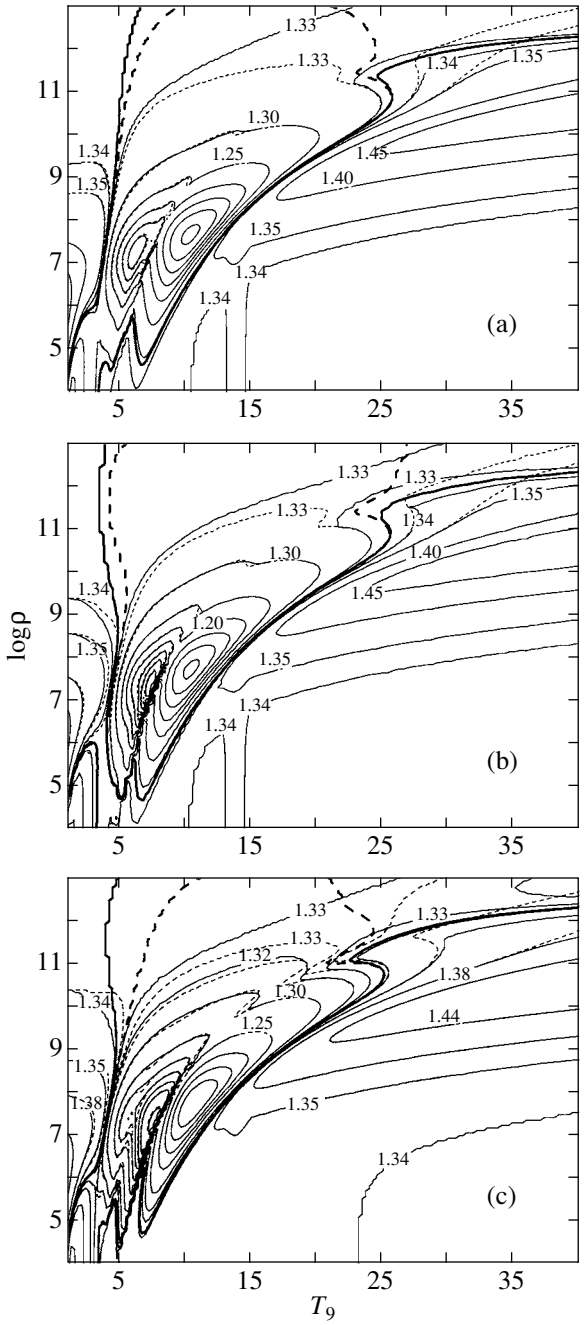


**Fig. 14.** Levels of constant $\gamma$ with (solid lines) and without (dashed lines) excited states for (a) $\theta = 1$, (b) $\theta = 30/26$, and (c) $\theta = 1.5$. The 1.33 level corresponds to the exact value of $\gamma = 1.33 < 4/3$. Levels of constant $\gamma$ for $\gamma \le 1.30$ are indicated at steps $\Delta j = 0.05$.

We see that the influence of nuclide excitation on the entropy becomes noticeable only at densities $\rho \gtrsim 10^{10}$ g cm$^{-3}$. Multiple excitation of nuclear levels increases the contribution of each individual nuclide ($\omega' > 0$ in formula (20)) to the total entropy. However, at fixed temperature and density, the degree of nuclide dissociation into free nucleons decreases, which leads

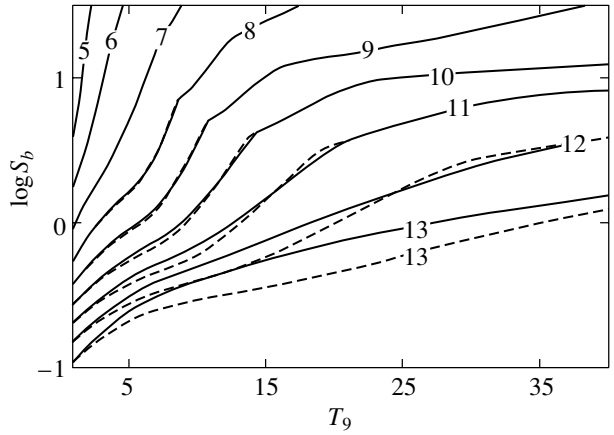


**Fig. 15.** Dimensionless entropy versus $T$ at various $\rho$ for $\theta = 30/26$ without (dashed lines) and with (solid lines) excited levels. The numbers near the curves give the values of $\log \rho$.

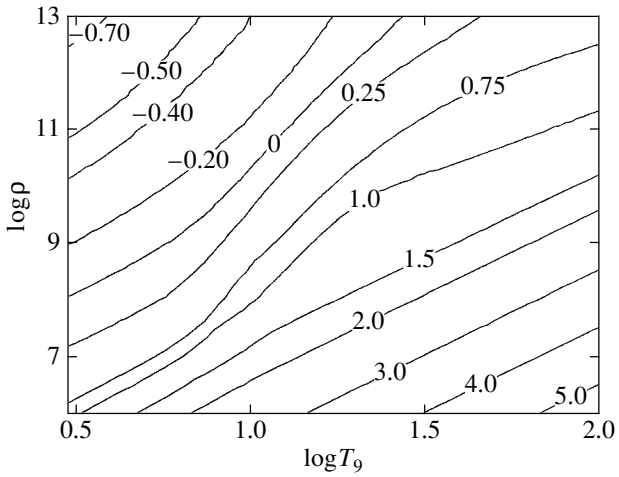


**Fig. 16.** Lines of constant entropy ($\log S_b$) on the $(T, \rho)$ plane at constant $\theta = 30/26$.

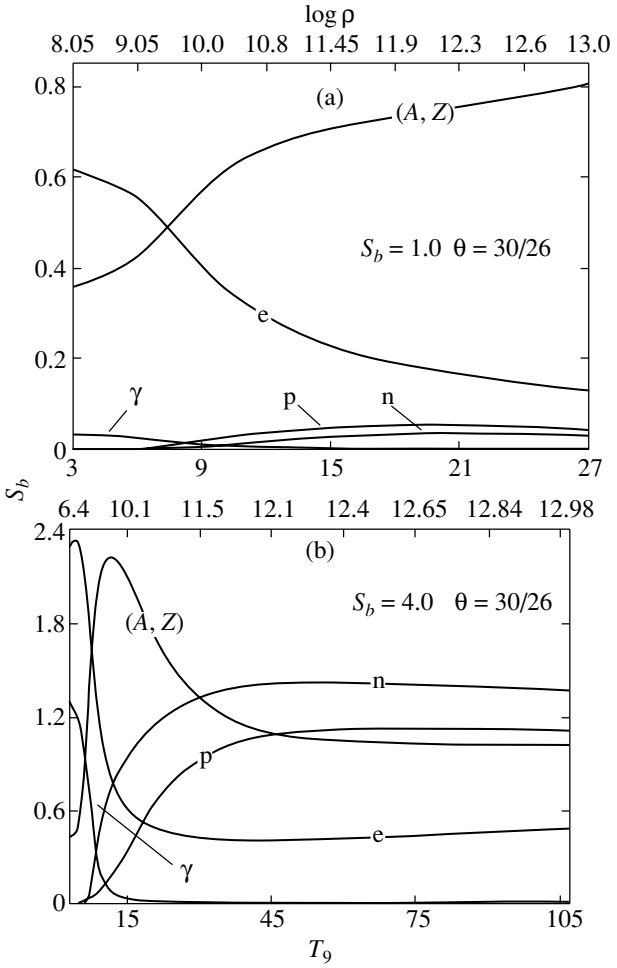


**Fig. 17.** Contributions from all nuclides $(A, Z)$, the electron–positron component e, free neutrons n, free protons p, and blackbody radiation $\gamma$ to the total entropy $S_b = 1$ (a) and 4 (b) as functions of the temperature or the density that closely corresponds to it at a fixed entropy.

to the opposite effect: a decrease in the contribution of the latter to the total entropy. As a result, the excitation of nuclides can be accompanied by both an increase and a decrease in the total entropy.

Figure 16 shows lines of constant entropy on the $(T, S)$ plane. In the absence of neutrino energy losses and neutronization processes, each element of stellar matter would collapse along the isentrope determined by its entropy at the onset of collapse. Figures 17a and 17b illustrate the contribution of the various components along the $S_b = 1$ and $S_b = 4$ isentropes, respectively, to the total entropy. At temperatures $T_9 \lesssim 8$, the electron–positron component makes the largest contribution to the entropy. At higher temperatures, the total contribution of the nuclides $(A, Z)$ dominates until these begin to dissociate into free nucleons, which become the main entropy suppliers (Fig. 17b).

## CONCLUSIONS

The main result of this work is that the excitation of numerous levels of atomic nuclei leads to appreciable (albeit noncritical) corrections to the equation of state only at densities $\rho \gtrsim 10^{10}$ g cm$^{-3}$. In particular, this effect contributes to the expansion of the domain $\gamma < 4/3$ on the $(T, \rho)$ plane (Fig. 14). Our suggested simple fit for the level density at high temperatures ($T_9 > 40$, Eq. (17)) seems quite adequate for their influence on the equation of state to be taken into account.

For the densities under consideration ($\rho < 10^{13}$ g cm$^{-3}$), the Fermi degeneracy of free nucleons

proves to be insignificant, because their concentrations are low. At low temperatures, almost all of the nucleons are packed in atomic nuclei.

In our next paper, we plan to investigate the influence of Coulomb interactions and neutron-rich nuclei that appear at low entropy on the equation of state. The ultimate goal of the entire study is to compile three-parameter tables supplied with a smooth interpolation procedure that could serve as an efficient tool in calculating gravitational collapse with allowance made for the matter neutronization kinetics.

## ACKNOWLEDGMENTS

This work was supported by the Russian Foundation for Basic Research (project no. 04-02-16840a).

## REFERENCES

1. E. M. Burbidge, G. K. Burbidge, W. A. Fowler, and F. Hoyle, Rev. Mod. Phys. **29**, 547 (1957).
2. S. I. Blinnikov, N. V. Dunina-Barkovskaya, and D. K. Nadyozhin, Astrophys. J. Suppl. **106**, 171 (1996).
3. S. Y. Chu, H. Nordberg, R. B. Firestone, and L. P. Ekstrom, *Isotope Explorer* (1999); http://ie.lbl.gov/toi.html.
4. F. E. Clifford and R. J. Tayler, Mem. R. Astron. Soc. **69**, 21 (1965).
5. M. F. El Eid and W. Hillebrandt, Astron. Astrophys. Suppl. **42**, 215 (1980).
6. W. A. Fowler, C. A. Engelbrecht, and S. E. Woosley, Astrophys. J. **226**, 984 (1978).
7. F. Hoyle, Mon. Not. R. Astron. Soc. **106**, 343 (1946).
8. F. Hoyle and W. A. Fowler, Astrophys. J. **132**, 565 (1960).
9. V. S. Imshennik and D. K. Nadyozhin, Astron. Zh. **42**, 1154 (1965) [Sov. Astron. **9**, 815 (1965)].
10. V. S. Imshennik and V. M. Chechetkin, Astron. Zh. **47**, 929 (1970) [Sov. Astron. **14**, 747 (1970)].
11. T. J. Mazurek, J. M. Lattimer, and G. E. Brown, Astrophys. J. **229**, 713 (1979).
12. M. J. Murphy, Astrophys. J. Suppl. **42**, 385 (1980).
13. B. Potet, J. Duflo, and G. Audi, in *Proceedings of the International Conference on Exotic Nuclei and Atomic Masses ENAM-95,* Ed. by M. de Saint-Simon and O. Sorlin (Frontieres, Arles, 1995), p. 151.
14. T. Rauscher, F.-K. Thielemann, and K.-L. Kratz, Phys. Rev. C **56**, 163 (1997).
15. D. L. Tubbs and S. E. Koonin, Astrophys. J. **232**, L59 (1979).

*Translated by V. Astakhov*

*Astronomy Letters, Vol. 30, No. 9, 2004, pp. 647–655. Translated from Pis'ma v Astronomicheskiĭ Zhurnal, Vol. 30, No. 9, 2004, pp. 711–720.*


# Fission and the *r*-Process: Competition between Neutron-Induced and Beta-Delayed Fission

**I. V. Panov[1]* and F.-K. Thielemann[2]**

[1]*Institute for Theoretical and Experimental Physics, ul. Bol'shaya Cheremushkinskaya 25, Moscow, 117259 Russia*

[2]*University of Basel, Klingelbergstr. 82, CH-4056, Basel, Switzerland*

Received January 19, 2004

**Abstract**—We show that for the discussed scenario of a neutron-star merger in highly neutronized ejecta ($Y_e \sim 0.1$), neutron-induced fission plays a major role in the $r$-process cycling and is the main obstacle to the formation of superheavy elements. At the final stage of the $r$-process, when the free-neutron density is already too low to maintain rapid nucleosynthesis and only beta-decay and beta-delayed fission take place, the leading role in forming the final abundances of chemical elements passes to delayed fission. The latter ultimately changes the abundances of individual isotopes in the region before the second peak and heavier than lead, which, in particular, affects the determination of the age of the Galaxy.


Key words: *nuclear astrophysics, nucleosynthesis, r-process; supernovae and supernova remnants.*

## INTRODUCTION

One of the most important problems in studying the $r$-process is revealing the physical processes that lead to the termination of nucleosynthesis. What is mainly responsible for the termination of nucleosynthesis: a decrease in the free-neutron density to values at which the $r$-process terminates, or some other significant change in physical conditions (e.g., a drop in the matter density), or fission that prevents the $r$-process from overcoming the region of actinides? In addition, it is important to estimate the sensitivity of the computational results to the accuracy of the nuclear data used and to determine the degree of their reliability. We emphasize that although the mass distribution of the fission-product nuclei of long-lived nuclei has been adequately studied experimentally, the pattern of the mass distribution of the fission fragments of short-lived neutron-rich actinides is unknown. Therefore, studying the influence of various shapes of the mass distribution on astrophysical results (Panov *et al.* 2000) can also be helpful in understanding the fission of an atomic nucleus.

Previous $r$-process calculations (except for the calculations by Goriely and Clerbaux 1999) considered only beta-delayed fission whose rates were calculated by Thielemann *et al.* (1983) for the entire region of fissionable nuclei. In this paper, we also used for the first time the rate of beta-delayed fission calculated by Staudt and Klapdor-Kleingrothaus (1992) on the basis of the microscopic QRPA model. We were apparently the first to use these data to simulate the $r$-process and to analyze the dependence of the calculated abundances of heavy elements, particularly for masses $A \leq 130$ and $A \geq 196$, on the sets of beta-delayed fission rates used.

Can the isotopes of chemical elements with such masses be produced through the fission of actinides in the $r$-process during a merger of neutron stars? On the other hand, can observational data be helpful in determining what fission-rate calculations reproduce the physics of this process more faithfully? To answer these questions, we simulated the $r$-process not only by using various calculations of the beta-delayed fission rates (Thielemann *et al.* 1983; Staudt and Klapdor-Kleingrothaus 1992), but also by taking into account neutron-induced fission and various shapes of the mass distribution of the fission-product nuclei.

## THE SYSTEM OF EQUATIONS AND NUCLEAR DATA

For our numerical $r$-process calculations both in the schematic model and in the neutron-star merger (NSM) scenario, we used the previously developed kinetic network incorporated into the SYNTEZ code (Blinnikov and Panov 1996; Nadyozhin *et al.* 1998;

*E-mail: Igor.Panov@itep.ru

Panov and Nadyozhin 1999) that specifies the densities of all the nuclei involved in nucleosynthesis, including a check of the neutron density.

Our mathematical model was used for nucleosynthesis calculations in various scenarios and was tested by calculations based on other codes (Panov *et al.* 2001a). The total number of equations considered in our calculations was 3100. All the possible isotopes from calcium ($Z = 20$) to einsteinium ($Z = 99$) were included in the system of equations. The nucleon stability boundaries were determined from the binding energies calculated by Hilf *et al.* (1976).

Let us consider the implications of the restrictions of the nucleosynthesis region that lead to the inclusion of only some of the fissionable isotopes in our calculations and the choice of various possible models for the mass distributions of the fission-product nuclei. The ways of introducing fission into the scheme of nucleosynthesis calculations can be divided into two groups:

(1) As we mentioned above, fission is most commonly introduced as a tool that terminates the advancement of the nucleosynthesis wave into the region of heavier nuclei and ensures the $r$-process cycling from the region of fissionable nuclei into the region of masses with $A \approx 110$–$140$. Therefore, the fission models of this group are very simple: 100% spontaneous fission is commonly assumed when nuclei with ($A_\mathrm{f}$, $Z_\mathrm{f}$) or, even more simply, $A_\mathrm{f}$ are reached (as, e.g., in the paper by Freiburghaus *et al.* (1999b), where $A_\mathrm{f} = 240$).

(2) The principal mechanism is beta-delayed fission that prevents the penetration of the nucleosynthesis wave through the region of nuclei with a delayed-fission probability close to 100% (Thielemann *et al.* 1983). If the $r$-process overcomes the region of beta-delayed fission to produce heavier nuclei at $P_{\beta\mathrm{df}} < 100\%$, then these can decay through the alpha channel or undergo spontaneous fission.

We included fission in our nucleosynthesis calculations by taking into account various channels, primarily beta-delayed and neutron-induced fission. These two fission channels virtually terminate the advancement of the nucleosynthesis wave in the region of chemical elements with $Z \approx 90$–$96$, at least for the fission barriers of Howard and Möller (1980). The influence of restrictions of the fission region on the final results will be shown below.

We used the radiative neutron capture rates from the calculations by Cowan *et al.* (1991) and Rauscher and Thielemann (2000). The nuclear masses were determined using the FRDM model (Kratz *et al.* 1993).

The change in the concentration of each actinide was determined by taking into account the reactions with neutrons, beta decay, and various fission channels:

$$
\begin{aligned}
dY_{A,Z}/dt = &-\lambda_{n\gamma}(A,Z)Y_{A,Z} \\
&+ \lambda_{n\gamma}(A-1,Z)Y_{A-1,Z} - \lambda_{\gamma n}(A,Z)Y_{A,Z} \\
&+ \lambda_{\gamma n}(A+1,Z)Y_{A+1,Z} + \lambda_{\nu e}(A,Z-1)Y_{A,Z-1} \\
&- \lambda_{\nu e}(A,Z)Y_{A,Z} - \lambda_{\beta}(A,Z)Y_{A,Z} \\
&- \lambda_{\mathrm{nf}}(A,Z)Y_{A,Z} - \lambda_{\mathrm{sf}}(A,99)Y_{A,99} \\
&+ \sum_{k=0,1,2,3} \lambda_{\beta}(A+k,Z-1)P_k(A+k,Z-1) \\
&\times Y_{A+k,Z-1} + \sum_{A_\mathrm{f},Z_\mathrm{f}} W_{\beta}(A_\mathrm{f},Z_\mathrm{f},A,Z) \\
&\times \lambda_{\beta}(A_\mathrm{f},Z_\mathrm{f})P_{\beta\mathrm{df}}(A_\mathrm{f},Z_\mathrm{f})Y_{A_\mathrm{f},Z_\mathrm{f}} \\
&+ \sum_{A_\mathrm{f},Z_\mathrm{f}} W_{\mathrm{nf}}(A_\mathrm{f},Z_\mathrm{f},A,Z)\lambda_{\mathrm{nf}}(A_\mathrm{f},Z_\mathrm{f})Y_{A_\mathrm{f},Z_\mathrm{f}} \\
&+ \sum_{A_\mathrm{f}} W_{\mathrm{sf}}(A_\mathrm{f},99,A,Z)\lambda_{\mathrm{sf}}(A_\mathrm{f},Z_{99})Y_{A_\mathrm{f},Z_{99}}.
\end{aligned}
\tag{1}
$$

Here, $\lambda_i$ are the reaction rates; $P_{\beta\mathrm{df}}(A_\mathrm{f},Z_\mathrm{f})$ is the beta-delayed-fission probability; $A_\mathrm{f}$ and $Z_\mathrm{f}$ are the mass and charge numbers of the fissionable nucleus, respectively; and the weighting function of the fission products $W_i(A_\mathrm{f},Z_\mathrm{f},A,Z)$ is defined as follows: $W_i(A_\mathrm{f},Z_\mathrm{f},A,Z) = \delta(A-A_\mathrm{L})\delta(Z-Z_\mathrm{L}) + \delta(A-A_\mathrm{H})\delta(Z-Z_\mathrm{L})$, where $i$ specifies the fission channel.

The beta-decay rates were calculated in the QRPA model (Kratz *et al.* 1993), and the data on beta-delayed (Thielemann *et al.* 1983; Staudt and Klapdor-Kleingrothaus 1992) and neutron-induced (Thielemann *et al.* 1989) fission were obtained using the fission barriers of Howard and Möller (1980). The rates of neutron-induced fission were calculated (Panov and Thielemann 2003a) on the basis of the same mass formulas that were used to calculate the beta-delayed-fission and neutron-capture rates (Thielemann *et al.* 1987) and the fission barriers of Howard and Möller (1980). Our analysis of the sensitivity of the neutron-induced fission rates (Panov and Thielemann 2003a) showed that even if the fission barriers are significantly underestimated, the neutron-induced fission in certain $r$-process scenarios with a high free-neutron density will not decrease in importance, but will only affect such nucleosynthesis parameters as the cycle time and the yields of elements heavier than uranium. Therefore, our preliminary calculations of the formation of elements in the $r$-process performed with the fission barriers of Howard and Möller (1980) allowed us to reliably estimate the contributions of beta-delayed and neutron-induced fission on the $r$-process.

## NUCLEOSYNTHESIS CALCULATIONS AND DISCUSSION

To determine the influence of basic fission parameters on nucleosynthesis, we considered two $r$-process models. The first is a simple schematic $r$-process model that reproduces the main typical conditions of the $r$-process: $T_9 = 1$, the density of the medium where nucleosynthesis proceeds $\rho = 10^5$ g cm$^{-3}$, and the initial neutron-to-proton ratio $n/p$ that varied in different calculations over the range 2.5 to 8.3, which corresponded from 140 to 460 neutrons per seed nucleus. Iron nuclei with a mass number of 56 were chosen as the seed nuclei. With these initial conditions, we obtained a neutron flux that declined with time and a natural termination of the $r$-process as the free-neutron density decreased. Varying the initial $n/p$ ratio caused the duration of the $r$-process ($\tau_r$) to change from the minimum, when the fission wave had no time to reach the region of actinides and $\tau_r < \tau_{\text{f}}$ (where $\tau_{\text{f}}$ is the time it takes for the nucleosynthesis wave to reach the region of fissionable nuclei), to the maximum, where fission led to the $r$-process cycling and to a severalfold increase in the initial concentrations of heavy nuclei ($\tau_r \gg \tau_{\text{f}}$). Under these conditions, it was possible to assess the role of fission and to check the efficiency and significance of various parameters of the fission model included in our analysis. In this simple model, we analyzed the influence of a chosen mass distribution of the fission-product nuclei on the $r$-process.

Based on this model, which satisfactorily describes the observed abundances of heavy elements, we studied the influence of various mass distributions of the fission products on the final yields of the $r$-elements. However, the final calculations were performed for a specific evolutionary scenario in which the conditions for the $r$-process are realized (Rosswog *et al.* 1999). All of the necessary parameters, the neutron density and temperature profiles and the initial isotopic composition, were taken from the same model, as was the initial value of the model parameter $Y_e$ that determines the matter neutronization.

### *Dependence of the Concentrations of Heavy Elements on the Fission Rates at High Initial Matter Neutronization*

Under the conditions achievable not only during neutron-star mergers, but, for example, also during the destruction of low-mass supernovae (Panov and Chechetkin 2002) and, possibly, in other objects (for example, jets (Cameron 2001)), the excess of free neutrons is large enough for the $r$-process cycling and the involvement of secondary fission-product nuclei in nucleosynthesis to be possible. The entropy in the scenario under consideration is low ($\sim$1), and the electron density varies within the range $0.05 < Y_e < 0.18$. $Y_e$ was a model parameter, but the values under consideration are typical of the composition of the ejected part of the neutronized matter (see Freiburghaus *et al.* (1999b) and references therein).

Our calculations show the following: the computed abundance curves $Y(A)$ in the range $120 < A < 240$ are in good agreement with the observed solar system (ss) abundances and with one another even for rough fission models where the induced fission of isotopes with masses $A > A_{\text{f}}$ takes place. However, the values of $Y_A$ computed using different models of the fission-product mass distribution for isotopes $100 < A < 120$ and, naturally, $A > A_{\text{f}}$ (see Figs. 1 and 2 and the figures in Panov *et al.* (2001b)) differ greatly.

The final abundances $Y_A$ derived for two different fission-product mass distributions, M1 (Seeger *et al.* 1965; Lyutostanskii *et al.* 1988) and M2 (Itkis *et al.* 1989) (formula (3) in Panov and Thielemann 2003a), and various beta-delayed fission rates are shown in Figs. 1 and 2.

Figure 1 shows excellent agreement (given the parameter $Y_e$) with the observed ss abundances of heavy elements for masses $120 < A < 240$. The computed concentrations $Y_A$ at smaller mass numbers are much lower than their observed values and depend on the nuclear data and the fission-product mass distribution.

The beta-delayed and neutron-induced fission processes increase the cycling rate, slow down the advancement of the nucleosynthesis wave into the region of heavier actinides through fission, and lead to the involvement of secondary fission-product nuclei in the $r$-process. We clearly see from Fig. 1 that due to the higher beta-delayed fission probabilities in the path of the $r$-process at high free-neutron densities, $n_n > 10^{24}$ cm$^{-3}$, for the data of Staudt and Klapdor-Kleingrothaus (1992), fission actively begins for smaller $Z$ and $A$. Therefore, fission products with masses less than 90 and numbers $Z < 40$ are formed through fission, and the cycle time is longer than the cycle time obtained using $P_{\beta\text{df}}$ from Thielemann *et al.* (1983), which leads to the fundamental difference between the final concentrations.

The main difference between the currently available calculations of the beta-delayed fission probabilities by Thielemann *et al.* (1983) and Staudt and Klapdor-Kleingrothaus (1992) was (as has already been discussed previously (Panov and Thielemann 2003a)) the larger $P_{\beta\text{df}}$ for smaller masses of most chemical elements in the data of Thielemann *et al.* (1983), compared to the calculations of Staudt and Klapdor-Kleingrothaus (1992).

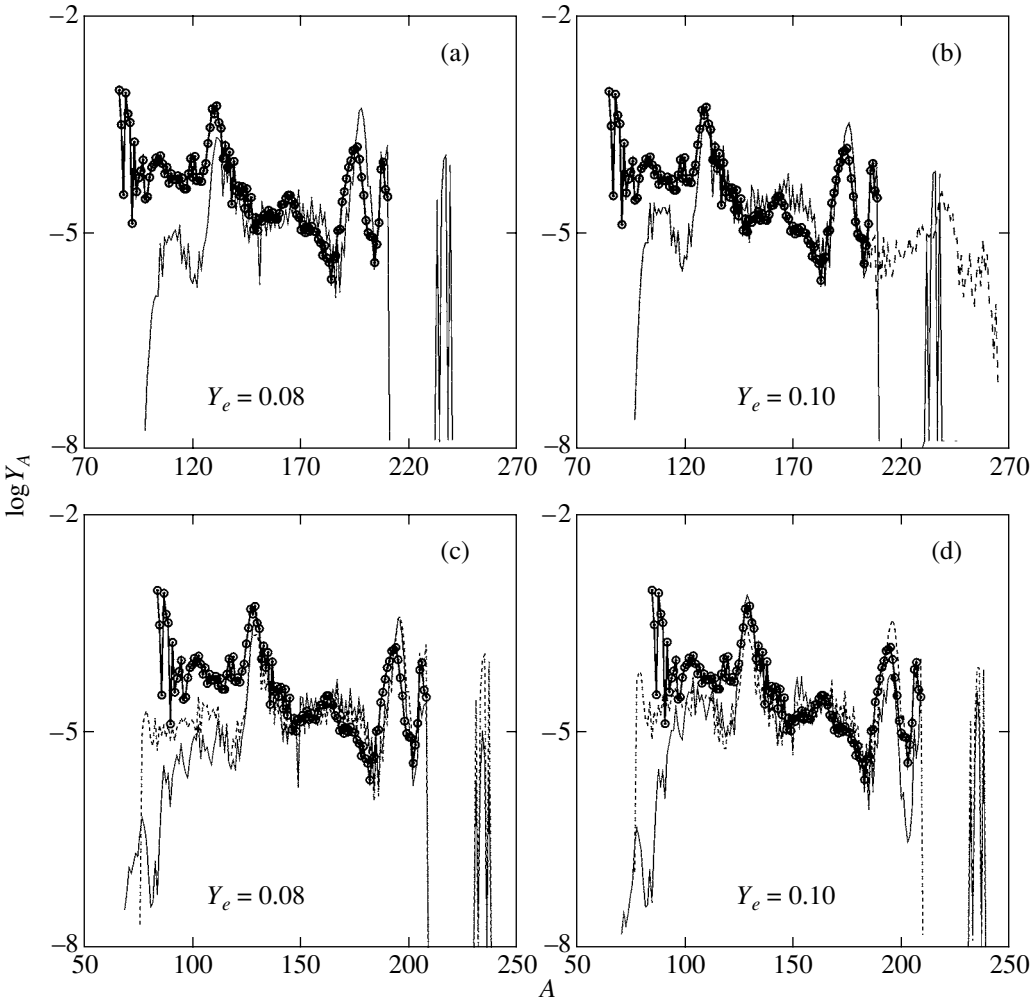


**Fig. 1.** Dependence of the isotope abundance $Y(A)$ on the initial values of $Y_e$, the model of the fission-product mass distribution, and the fission rates. (a), (b) are the model M1 of the fission-product mass distribution. The calculations were performed with (solid line) and without (dashed line) $\alpha$ decays. (c), (d) model M2 of the fission-product mass distribution. The calculations were performed with the fission probabilities as determined by Thielemann *et al.* (1983) (solid line) and Staudt and Klapdor-Kleingrothaus (1992) (dashed line). The solar elemental abundances (Anders and Grevesse 1989) are represented by the heavy line and circles.

However, near $A \approx 130$ and 196, better agreement with the observations was achieved in our calculations performed using the fission probabilities of Thielemann *et al.* (1983). This confirms the importance of reliable calculations of the beta-decay strength functions required to calculate $P_{\beta\mathrm{df}}$.

Excellent agreement of the computed $Y_Z$ with both the observed ss abundances and the elemental abundances in old stars (Sneden *et al.* 2000; Cowan *et al.* 1999) was achieved at $Y_e = 0.08$–$0.12$ not only for elements with $56 < Z < 76$ (Fig. 2) using various beta-delayed fission rates (Thielemann *et al.* 1983; Staudt and Klapdor-Kleingrothaus 1992). Note that there is much better agreement with the observations in the range $Z \approx 44$–$48$ for asymmetric fission that leads to shorter cycle times; this agreement is also observed for a wider range of initial neutrino excesses $Y_e$. This shows that the duration of the $r$-process in very old stars is fairly long, and fission plays an important role and may determine the observed abundances of at least some of the nuclides in the mass range $100 < A < 120$.

Note that we did not set the goal of finding better agreement with observations by a superposition of solutions. Our objective was to understand both the influence of the initial neutron excess, the fission-product mass distribution, and the beta-delayed fission data on nucleosynthesis and the role of various fission channels in the $r$-process.

Having considered previously (Panov *et al.* 2000) various models of the mass distribution and its influence on the abundances of the $r$-process elements in

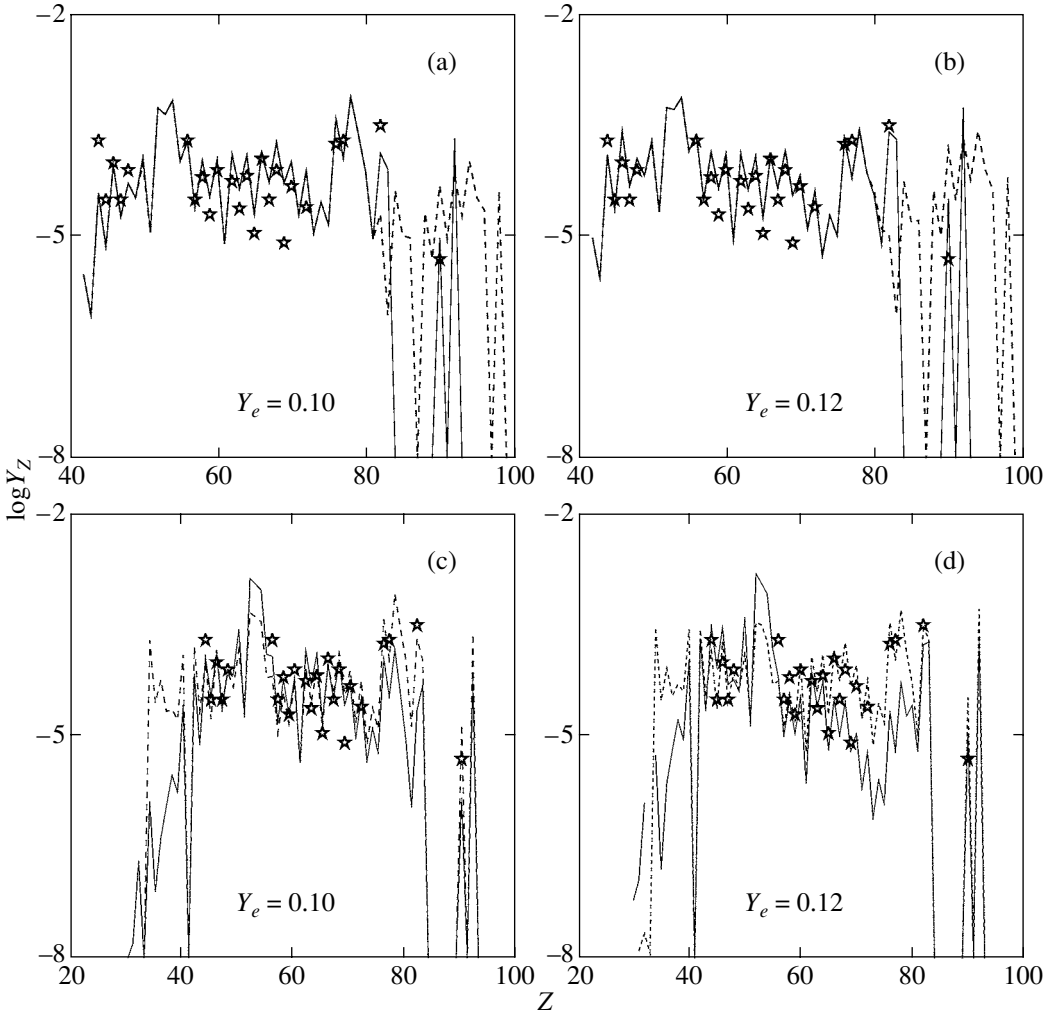


**Fig. 2.** Same as Fig. 1 for the isotope abundance $Y(Z)$. The observed abundances in old, metal-poor stars (Sneden *et al.* 2000) are represented by stars.

the specific neutron-star merger scenario, in which the $r$-process proceeds at high free-neutron densities (Freiburghaus *et al.* 1999a), we used mainly the systematics of Itkis *et al.* (1989) in our calculations, because the fission-product mass distribution for highly neutron-rich nuclei has not been studied adequately and requires a separate discussion.

Both abundance observations for elements with $Z \sim 30$ and more reliable fission-rate calculations are required to clarify further the question of the contribution from asymmetric fission, and to interpret the observations in the mass range $A \sim 100$–$120$.

### *The Role of Neutron-Induced Fission*

Let us consider the results of the total influence of neutron-induced fission on the yields of the $r$-process elements. In simulating the $r$-process, we used the neutron-induced fission rates for all isotopes from francium ($Z = 87$) to fermium ($Z = 100$) that we calculated using the SMOKER code (Thielemann *et al.* 1987) on the basis of the well-known fission barriers (Howard and Möller 1980).

Figure 3 shows the motion of the nucleosynthesis wave and the variation of the abundance $Y_A$ with time in the scenario under consideration at the initial neutron excess $Y_e = 0.1$. The calculations were performed using the time profiles of the temperature $T_9(t)$ and density $n_n(t)$ obtained by Rosswog *et al.* (1999) and the initial values of $T_9(0)$=6 and $n_n(0) = 10^{35}$ (the thin line in the region $100 < A < 120$ in Fig. 3a).

For an $r$-process duration of 0.5 s (Fig. 3a), virtually all of the nuclei with $A < 180$ were burned out, and the formation of secondary nuclei in the region $A \approx 130$ begins through fission. At $\tau_r = 0.7$ s (Fig. 3b), the previously burned isotopes with masses $A \approx 120$–$200$ are again produced through (primarily

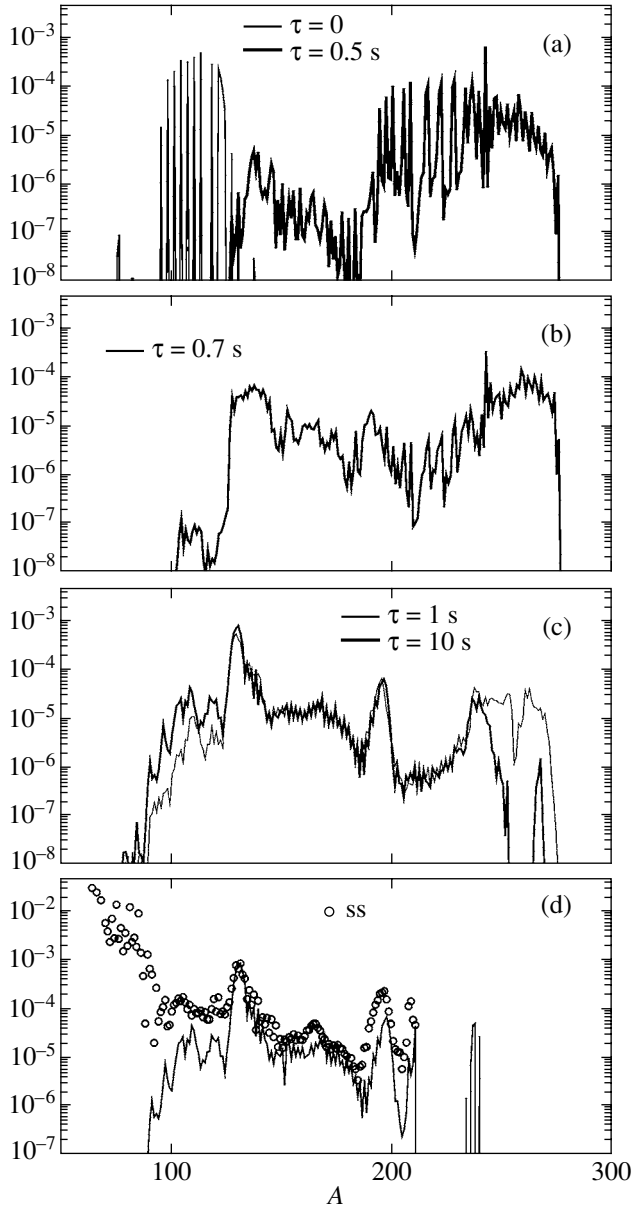


**Fig. 3.** Abundance variations during the $r$-process: the nucleosynthesis duration $\tau = 0.5$ (a), 0.7 (b), 1 s (thin line), 10 s (thick line) (c), and the final abundance (d). The initial (for the onset of the $r$-process) composition at $\tau = 0$ (a) is indicated by the thin line; the ss abundances are denoted by the circles.

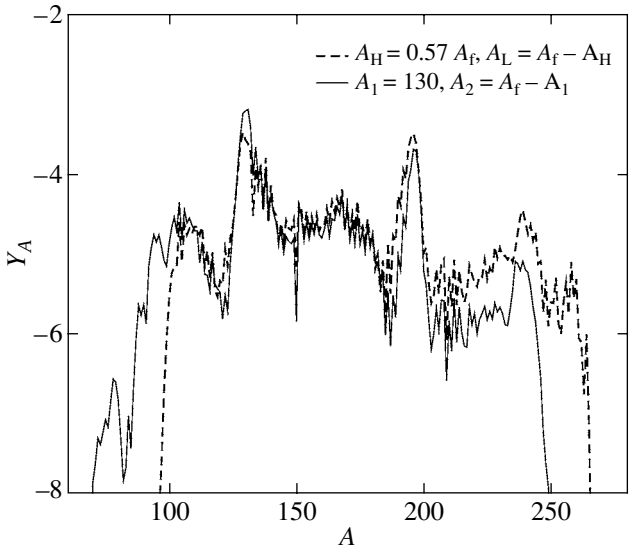


**Fig. 4.** Final elemental abundances (without alpha-decay) for various mass distributions of the fission-product nuclei and with (solid line) and without (dashed line) neutron-induced fission.

neutron-induced) fission and the $r$-process cycling. Since the free-neutron density drops to $10^{20}$ cm$^{-3}$, the neutron-induced fission almost ceases, the neutron capture terminates, and the motion of the nucleosynthesis wave stops. At $\tau_r = 10$ s (Fig. 3c), the formation of new nuclei through beta-decay and beta-induced fission is virtually complete. The computed abundances of the nuclei with masses $A \approx 100$–$120$ are in good agreement with the observations of old stars. At $\tau_r = 10^{10}$ s, the final abundance curve that includes not only beta-decay, but also alpha-decay is shown in Fig. 3d.

Our previous calculations (Panov and Thielemann 2003b) showed that when the free-neutron density is high enough, intermediate-mass nuclei are produced during the $r$-process through both symmetric and asymmetric fission. However, the nuclei with masses $A < 130$ are rapidly burned out. The lightest nuclei with $90 < A < 120$ are produced through beta-delayed asymmetric fission only when the neutron density drops below its critical value and the $r$-process terminates.

Figure 4 shows the final elemental abundances (without alpha decay) for various mass distributions of the fission-product nuclei with and without neutron-induced fission. Clearly, including the neutron-induced fission removes the overproduction of the third-peak elements (with respect to the abundance of the second-peak elements), and various fission-product mass asymmetries lead to great differences in the yields of nuclei with masses $80 \leq A \leq 120$.

Figure 5 shows the role of beta-delayed and neutron-induced fission at various nucleosynthesis stages (Fig. 5a) and the contribution of various fissionable chemical elements (Fig. 5b) to the formation of fission-product nuclei.

Clearly, neutron-induced fission in the scenario under consideration affects most strongly the formation of nuclei with $Z > 87$.

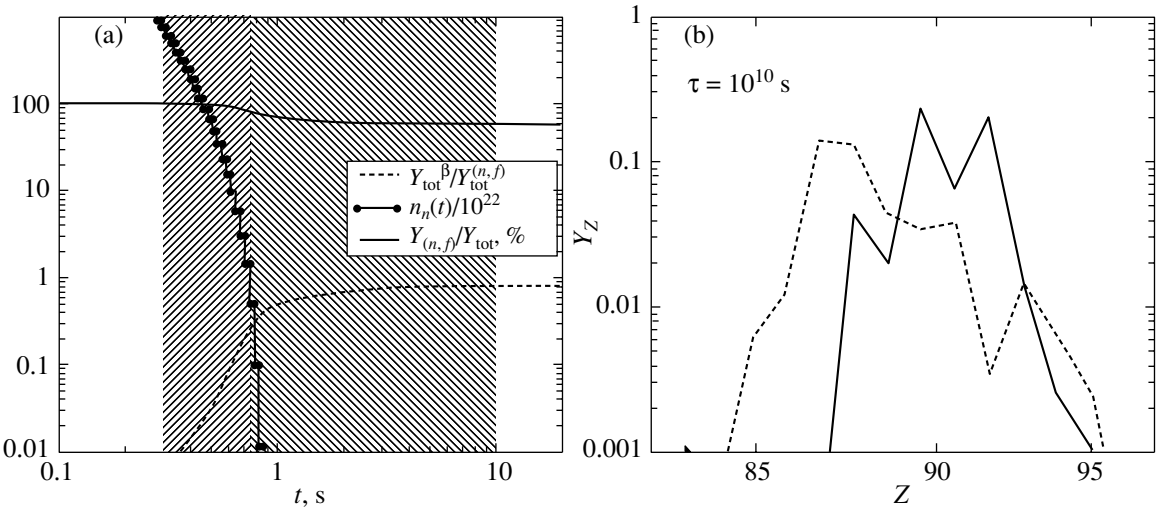


**Fig. 5.** (a) Dynamics of the change in the role of beta-delayed and neutron-induced fission: the fraction of the secondary nuclei (in percent) produced through neutron-induced fission (solid line); the ratio of the number of fissions during beta-decay to the number of fissions through neutron-induced fission (dashed line); the free-neutron density (the line with circles). The regions where neutron-induced (left hatching) and beta-delayed (right hatching) fission dominate are hatched. (b) The fraction of the chemical elements decayed during nucleosynthesis in the NSM scenario through neutron-induced (solid line) and beta-delayed (dashed line) fission.

Our calculations lead us to conclude that neutron-induced fission must play a crucial role in the $r$-process cycling when the neutron density is fairly high. The neutron-induced fission rates (with the barriers of Howard and Möller (1980)), particularly for the transuranium elements, are so high (Table 1) that, as preliminary estimates indicate, this fission channel remains important even for higher barriers (Mamdouh *et al.* 1998; Myers and Swiatecki 1999).

### *Nuclear Cosmochronology*

Having considered the various fission channels previously (Panov and Thielemann 2003a), we estimated the influence of both nuclear data and different fission channels on the nucleosynthesis results. Note that the choice of mass formulas, the fission-barrier determination, and the consistent fission-rate calculation are the subjects of a separate study that requires a proper calculation of the beta-decay strength functions (Möller *et al.* 2003). In this paper, we considered only the relative contribution of the beta-delayed and neutron-induced fission and showed the importance of the neutron-induced fission. In this section, we discuss the extent to which a consistent allowance for all fission channels, neutron-induced fission in particular, affects the determination of the age of the Galaxy.

The uranium ($A = 235, 238$) and thorium ($A = 232$) isotopes have been most commonly used as pairs of cosmochronometer nuclei to determine the age of the Galaxy by the isotopic-ratio method (Cowan *et al.* 1991), although there are also other isotopes that can be used for nuclear chronometry (see Table 1). We considered the stability of the abundance ratios for the pairs of $^{232}$Th and $^{235,238}$U chronometers as a test of the relative reliability of the fission models used in the $r$-process calculations. We emphasize once again that the abundances of most nuclei in the mass range $A \approx 130-230$ are weakly sensitive to the fission model; this has predetermined the use of the rough fission models described above for several years.

According to our previous calculations (Lyutostanskii *et al.* 1988), the permitted and most

**Table 1.** List of nuclei that are possible cosmochronometers

| Mother nucleus | $T_{1/2}$, yr | Daughter nucleus | Decay |
|---|---|---|---|
| $^{129}$I | $1.6 \times 10^7$ | $^{129}$Xe | $\beta^-$ |
| $^{182}$Hf | $9.0 \times 10^6$ | $^{182}$W | $\beta^-$ |
| $^{187}$Re | $4.5 \times 10^{10}$ | $^{187}$Os | $\beta^-$ |
| $^{232}$Th | $1.4 \times 10^{10}$ | $^{208}$Pb | $\alpha$ |
| $^{235}$U | $7.0 \times 10^8$ | $^{207}$Pb | $\alpha$ |
| $^{236}$U | $2.3 \times 10^7$ | $^{232}$Th | $\alpha$ |
| $^{238}$U | $4.5 \times 10^9$ | $^{206}$Pb | $\alpha$ |
| $^{244}$Pu | $8.2 \times 10^7$ | $^{232}$Th/$(A_1 + A_2)$ | $\alpha/sf$ |
| $^{247}$Cm | $1.6 \times 10^7$ | $^{235}$U | $\alpha$ |

**Table 2.** Abundances of the $^{232}$Th and $^{235,238}$U cosmochronometers in different models

| No. | Calculation | $Y_{U^{235}}$ | $Y_{U^{238}}$ | $Y_{U^{235}}/Y_{U^{238}}$ | $Y_{Th^{232}}$ | $Y_{Th^{232}}/Y_{U^{238}}$ |
|---|---|---|---|---|---|---|
| 1 | CNF, without fission | $1.43 \times 10^{-2}$ | $1.49 \times 10^{-3}$ | 1.0 | $2.5 \times 10^{-3}$ | 1.68 |
| 2 | CNF, $A_f = 240$ | $1.12 \times 10^{-10}$ | $4.16 \times 10^{-11}$ | 2.7 | $3.56 \times 10^{-10}$ | 8.6 |
| 3 | NSM, $A_f = 240$ | $1.39 \times 10^{-5}$ | $3.96 \times 10^{-6}$ | 3.5 | $2.31 \times 10^{-5}$ | 5.8 |
| 4 | NSM, $A_f \longrightarrow A_1 = A_2$ | $5.29 \times 10^{-5}$ | $5.71 \times 10^{-5}$ | 0.93 | $5.86 \times 10^{-5}$ | 1.03 |
| 5 | NSM, mass formula of Janacke and Eynon (1976) | $5.02 \times 10^{-5}$ | $5.29 \times 10^{-5}$ | 0.95 | $5.51 \times 10^{-5}$ | 1.04 |
| 6 | NSM, $A_f \longrightarrow A_1/A_2 = 0.75$ | $6.51 \times 10^{-5}$ | $6.20 \times 10^{-5}$ | 1.05 | $7.38 \times 10^{-5}$ | 1.19 |
| 7 | NSM, $A_f \longrightarrow A_L + A_H$ | $6.89 \times 10^{-5}$ | $6.97 \times 10^{-5}$ | 0.99 | $8.31 \times 10^{-5}$ | 1.19 |
| 8 | NSM, $A_L + A_H$, $P_{\beta df}$ (Staudt and Klapdor-Kleingrothaus 1992) | $3.61 \times 10^{-5}$ | $9.56 \times 10^{-6}$ | 3.74 | $1.42 \times 10^{-5}$ | 1.47 |

probable abundance ratios of the cosmochronometer nuclei lie within the range 1 to 2:

$$1 \leq Y_{232}/Y_{238} < 2; \quad 1 < Y_{235}/Y_{238} < 2, \qquad (2)$$

in agreement with the calculations of other authors (see the review by Cowan *et al.* 1991). We compared the calculations both for different scenarios and with different fission models and nuclear data (Table 2). The first two calculations were performed in the constant nuclear flux (CNF) model; the remaining calculations were performed for the neutron-star merger (NSM) scenario. As a result, we found that not all of the considered models yield a result consistent with condition (2). We considered the CNF and NSM models with different assumptions about the distribution of the fission-product nuclei, different mass formulas, different computational models for the beta-delayed fission probability, and different $r$-process boundary conditions. In particular, we considered the validity of the neutron-induced fission at $A_f = 240$ (Freiburghaus *et al.* 1999b). Clearly, in two cases (nos. 2 and 3 in Table 2), we have $Y_{232}/Y_{238}$ and $Y_{235}/Y_{238}$ ratios that drop out of the admissible range. Consequently, to determine the chronometric parameter, we cannot artificially restrict the nucleosynthesis region, nor can we terminate the $r$-process arbitrarily, at low $A_f \sim 240$. The calculations of the beta-delayed fission probability by Staudt and Klapdor-Kleingrothaus (1992) also yield an overestimated value for one of the ratios (no. 8 in Table 2). This provides further evidence that the fission rates must be recalculated more consistently on the basis of new calculations of the fission barriers $B_f$ and the beta-decayed force functions $S_\beta$.

We see from the results in Table 2 that, apart from the fission barriers, the restriction of the region of transuranium elements involved in nucleosynthesis and the technique for calculating the beta-delayed fission rates based on the strength-function model have the strongest effect on the result (in our case, the age of the Galaxy). Changing the mass distribution weakly affects the ratios of the cosmochronometer yields, i.e., it cannot lead to a significant increase in the error in the age of the Galaxy.

## CONCLUSIONS

Thus, we may conclude that neutron-induced fission for the NSM scenario under consideration in highly neutronized ejecta ($Y_e = 0.1$) plays a major role in $r$-process cycling until the neutron density falls to $10^{22}$ cm$^{-3}$, and this process is the main obstacle to the formation of superheavy elements. Nevertheless, most of the secondary nuclei are produced through beta-delayed fission at the end of the $r$-process, when the free-neutron density is already too low to maintain it and the only nuclear reactions are beta decay and beta-delayed fission. It is beta-delayed fission that is responsible for the ultimate formation of the isotope yields in the region before the second peak and for the abundances of elements heavier than lead (which ultimately lead to the formation of Pb, Bi, Th, U through alpha decays).

Without discussing here the dependence of the fission rates on the fission barriers, our parametric calculations have shown that, even if the fission rates used were overestimated, the pattern of termination of the $r$-process will not change greatly. If the actual fission barriers prove to be higher than the fission barriers of Howard and Möller (1980) used here, then the region of active fission will shift to the region of chemical elements with larger $Z$.

In conclusion, note that, in addition to the adequately studied neutron-induced and beta-delayed

fission processes, a new fission channel—neutrino-induced fission—has recently been introduced by Qian (2002) in the $r$-process scenario. Therefore, it should be noted that it becomes even more important to calculate the rates of weak processes (Langanke and Kolbe 2002; Langanke and Martinec-Pinedo 2003).

There is no doubt that fission plays an important role in the $r$-process and that more accurate data on both the fission rates and the mass distribution of the fission-product nuclei are required; these data should be used to further develop the theory of rapid nucleosynthesis.

## ACKNOWLEDGMENTS

We wish to thank E. Kolbe, K.-L. Kratz, K. Langanke, G. Martinec-Pinedo, D.K. Nadyozhin, B. Pfeiffer, T. Rauscher, and S. Rosswog their for helpful discussions and interest in this study. This work was supported in part by the Swiss National Foundation (SNF no. 20-68031.02) and the Russian Foundation for Basic Research (project no. 04-02-16793-a ).

## REFERENCES

1. E. Anders and N. Grevesse, Cosmochimica Acta **53**, 197 (1989).
2. S. I. Blinnikov and I. V. Panov, Pis'ma Astron. Zh. **22**, 39 (1996) [Astron. Lett. **22**, 39 (1996)].
3. A. G. W. Cameron, Astrophys. J. **562**, 456 (2001).
4. J. J. Cowan, B. Pfeiffer, K.-L. Kratz, *et al.*, Astrophys. J. **521**, 194 (1999).
5. J. J. Cowan, F.-K. Thielemann, and J. W. Truran, Annu. Rev. Astron. Astrophys. **29**, 447 (1991).
6. C. Freiburghaus, J.-F. Rembges, T. Rauscher, *et al.*, Astrophys. J. **516**, 381 (1999a).
7. C. Freiburghaus, S. Rosswog, and F.-K. Thielemann, Astrophys. J. Lett. **525**, L121 (1999b).
8. S. Goriely and B. Clerbaux, Astron. Astrophys. **346**, 798 (1999).
9. E. R. Hilf, H. V. Groote, and K. Takahashi, in *Proceedings of the 3rd International Conference on Nuclei far from Stability* (CERN-76-13, 1976), p. 142.
10. W. M. Howard and P. Möller, At. Data Nucl. Data Tables **25**, 219 (1980).
11. M. G. Itkis, V. N. Okolovich, and G. N. Smirenkin, Nucl. Phys. A **502**, 243 (1989).
12. J. Janacke and B. P. Eynon, At. Data Nucl. Data Tables **17**, 467 (1976).
13. K.-L. Kratz, J.-P. Bitouzet, F.-K. Thielemann, *et al.*, Astrophys. J. **403**, 216 (1993).
14. K. Langanke and E. Kolbe, At. Data Nucl. Data Tables **82**, 191 (2002).
15. K. Langanke and G. Martinec-Pinedo, Rev. Mod. Phys. **75**, 819 (2003).
16. Yu. S. Lyutostanskiĭ, S. V. Malevannyĭ, I. V. Panov, and V. M. Chechetkin, Yad. Fiz. **47**, 780 (1988) [Sov. J. Nucl. Phys. **47**, 780 (1988)].
17. A. Mamdouh, J. M. Pearson, M. Rayet, and F. Tondeur, Nucl. Phys. A **644**, 389 (1998).
18. P. Möller, B. Pfeiffer, and K.-L. Kratz, Phys. Rev. C **67**, 055802 (2003).
19. W. D. Myers and W. J. Swiatecki, Phys. Rev. C **60**, 014606 (1999).
20. D. K. Nadyozhin, I. V. Panov, and S. I. Blinnikov, Astron. Astrophys. **335**, 207 (1998).
21. I. V. Panov, S. I. Blinnikov, and F.-K. Thielemann, Pis'ma Astron. Zh. **27**, 248 (2001a) [Astron. Lett. **27**, 239 (2001)].
22. I. V. Panov and V. M. Chechetkin, Pis'ma Astron. Zh. **28**, 476 (2002) [Astron. Lett. **28**, 476 (2002)].
23. I. V. Panov, C. Freiburghaus, and F.-K. Thielemann, Nucl. Phys. A **688**, 587 (2001b).
24. I. V. Panov, C. Freiburghaus, and F.-K. Thielemann, in *Proceedings of Workshop on Nuclear Astrophysics,* Ed. by W. Hillebrandt and E. Müller (Ringberg, Garching, MPA, 2000), p. 73.
25. I. V. Panov and D. K. Nadyozhin, Pis'ma Astron. Zh. **25**, 369 (1999) [Astron. Lett. **25**, 369 (1999)].
26. I. V. Panov and F.-K. Thielemann, Pis'ma Astron. Zh. **29**, 508 (2003a) [Astron. Lett. **29**, 510 (2003)].
27. I. V. Panov and F.-K. Thielemann, Nucl. Phys. A **718**, 647 (2003b).
28. Y.-Z. Qian, Astrophys. J. Lett. **569**, L103 (2002).
29. T. Rauscher and F.-K. Thielemann, At. Data Nucl. Data Tables **75**, 1 (2000).
30. S. Rosswog, M. Liebendörfer, F.-K. Thielemann, *et al.*, Astron. Astrophys. **341**, 499 (1999).
31. P. A. Seeger, W. A. Fowler, and D. D. Clayton, Astrophys. J., Suppl. Ser. **97**, 121 (1965).
32. C. Sneden, J. J. Cowan, I. I. Ivans, *et al.*, Astrophys. J. **533**, L139 (2000).
33. A. Staudt and H. V. Klapdor-Kleingrothaus, Nucl. Phys. A **549**, 254 (1992).
34. F.-K. Thielemann, M. Arnould, and W. Truran, *Advan. Nucl. Astrophys.,* Ed. by E. Vangioni-Flam *et al.* (Frontiers, Gif sur Yvette, 1987), p. 525.
35. F.-K. Thielemann, A. G. W. Cameron, and J. J. Cowan, in *Proceedings of International Conference: 50 Years with Nuclear Fission,* Ed. by J. Behrens and A. D. Carlson (Am. Nucl. Soc., La Grange Park, 1989), p. 592.
36. F.-K. Thielemann, J. Metzinger, and H. V. Klapdor-Kleingrothaus, Z. Phys. A **309**, 301 (1983).

*Translated by V. Astakhov*